High entropy spinel oxides and iron-cobalt based electrocatalysts for rechargeable zinc-air batteries.

UNIVERSITY OF THE
WITWATERSRAND,
JOHANNESBURG

Agnes M. Mongwe (1847873)

A dissertation submitted to the faculty of Science, University of the Witwatersrand, Johannesburg in fulfilment of the requirements for the Master of Science degree.

Master of Science

Supervisors: Prof. Kenneth I. Ozoemena, Dr. Aderemi B. Haruna

August 2024

DECLARATION

I declare that this dissertation is my own, unaided work. It is being submitted for the Master of Science degree at the University of the Witwatersrand, Johannesburg. It has not been submitted before for any degree or examination at any other University.

Signature:  Date: 10 August 2024

DEDICATION

This dissertation is dedicated to my family, to those who served as a source of inspiration throughout this research and to friends who became part of my family. Your constant prayers and encouragement kept me uplifted and I hope this achievement will fulfil the dream you envisioned for me.

I will forever be grateful for your presence in my life.

ACKNOWLEDGEMENTS

The successful completion of this project is owed to the efforts of many people.

To my heavenly Father God, thank you for keeping me strong and blessed. You have done so much for me, and your strength kept me going in moments of doubt. I have learnt throughout this journey that there's power beyond me which is in control.

To my supervisor Prof. Kenneth Ozoemena for granting me an opportunity to work on this project. Thank you for unleashing the potential I never thought I had and for your constant support throughout this project. I am grateful for the bi-weekly one-on-one meetings which helped me better understand my data and see room for improvement.

To my Co-supervisor Dr. Aderemi Haruna for overseeing every step of the project. You have always been there to offer your knowledge and valuable insights even during challenging times. Thank you for taking the time to help with the synthesis of the catalysts.

To Dr. Thapelo Mofokeng for lending a helping hand whenever possible. Thank you for assisting with drawing the synthesis schemes and deconvoluting the XPS.

Thank you to all members of the materials electrochemistry and energy technologies (MEET) group for showing me how to pull the strings in the lab. Your constructive criticism helped me grow.

Many thanks, to Dr Augustus Lebechi for teaching me how to run the electrochemistry and process the data.

To Lesego Gaolatlhe for her patience while teaching me how to assemble and run zinc-air batteries. Her efforts in the rechargeable zinc-air battery breakthrough do not go unnoticed. Thank you for taking the time to overcome the challenges and passing down your knowledge.

Profound gratitude to the Sasol-NRF for the financial support throughout this research project.

Many thanks to my family and friends for their constant support throughout this journey. They are my greatest cheerleaders and their presence in my life will forever be cherished.

RESEARCH OUTPUT

Manuscripts prepared for publication.

1. **Agnes M. Mongwe**, Aderemi B. Haruna, Lesego Gaolatlhe, Thapelo P. Mofokeng, Augustus K. Lebechi, Patrick V. Mwonga and Kenneth I. Ozoemena. *Onion-like carbon supported high-entropy spinel oxides [$(CoCuFeMnNi)_3O_4$] for robust rechargeable zinc-air batteries*. (in preparation)
2. **Agnes M. Mongwe**, Augustus K. Lebechi, Aderemi B. Haruna, Thapelo P. Mofokeng and Kenneth I. Ozoemena. *Hybrid FeCo-Fe_2CoO_4/C bifunctional electrocatalysts for high-performance rechargeable zinc-air batteries.* (in preparation)

CONFERENCES

1. **Agnes M. Mongwe**, Augustus K. Lebechi, Aderemi B. Haruna and Kenneth I. Ozoemena. *Microwave irradiated Fe_2CoO_4-FeCo/C electrocatalysts for ORR, OER and Rechargeable Zinc-Air Batteries*. 32nd Annual Meeting of the Catalysis Society of South Africa (CATSA), 13th to 16th November 2022 at the Champagne Sports Resort, Central Drakensberg, KwaZulu-Natal, South Africa. **(Poster presentation)**.
2. **Agnes M. Mongwe**, Aderemi B. Haruna and Kenneth I. Ozoemena. *High entropy spinel oxides as bifunctional electrocatalysts for high-performance rechargeable zinc-air batteries*. 6th International Symposium on Electrochemistry, Electrochem SA, 3rd to 6th April 2023, University of Johannesburg, South Africa. **(Oral presentation)**.
3. **Agnes M. Mongwe**, Augustus K. Lebechi, Aderemi B. Haruna and Kenneth I. Ozoemena. *Defect-engineered FeCo-Fe_2CoO_4/C bifunctional electrocatalysts for rechargeable zinc-air batteries.* 33rd Annual meeting of the Catalysis Society of South Africa (CATSA), 5th to 8th November 2023 at the Diaz Hotel & Resort in Mossel bay in the Western cape, South Africa. **(Flash talk + Poster presentation)**.

PROFESSIONAL ORGANISATIONS

1. Member of the South African Chemical Institute.

ABSTRACT

The development of effective and stable rechargeable zinc-air batteries (RZABs) using noble-metal free bifunctional electrocatalysts for oxygen evolution reaction (OER) and oxygen reduction reaction (ORR) has been a key challenge to its practical applications. This MSc research work strategically investigated some synthetic methods aimed at tuning the physicochemistry and electrochemical properties of two electrocatalysts (i.e., noble-metal free high entropy spinel oxide ($HESO_x$) ($(CoCuFeMnNi)_3O_4$) and spinel Fe_2CoO_4 for rechargeable zinc-air batteries). For $HESO_x$, a simple and reproducible Pechini method was used to synthesize a homogeneous nanosized electrocatalyst $HESO_x$-550. The $HESO_x$-550 was thereafter supported on onion-like carbon (OLC) in (1) an acidic environment to produce $HESO_x$-550/OLC_{AT} (where AT stands for acid-treated) and (2) a nonacidic environment to produce $HESO_x$-550/OLC. The effects of the different synthesis environments on these three samples were thoroughly investigated using different analytical techniques, including X-ray diffraction (XRD), X-ray photoelectron spectroscopy (XPS), Raman spectroscopy, thermogravimetric analysis (TGA) and Nitrogen Gas Adsorption analysis. The Nitrogen Gas Adsorption analysis results show that the $HESO_x$-550/OLC_{AT} has the largest surface area and pore volume. The electron paramagnetic resonance (EPR) and O1s XPS data consistently proved that $HESO_x$-550/OLC_{AT} has improved oxygen vacancies which are essential in improving conductivity and offering abundant reaction sites. The $HESO_x$-550/OLC_{AT} shows the best bifunctional ORR and OER electrocatalytic performance with a bifunctionality index (ΔE) of 0.70 V in 1 M KOH. In addition, the RZAB air electrode with $HESO_x$-550/OLC_{AT} exhibits high areal capacity (60 mAh cm^{-2}) and areal energy density (73.2 mWh cm^{-2}) with a long-term cycle stability over 112 h in 6.0 M KOH and 0.2 M zinc acetate. The $HESO_x$-550/OLC_{AT} RZAB shows better electrochemical performance than 10wt.% Pt/C-

IrO_2 when cycled over 315 h under 27% depth of discharge condition. For Fe_2CoO_4, iron cobalt-based electrocatalysts on Vulcan carbon support were synthesized using a simple reduction method to produce two composites ($FeCo\text{-}Fe_2CoO_4/C_{Annealed}$), and ($FeCo\text{-}Fe_2CoO_4/C_{Microwave}$). The physicochemical analytical methods such as XRD, XPS, Raman, TGA and Nitrogen Gas Adsorption analysis were used to investigate the samples. The electrochemical analysis showed that the $FeCo\text{-}Fe_2CoO_4/C_{Ann}$ had a very low "bifunctionality index" (ΔE) of 0.76 V and the $FeCo\text{-}Fe_2CoO_4/C_{Ann}$ air cathode RZAB demonstrated good stability for over 50 h under harsh DOD conditions (35.2%). The assembled RZABs have areal energy densities of 48.4 $mWhcm^{-2}$ and 60.5 $mWhcm^{-2}$ which are higher than the minimum recommended areal energy density of 35 $mWhcm^{-2}$ (and better than most electrocatalysts reported in the literature). This study has significant contributions to the progress of practical applications of RZABs.

Table of Contents

List of figures

List of tables

List of schemes

List of symbols

Ar	Argon
C	Carbon
Co	Cobalt
Cu	Copper
℃	Degree Celsius
E	Potential
$E_{1/2}$	Half-wave potential
$E_{j=10}$	Potential at 10 mA cm^{-2} current density
ΔE	Change in potential
F	Faraday constant
Fe	Iron
H	Hour
IrO_2	Iridium oxide
K	Kelvin
min	minute(s)
Mn	Manganese
N	Nitrogen
n	Number of electrons
η	Overpotential

Ni	Nickel
O	Oxygen
O_l	Lattice oxygen
O_v	Oxygen vacancies
O_c	Chemosorbed oxygen
Pt	Platinum
R	Universal gas constant
ω	Rotation speed
Zn	Zinc

List of abbreviations

A

Ann	Annealed

B

BE	Binding energy
BET	Brunauer-Emmet-Teller

C

CE	Counter electrode
cm	Centimetre(s)
CP	Chronopotentiometry
CV	Cyclic voltammetry
CVs	Cyclic voltammograms

D

d	Interplanar spacing
DTG	Derivative Thermogravimetry
DFT	Density functional theory
DOD	Depth of discharge

E

ECSA	Electrochemical active surface area
EDS	Energy dispersive X-ray spectroscopy
EG	Ethylene glycol

EIS	Electrochemical impedance spectroscopy
EPR	Electron paramagnetic resonance
eV	Electron volt(s)
F	
FWHM	Full width at half maximum
G	
G	Grams
GCE	glassy carbon electrode
H	
HCl	Hydrochloric acid
HEO	High-entropy oxide
HER	Hydrogen evolution reaction
HESO	High-entropy spinel oxide
HEA	High-entropy alloy
I	
i	Current
J	
j	Current density
j_k	Kinetic current density
j_d	Diffusion limiting current density
K	

KCl	Potassium chloride
KE	Kinetic energy
K-L	Koutecky-Levich
KOH	Potassium hydroxide
L	
LSV	Linear sweep voltammetry
M	
MW	Microwave
O	
OCV	Open circuit voltage
OLC	Onion-like carbon
OER	Oxygen Evolution Reaction
ORR	Oxygen Reduction Reaction
P	
PTFE	Polytetrafluoroethylene
PVP	Polyvinylpyrolidone
R	
RDE	Rotating disc electrode
RE	Reference electrode
RHE	Reversible hydrogen electrode
RRDE	Rotating ring disc electrode

rpm	Revolutions per minute
RZAB	Rechargeable zinc-air battery
S	
SEM	Scanning electron microscopy
SHE	Standard hydrogen electrode
T	
TEM	Transmission electron microscopy
TGA	Thermogravimetric analysis
T_{max}	Temperature of maximum mass change rate
U	
UPS	Ultraviolet photoelectron spectroscopy
V	
V	Volts
W	
W	Watt
WE	Working electrode
Wt.%	Weight percentage
X	
XPS	X-ray photoelectron spectroscopy
XRD	X-ray diffraction
Z	

ZAB	Zinc-air battery

CHAPTER 1

Introduction

An overview of the background and motivation for the study is presented in this chapter. Furthermore, the chapter contains the study's objectives and aim, as well as an outline of the dissertation.

1.1. Background and Motivation

The ongoing energy crisis fuelled the need to reconsider the currently existing energy sources. Recent reports suggest that non-renewable energy sources such as coal and oil are quickly running out and will not sustain the ever-growing world population for the next century. The current world population in 2024 is sitting at over 8 billion people and this number is steadily rising escalating the dependence on fossil fuels for energy generation and transportation. The utilization of traditional fossil fuel-derived energy is not without many drawbacks, some of which require urgent intervention. It is not only known to result in the depletion of natural resources but the emission of carbon dioxide which leads to increasing average global temperatures. Increased greenhouse gas concentration in the atmosphere, if not reversed, will result in major changes to the world’s climate with negative consequences for our economy and society [1]

Figure 1.1 illustrates the global energy production from different types of fossil fuels and their corresponding carbon dioxide emissions which have increased exponentially over the years.

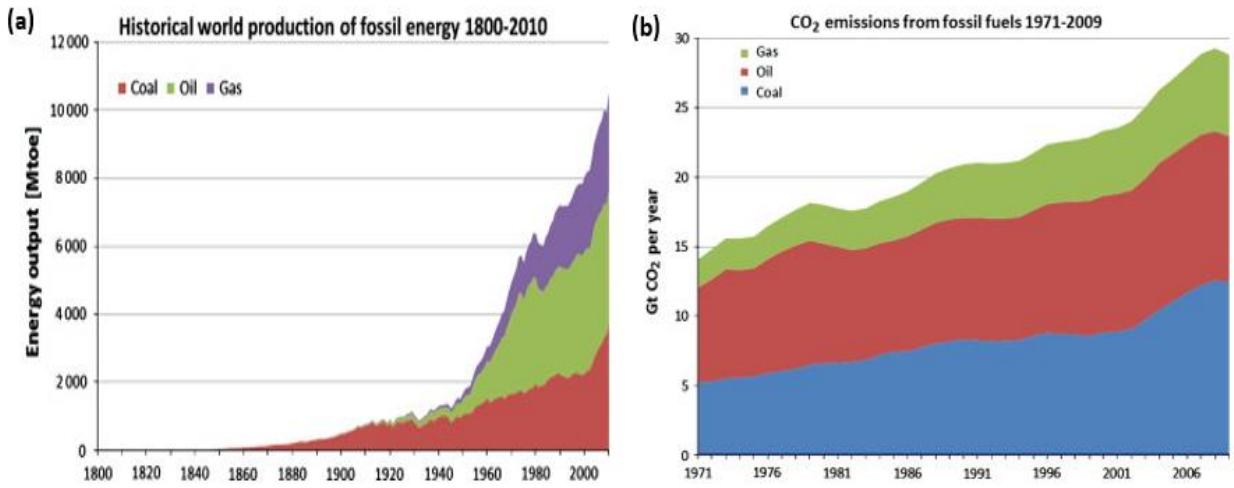

Figure 1. 1: (a) The global energy production from 1800 to 2010 [2] and (b) carbon dioxide emission trends from 1971 to 2009 due to various fossil fuels [3].

Approximately 80% of the world's energy is generated by fossil fuels and increasing evidence indicates that providing enough fossil energy for continued economic growth will be challenging, leading to energy insecurity [3]. Oil accounts for 32.8%, coal for 27.2%, and gas for 20.9% of energy generation [3]. The aforementioned data is worrisome since fossil fuel CO_2 emission is the biggest contributor to global warming. About 70% of all anthropogenic greenhouse gas emissions are derived from the energy sector due to fossil fuel combustion [3]. Greenhouse gas concentration levels have increased steadily and are now higher than ever in the past eight hundred thousand years [1]. This is the kind of intractable problem that renewable energy sources seek to improve by promoting green energy production.

The world's fossil fuel and mineral resources are finite and non-renewable [4]. In this regard, the world is turning towards clean and sustainable sources of energy. Renewable sources of energy include wind, solar, biomass, marine and hydropower energies [5]. By substituting conventional energy sources with renewable energy sources, we can mitigate greenhouse gas emissions and reduce global warming [5]. However renewable energy sources are only used as

alternatives and supply only 14% of the total energy demand [5]. **Figure 1.2** shows the energy contributions from different sources.

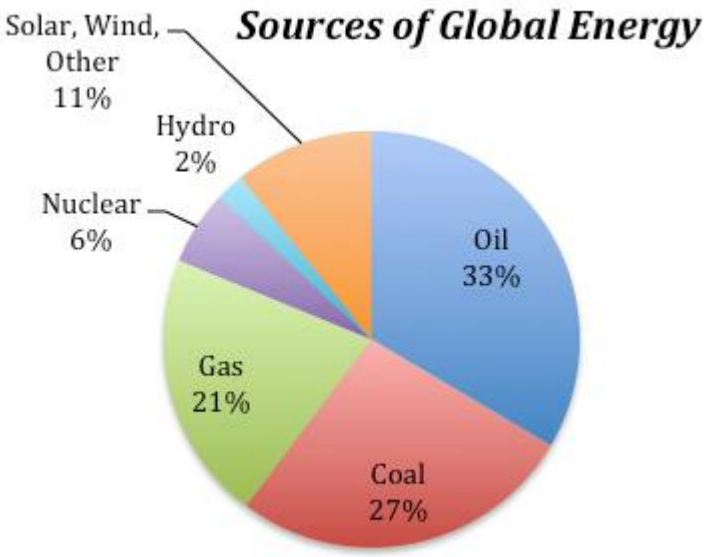

Figure 1. 2: The current contributions to our global energy from different sources. Data from International Energy Agency (iea.org).

It is evident that the usage of renewable energy sources does not surpass that of fossil fuels and one plausible reason can be their intermittent nature due to regional, seasonal and actual weather patterns variations. Due to the inherent variability and intermittency of many well-known renewable sources, this can result in erratic generation patterns and changes in power availability [6]. Energy storage devices can manage the risk of using renewable energy sources by acting as operating reserves that can immediately address short-term imbalances [6]. There is a need for the establishment of efficient electrochemical energy storage devices with a long life span, high power, and high energy to fill the gap that exists in the current energy market [7]. In this study, the electrochemical energy storage device of choice proposed to tackle the above-mentioned challenges is the rechargeable zinc-air battery. This device is known to hold more energy while being safe and cost-effective than other devices on the market.

1.2. Aim and objectives

1.2.1. Aim

This research aimed to design, synthesize and characterize high entropy ($(CoCuFeMnNi)_3O_4$/C) and iron-cobalt based (FeCo-Fe_2CoO_4/C) electrocatalysts for application in robust rechargeable zinc-air batteries.

1.2.2. Objectives

- To synthesize pristine $CoCuFeMnNi)_3O_4$ electrocatalysts using the Pechini method.
- To load onion-like carbon (OLC) on the $(CoCuFeMnNi)_3O_4$ and form the high entropy composite ($HESO_x$-550/OLC).
- To acid-treat the high entropy composite with HCl and form an acid-treated composite ($HESO_x$-550/OLC_{AT}).
- To synthesize FeCo-Fe_2CoO_4/C electrocatalysts using a simple reduction method.
- To characterize the electrocatalysts by studying their structure, morphology, and composition.
- To investigate the electrochemical performances of the electrocatalysts by testing for the bifunctionality (ORR and OER) in a three-electrode system.
- To test the performances of the electrocatalysts in rechargeable zinc-air batteries using a full-cell system.

1.3. Dissertation outline

Chapter 1 (Introduction): This is an introductory chapter that provides a general overview of the study, outlining the background**,** motivation, aims and objectives and the outline of the dissertation.

Chapter 2 (Literature review): This chapter reviews the background, working principles, challenges, progress, and materials for rechargeable zinc-air batteries.

Chapter 3 (Methodology): This chapter includes a brief overview of some of the characterization techniques, the electrochemical measurement techniques and the RZAB fabricating procedures used in this study.

Chapter 4: This chapter presents the experimental procedures, the results, and discussions for $HESO_x$ electrocatalysts and their application in RZAB.

Chapter 5: This chapter outlines the experimental procedures, the results, and discussions for iron-cobalt-based electrocatalysts and their application in RZAB.

Chapter 7 (Conclusions and recommendations): This chapter provides conclusions and recommendations for future work.

1.4. References

(1) Coyle E.D, Simmons R.A, *Understanding the Global Energy Crisis*, **2014 1** 1-5.

(2) Höök, M.; Li, J.; Johansson, K.; Snowden, S. Growth Rates of Global Energy Systems and Future Outlooks. *Natural Resources Research* **2012**, *21* (1), 23–41. https://doi.org/10.1007/s11053-011-9162-0.

(3) Höök, M.; Tang, X. Depletion of Fossil Fuels and Anthropogenic Climate Change-A Review. *Energy Policy* **2013**, *52*, 797–809. https://doi.org/10.1016/j.enpol.2012.10.046.

(4) Capellán-Pérez, I.; Mediavilla, M.; de Castro, C.; Carpintero, Ó.; Miguel, L. J. Fossil Fuel Depletion and Socio-Economic Scenarios: An Integrated Approach. *Energy* **2014**, *77*, 641–666. https://doi.org/10.1016/j.energy.2014.09.063.

(5) Panwar, N. L.; Kaushik, S. C.; Kothari, S. Role of Renewable Energy Sources in Environmental Protection: A Review. *Renewable and Sustainable Energy Reviews* **2011**, *15* (3), 1513–1524. https://doi.org/10.1016/j.rser.2010.11.037.

(6) Castillo, A.; Gayme, D. F. Grid-Scale Energy Storage Applications in Renewable Energy Integration: A Survey. *Energy Convers Manag* **2014**, *87*, 885–894. https://doi.org/10.1016/j.enconman.2014.07.063.

(7) Mai, L.; Tian, X.; Xu, X.; Chang, L.; Xu, L. Nanowire Electrodes for Electrochemical Energy Storage Devices. *Chem Rev* **2014**, *114* (23), 11828–11862. https://doi.org/10.1021/cr500177a.

CHAPTER 2

Literature review

2.1. Energy storage systems

The negative environmental impact, fluctuating prices, and rapid depletion of fossil fuels lead to the new green energy era. Renewable energy sources prices have significantly declined in the past decade and their little to no environmental impact makes them appealing [1]. Energy storage systems are vital in maintaining the energy produced from seasonal renewable energy sources like solar and wind. They act as a safeguard against power outages and release energy whenever the need arises. The energy storage systems can be classified as electrochemical (e.g. batteries, fuel cells and supercapacitors), electrical (pumped hydro electricity storage), mechanical (e.g. flywheels), thermal e.g. (oil or water heaters) and magnetic (e.g. superconducting magnetic energy storage) [2,3].

Electrochemical energy storage systems, especially batteries, are predominantly used worldwide because of their appealing high energy efficiency and availability in different sizes [4]. Batteries have higher energy density compared to supercapacitors and higher power compared to fuel cells as illustrated by the Ragone plot in **Figure 2.1.** Lead-acid, Nickel-Cadmium (Ni-Cd), Sodium sulphur (NaS) and lithium-ion batteries are amongst the well-known types of batteries [4]. However, metal-air batteries are also gaining attention in the electrochemistry field. Metal-air batteries are safer, cheaper (anode constructed from low-cost materials), lighter in weight (oxygen is utilized from the atmosphere and not stored inside the battery) and higher in energy density compared to other types [5]. The common metal electrodes for metal-air batteries include zinc [6], lithium [7], magnesium [8], aluminium [9], and others. Although some challenges still exist, zinc-air batteries are the only metal-air

batteries which are fully developed and have successfully been marketed as primary cells for many decades.

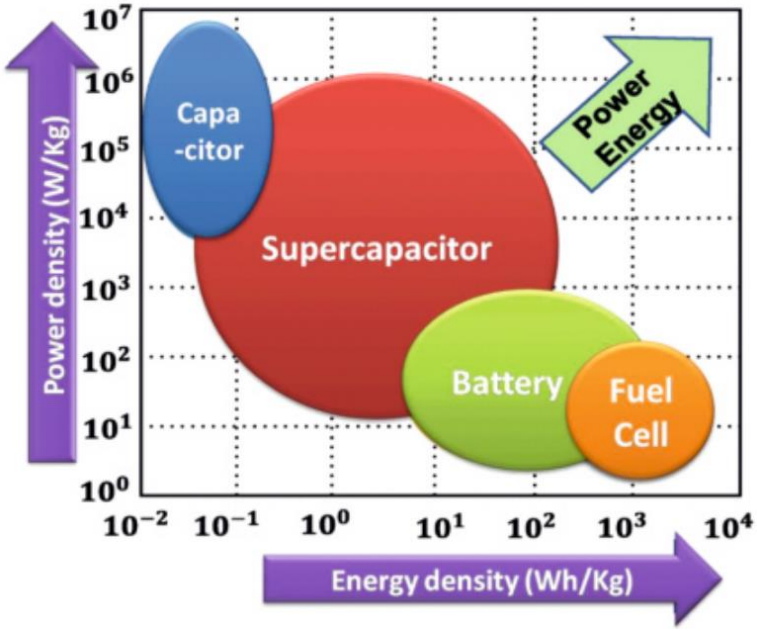

Figure 2. 1: Ragone plot: Power vs energy density (Adapted from [10]).

It is a necessity for energy storage devices to possess high energy meaning they can operate for a prolonged period. **Figure 2.2.** compares Zinc-based batteries and their closest competitors. Zinc-air batteries are taking the lead in terms of specific energy making them the perfect candidate for energy storage. Zinc is a geographically dispersed metal therefore it has low cost, it is non-toxic and it is compatible with water-based electrolytes removing risks of fire and explosion compared to their closest competitor (lithium-ion batteries).

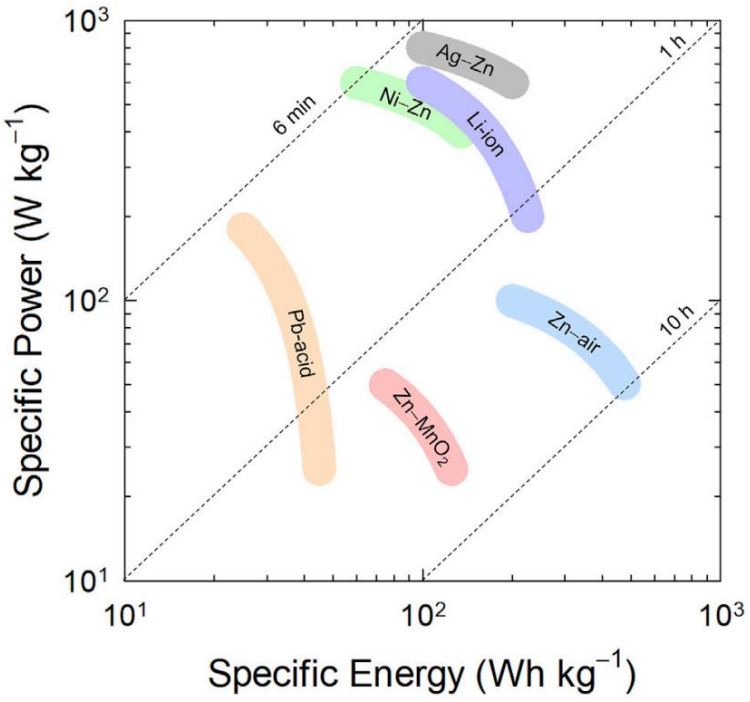

Figure 2. 2: An illustration of the Ragone plot, comparing zinc-based batteries to their closest competitors [11].

2.2. Zinc-air batteries.

2.2.1. History

Zinc-based batteries, discovered in the early 1800s went through a prolonged gestation period. The initial zinc-based electrochemical battery dates to the early 19th century. It is known as voltaic piles in which metallic zinc was employed as the energy storage anode material [12]. These voltaic piles design fuelled the evolution of zinc-based devices such as the Daniell cell (Zn|Cu, 1836) [13], Grove cell (Zn|HNO3, 1843) [14], and Leclanché cell (Zn|MnO2, 1866) [15].

Inspired by the Leclanché cell, a French engineer, L. Maiché uncovered a battery with a porous air cathode and zinc anode during the electrochemical systems discovery period [12]. Despite the similar design to the Leclanché cell, the porous platinized carbon air electrode proved to be as effective as MnO_2 cathodes in the zinc-air cell [6,12]. Despite Maiché's zinc-air battery's success, it failed to attract much recognition at that time despite its potential as an energy

storage device. The possibility of this battery gaining more traction was ruled out by low output voltage, electrolyte flooding and the acid electrolyte inherited from the Leclanché cell which led to unsatisfactory electrode material stability.

In 1932, Erwin A. Schumacher and George W. Heise turned the situation around by developing the earliest alkaline zinc-air battery which unlike Maiché's acidic electrolyte conditions utilized the electrolyte made from caustic soda to avoid electrode erosion and enhance performance [12]. The battery comprised of zinc anode, caustic soda electrolyte and carbon rod cathode (for the adsorption of oxygen) as active components. To prevent atmospheric carbon dioxide from neutralizing the interior environment's basicity and deteriorating the pristine electrolyte, lime was introduced. Primary alkaline zinc-air batteries were applied to a wide variety of applications, including railway signals, navigation instruments, oceanographic experiments, and marker lights by the end of the 1950s [12].

2.2.2. Rechargeable zinc-air batteries: general overview

Due to the ever-increasing energy demand, zinc-air batteries, developed since 1878 are now seeing a resurgence [12]. This century-old technology is characterized by high theoretical energy density (1086 W h kg^{-1}) with an ample supply of oxygen from the atmosphere, an abundance of raw materials, cost-effectiveness, environmental friendliness, and years of safety validation. In comparison to lithium-ion batteries, primary zinc-air batteries have 3x higher energy density thus they offer compelling "beyond lithium-ion" technologies [16].

The three main components in zinc-air batteries are the porous air cathode (to allow oxygen diffusion), the electrolyte (to facilitate ion transfer between the anode and cathode) and the zinc anode as depicted in **Figure 2.3.** The most popular electrolyte used in zinc-air batteries is a concentrated KOH solution mixed with zinc acetate to establish Zn electrochemical reaction reversibility at the anode [16,17]. The key anodic and cathodic reactions in rechargeable zinc-air batteries are summarized in **Figure 2.3** followed by a detailed description.

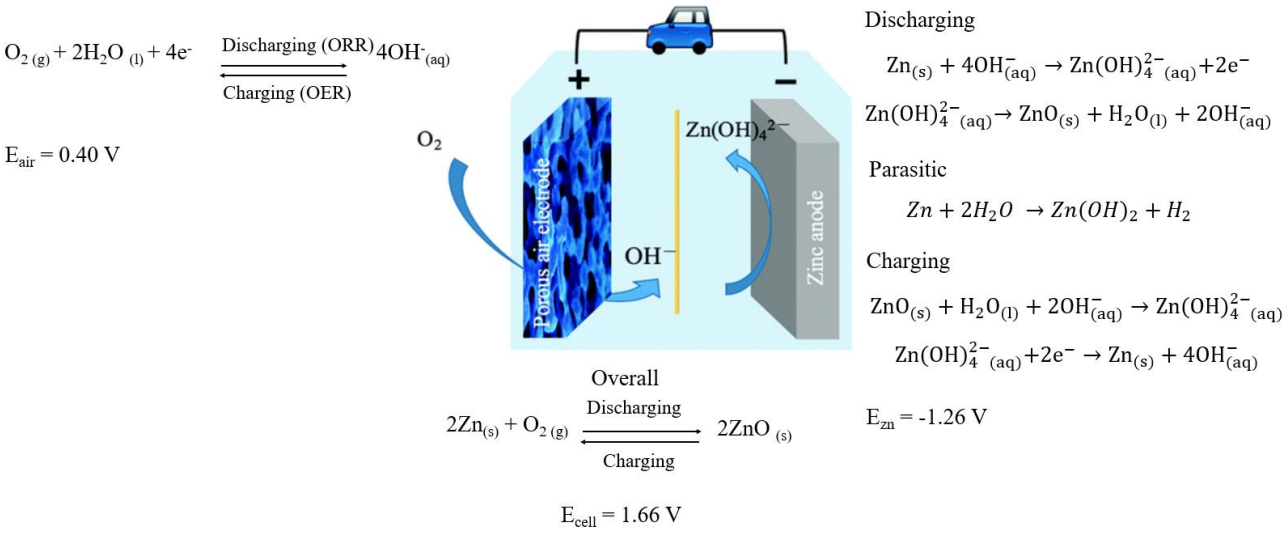

Figure 2. 3: Typical zinc-air battery schematic (Picture adapted from Ref. [18] and modified with equations).

(i) Zin Anode

During the battery discharge at the zinc electrode, the zinc plate gets oxidised and reacts with OH^- from the electrolyte forming the zincate ions ($Zn(OH)_4^{2-}$) which are soluble [18]. Due to supersaturation in the electrolyte, the zincate ions encounter spontaneous decomposition forming an insoluble zinc oxide (ZnO). This reaction pathway is reversible upon the charging of the battery with the $Zn(OH)_4^{2-}$ reversed back to metallic zinc (Zn). Another side reaction that is detrimental to the zinc anode is the hydrogen evolution reaction. This parasitic reaction is energetically favoured at the zinc anode which leads to the battery's self-discharge when it's at rest.

(ii) Air cathode

The vital air cathode electrochemical processes are oxygen reduction reaction (ORR) and oxygen evolution reaction (OER) in rechargeable zinc-air batteries [19]. Upon battery discharge, oxygen diffusion into the porous air electrode due to the concentration gradient. With the help of the catalyst, ORR occurs at the gas phase (O_2), solid air electrode

(electrocatalyst), and liquid (electrolyte) interface (triple phase boundary) [20]. Oxygen is reduced in the presence of an alkaline electrolyte to form hydroxide ions (OH-) which migrate in the electrolyte from the air cathode to the zinc anode to complete the discharge process. Oxygen is released back into the environment during the OER process (charging).

The O=O has an exceptionally strong energy bond of 498 kJ mol^{-1} which makes the reduction of the molecules by electrons very difficult. To lower the energy barrier, electrocatalysts are necessary to activate and cleave the O_2 bonds. In zinc-air batteries, an ideal electrocatalyst is required to be "bifunctional" meaning it favours both the forward (ORR) and the reverse reaction (OER).

ORR process in zinc-air batteries:

Oxygen diffuses through the porous air electrode and then gets absorbed on the catalysts' surface. Electrons then move from the zinc anode to the cathode weakening and breaking oxygen-oxygen bonds leading to the production of OH^- ions. This complex reaction is believed to proceed through two different mechanisms depending on the type of adsorption. The first mechanism involves a highly efficient 4-electron direct pathway, and the second one is the peroxide 2-electron pathway. In the 4-electron pathway, the two oxygen atoms are coordinated to the electrocatalyst and are directly reduced to OH^- under bidentate O_2 adsorption [18]. The 2-electron pathway is believed to proceed via the 2-electron reduction of peroxide or the chemical disproportionation of peroxide [18]. Due to the 2-electron pathways forming corrosive peroxide species and exhibiting low energy efficiency, the four-electron pathway is preferred. The pathways are given as follows:

Four-electron pathway:

$$O_2 + 2H_2O + 4e^- \rightarrow 4OH^-$$

Two-electron pathway:

$O_2 + H_2O + 2e^- \rightarrow HO_2^-$

$HO_2^- + H_2O + 2e^- \rightarrow 3HO^-$

$2HO_2^- \rightarrow 2HO^- + O_2$

Oxygen is a paramagnetic molecule meaning it has unpaired electrons and a small but positive magnetic susceptibility. Producing it from or reducing it to diamagnetic (electrons are paired) hydroxide/water requires spin-related electron transfer [21]. At room temperature, the electron transfer in water during oxygen electrocatalysis displays highly spin-related character because the ground state of the O_2 molecule is a triplet state (↑O=O↑) giving it its paramagnetic characteristics [21]. In reaction kinetics, triplet O_2 requires a vital spin-related electron transfer during oxygen reactions (either from O_2 to H_2O/OH^- (ORR) or H_2O/OH^- to O_2, OER) which is unintentionally neglected in most literature [21]. The transition from O_2 to OH^-/H_2O is spin forbidden which makes these reactions very complex to facilitate. **Figure 2.4** shows the molecular orbital diagrams for O_2, H_2O and OH^-.

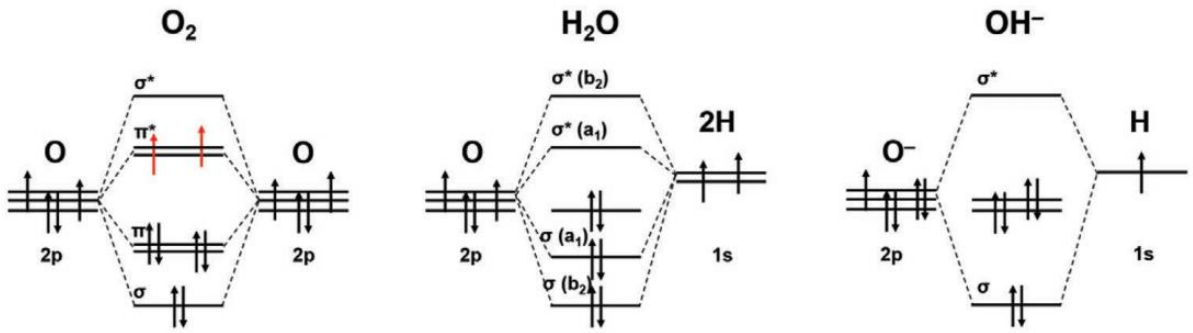

Figure 2. 4: Molecular orbital diagrams of O_2, H_2O and OH^- (adapted from [21]).

2.2.3. RZAB Challenges and Solutions

Although these batteries offer promising alternatives to lithium-ion batteries, their potential has not yet been fully realized due to the challenges with the air cathode, zinc anode and electrolyte.

2.2.3.1. Zinc electrode

(i) Hydrogen evolution reaction

The zinc interaction with the electrolyte results in a parasitic reaction causing spontaneous H_2 generation and corrosion of the electrode leading to a reduction in active material (Zn) efficiency [6]. HER is accompanied by the following equation:

$$Zn + 2H_2O \rightarrow H_{2(g)} + Zn(OH)_2 \qquad E^0 = -0.83\ V\ vs\ SHE\ (at\ pH\ 14)$$

The Zn^{2+}/Zn standard reduction potential is -1.26 V which is lower than that of HER (-0.83 V), therefore HER is more thermodynamically favoured than Zn^{2+}/Zn reaction [22]. As a result, the zinc anode self-discharges (corrodes) at rest making it difficult to charge the zinc-air battery with 100% coulombic efficiency [22]. This side reaction leads to the consumption of the electrolyte and reduces the zinc electrode utilization efficiency, thereby shortening the battery's lifespan. **Figure 2.5.** shows the HER bubbles observed during the battery cycling in the laboratory.

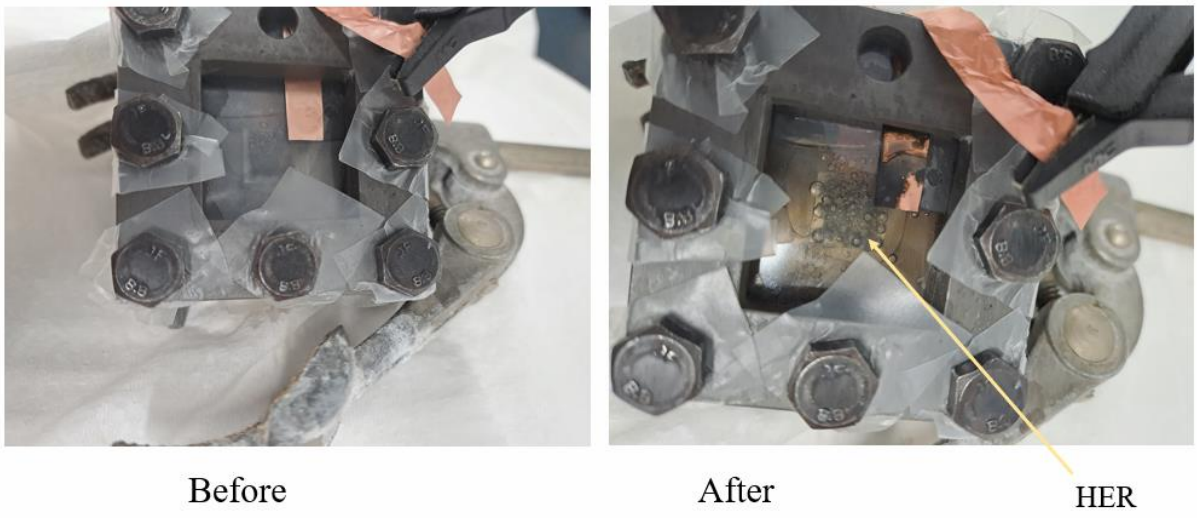

Figure 2. 5: The before and after picture of an assembled zinc-air battery with HER bubbles (pictures were taken in the lab during RZAB testing).

To circumvent this, alloying zinc electrodes with certain metals such as tin (Sn), bismuth (Bi), lead (Pd), cadmium (Cd), and indium (In) is known to suppress HER to a certain extent [23]. Coating the surface of the Zinc electrode with lithium boron oxide (Li_2O-$2B_2O_3$) or aluminium oxide (Al_2O_3) also suppresses HER [24,25]. Another suggested solution is adding inorganic additives such as silicates, PbO, $In(OH)_3$, In_2O_3, $Ca(OH)_2$, Tl_2O_3, Bi_2O_3 and Ga_2O_3 [25].

(i) Dendrite formation

Upon recharge, current density distribution at an electrode surface is not uniform which leads to a change in electrode shape resulting in dendrite formation. In the event that these dendrites reach the cathode side, the battery will experience a short circuit and get destroyed. **Figure 2.6** shows the dendrite growth observed on the polished zinc plate when cycling the RZAB in the laboratory.

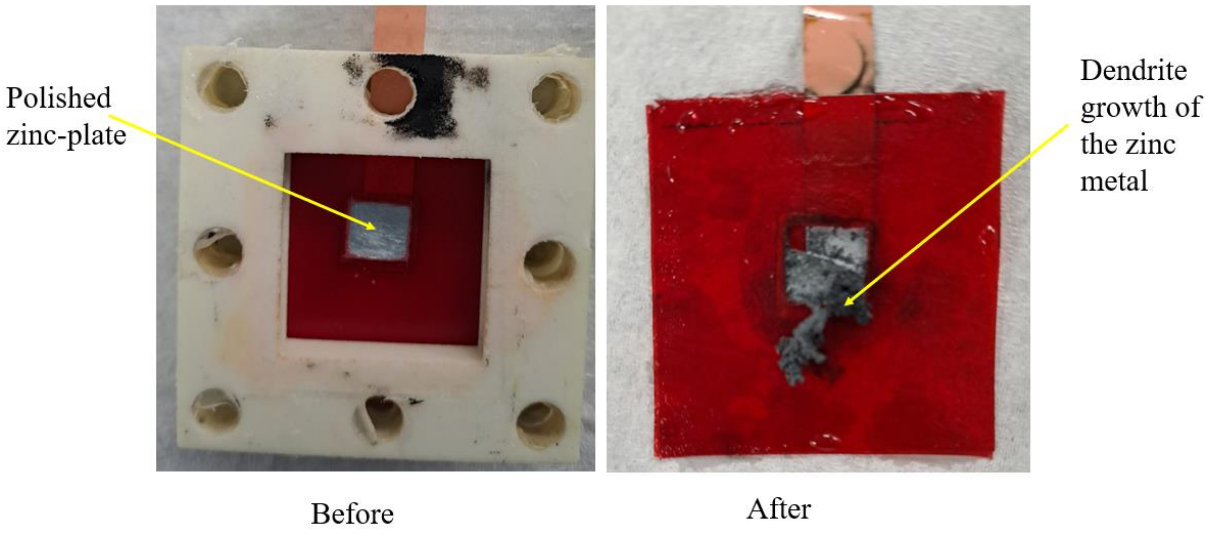

Figure 2. 6: Pictures showing the zinc plate before and after cycling (pictures were taken in the lab during RZAB testing).

To alleviate dendrite formation and improve the anode cyclability, near-neutral alkaline electrolytes can be used. Wang and coworkers used highly concentrated zinc-ion electrolyte (HCZE) to reduce H_2O activity [26]. The neutral pH of the HCZE was found to simultaneously stabilize the Zn and the air cathode. Although these non-alkaline electrolytes slow down Zn

metal corrosion and relieve dendrite growth during Zn plating, they can hinder RZAB performance. ORR and OER kinetics are much slower in neutral pH than in alkaline conditions due to the altered reaction pathway [6]. The surface passivation by resistive ZnO films also hinders the Zn anode activity in neutral electrolytes [6].

2.2.3.2. Air cathode

Oxygen electrocatalysis is becoming increasingly important in building sustainable energy infrastructure. Oxygen chemistry has limitations which prevent the effectiveness of renewable and eco-friendly technologies such as fuel cells and metal-air batteries. The ORR and OER at the air cathode have large overpotentials giving a limited round trip efficiency of $< 65\%$ in actual working conditions which is lower than that of standard lithium-ion batteries (energy efficiency of 80-90%) [6]. OER requires harsh electrochemical potentials which are detrimental to ORR by leaching transition metals and corroding carbon support therefore leading to poor cyclability of the cell [27]. The air cathode is also prone to polarization and rapid degradation during cycling which hinder the long-term operation of the ZABs. Reversing the ORR/OER processes possesses high energy barriers which makes the reactions sluggish. Thus, for practical ZAB applications, high-activity and robust oxygen electrocatalysts are a necessity.

2.2.4. Cathode materials for RZAB and suitable supports

Several studies proved that Pt-based noble catalysts demonstrate outstanding ORR catalytic activity, while Ir/Ru-based noble catalysts perform exceptionally well in OER [28–31]. The downside of Pt-based and Ir/Ru-based catalysts lies in their scarcity, high cost, short lifespan, and low ORR/OER catalytic selectivity [32]. Metal-free electrocatalysts have been at the forefront due to their high conductivity and reduced costs, however, when exposed to high OER potentials, they are easily prone to corrosion [32]. Recently, transition metal-based electrocatalysts have taken centre stage because of their abundance in nature and cost-

effectiveness. It has been demonstrated that low-cost transition metals such as Fe, Ni, Co, Mn, Mo, and Cu present potential catalytic activities for ORR and OER [33–36]. However, transition metal-based electrocatalysts suffer from drawbacks such as poor conductivity (due to semiconductive characteristics), instability, and low intrinsic activity. It is however noteworthy that transition metal-based catalysts stand close to noble metal-based catalysts in terms of catalytic activity and achieve higher corrosion resistance than metal-free catalysts.

Transition metal-based electrocatalysts can be partitioned into oxides [33,34], hydroxides [37,38] alloys [39,40], single atoms [41], nitrides [42,43] and phosphides [44,45]. The incompletely filled d orbitals of transition metals allow electron donation and redox reactions to be relatively rich thus they remain a viable option for oxygen reactions [32]. To circumvent the semiconducting properties of transition metal-based electrocatalysts, methods such as heteroatom doping [46], loading the catalyst with conductive materials [47] and nanosizing [48] were proposed. Loading conductive substances on transition metal-based catalysts is an effective solution to overcome their poor conductivity. This research thus explores the transition metal-based electrocatalysts loaded on carbon support.

2.2.4.1. High-entropy oxides

A compound's number of metal cations classifies it as either low, medium, or high entropy. Compounds with at least three metal cations are ascribed to low entropy, four metal cations to medium entropy and five metal cations to high entropy [49]. High entropy oxides (HEO) which were inspired by high entropy alloys (HEA) gained a lot of traction ever since their discovery. These are multicomponent materials which contain oxygen and five or more metallic elements which crystalize into a single-phase solution [50]. **Figure 2.7** shows an example of the arranged metals and oxygen atoms in a high entropy crystalline structure. For materials to be classified as high entropy, the configurational entropy should be ~1.61R therefore decreasing the number of metal ions to less than five significantly reduces the configurational entropy to ~1.39R [51].

The single lattice model of configurational entropy assumes that the components are equally likely to be arranged in any lattice configuration and can be calculated as follows:

$$S_{ss}^{conf} = -R \sum X_i \ln (X_i) \qquad (1)$$

Where R is the universal gas constant and x_i is the mole concentration of the cation [52].

Given that the components are in equiatomic proportions, equation (1) can be reduced to equation (2):

$$S_{ss}^{conf} = -Rln(n) \qquad (2)$$

Where n is the number of components or "entropy species" [52].

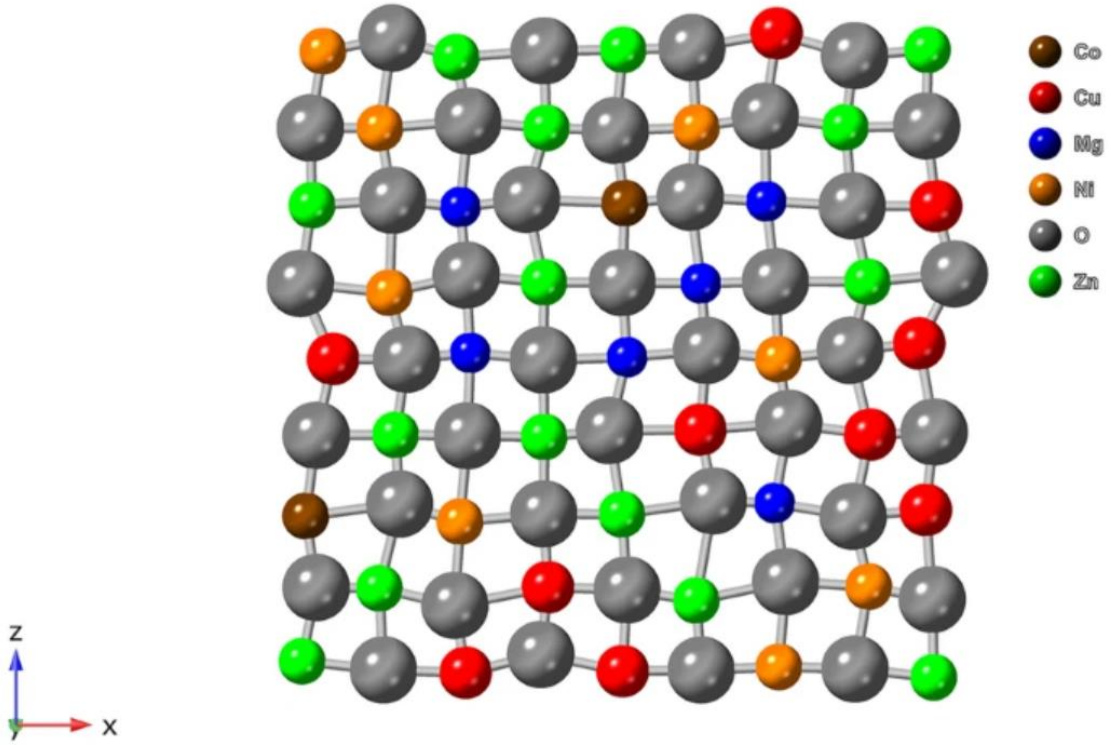

Figure 2. 7: A 2D slice of high entropy oxide displaying the lattice distortion effect [53].

The first HEOs were reported by Rost et al in which a mixed oxide was developed by occupying a single sublattice with numerous distinct cations [54]. The five-component oxide was engineered in such a way that cations were randomly and homogeneously distributed

promoting high entropy stabilization effect [54]. The numerous combinations of the metallic elements bring about desirable characteristics such as the high entropy effect, lattice distortion, sluggish diffusion and the cocktail effect. The lattice distortion and sluggish diffusion effect delay the atomic movement hence improving interface stability. **Figure 2.7** displays the lattice distortion effect. The cocktail effect produces unpredictable synergies since the combined effect of the metal ions is different from that of individual ions. An increase in configurational entropy facilitates the formation of a stable solid solution structure instead of a weak intermetallic compound and this is known as the "high-entropy effect" [50].

(i) Crystal structure of HEOs

HEOs can have a rock-salt structure like other oxides. Only one Wyckoff site is present for the cations in a rock salt structure therefore a well-dispersed structure with chemical stability can be achieved providing promising electrochemical application [51]. The first ever synthesized high entropy oxide with $Mg_{0.2}Co_{0.2}Ni_{0.2}Cu_{0.2}Zn_{0.2}O$ composition was a rock salt structure [54]. Mao et al also successfully synthesized an equimolar $(Co_{0.2}Cu_{0.2}Mg_{0.2}Ni_{0.2}Zn_{0.2})O$ HEO using the modified solution combustion synthesis (SCS) method [55]. The single-phase rock salt structure was achieved at a temperature of 1123 K. There are also single-phase HEO structures like perovskites, which can have cubic, orthorhombic, or hexagonal crystallography. They are composed of two cations molecules, one of which is a 12-fold coordination and the other a 6-fold coordination [56]. In these structures, an anion octahedral oxygen is also present. An easy-to-use one-pot combustion technique was used by Yang et al to produce single-phase perovskite HEO [57]. Among the other interesting groups, single-phase spinel HEOs exist, similar to the ones commonly found in oxides of single metals, such as spinel-Mn_3O_4 and spinel-Fe_3O_4. Stygar *et al* succeeded in forming spinel-type structured HEOs such as $(Co,Cr,Fe,Mg,Mn)_3O_4$, $(Cr,Fe,Mg,Mn,Ni)_3O_4$ and $(Co,Cr,Fe,Mn,Ni)_3O_4$ while varying the

metal composition [58]. Apart from the mentioned crystal structures, entropy-stabilized phases are fluorite, pyrochlore, and bixbyite as shown in **Figure 2.8**.

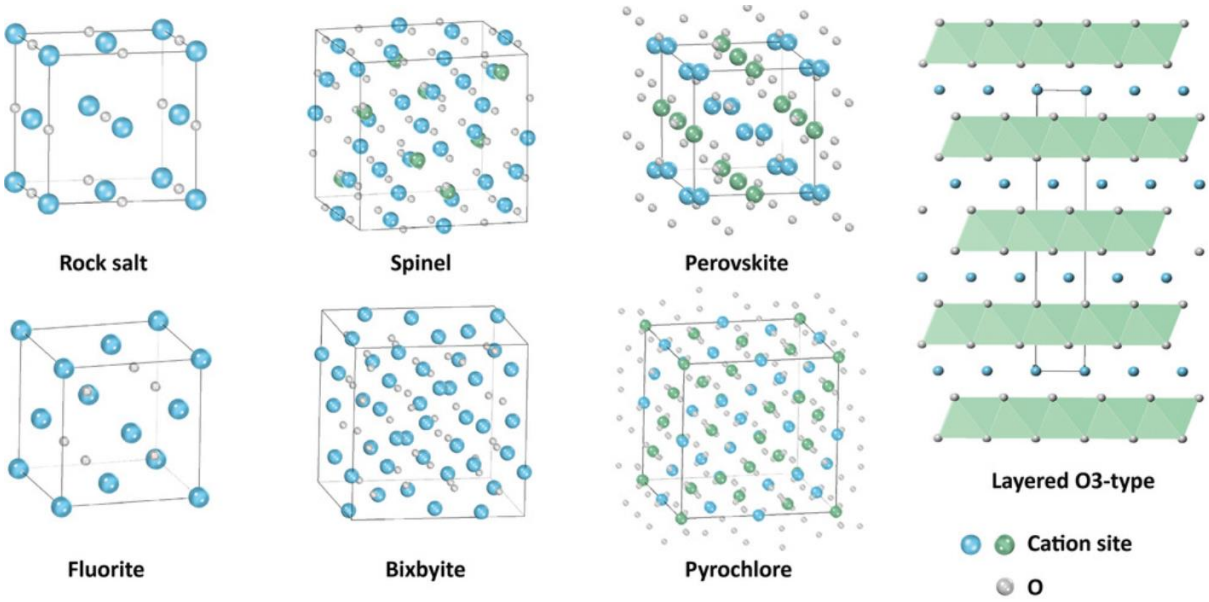

Figure 2. 8: Typical crystal structures of HEOs (Adapted from [51]).

This research particularly focuses on high entropy spinel oxides (HESO). Spinel oxides are materials with the formula AB_2O_4. They have widely attracted attention because of their excellent stability under battery working conditions, compositional flexibility and abundance of raw materials enabling efficient design of this structure as ORR/OER bifunctional electrocatalyst. Additionally, the formation of spinel structured materials requires low temperatures (200 ℃) compared to perovskites which are known for their higher calcination temperatures [59]. The various valence states of transition metals offer flexibility in the composition of spinel oxides thus leaving space for manipulation in the electronic structure of these materials for electrocatalysis.

In a unit cell of a spinel oxide, the cation distribution is variable. As a result, three types of structures can develop. A normal spinel is characterized by A occupying tetrahedral sites, B occupying octahedral sites and this is summed up as follows: $A_{Td}(B_2)_{Oh}O_4$ [59]. An inverse spinel allows half of B to occupy tetrahedral sites while A and the remainder of B to occupy

Octahedral sites giving $B_{Td}(AB)_{Oh}O_4$. The format of the complex spinel based on the rule is $(B_\lambda A_{1-\lambda})_{Td}(A_\lambda B_{2-\lambda})_{Oh}O_4$ $(0 < \lambda < 1)$ [60].

2.2.4.2. Iron-cobalt-based electrocatalysts

Among heavily investigated transition metal-based ORR/OER electrocatalysts are bimetallic (especially FeCo-based) oxides, alloys, hydroxides, oxyhydroxides and sulphides [61]. Transition metal oxides and alloys combined with carbon materials have been identified as one of the promising candidates for ORR and OER because the bond between metals can constitute intrinsic polarity and promote multiple valance states, significantly promoting ORR and OER [62]. There is a great deal of evidence which states that the 3d orbital electron number drastically affects the OER electrochemical activity of the catalysts which are transition metals based [63]. One of the ideal OER electrocatalysts would be Co^{2+} with a $t_{2g}^6e_g^1$ electronic configuration close to the optimal e_g filling [64]. Fe-based catalysts are known to have superior activity in the ORR, as demonstrated by the Fe-N_x-C system, which is comparable to Pt-based catalysts in terms of performance [65]. The strong synergistic effect between Co and Fe ions has led to several researchers recently developing electrocatalysts based on FeCo ions to use as potent and promising water-splitting and metal-air battery catalysts [63,66].

Factors that should be taken into consideration when choosing an excellent electrocatalyst.

- *The intrinsic catalytic activity*

The intrinsic catalytic activities of metal centres that are accessible on the surface and act as catalytic active centres are essential. This factor depends on the electronic structure of the electrocatalyst which in turn is controlled by the constituent's synergistic effect [61]. The energies of adsorption for intermediate species (which include O-O species formed during OER) at the metal sites are tuned into the ideal state by combining iron and cobalt. It is not

known what the nature of the actual catalytic active centres (Fe or Co) is in FeCo-based composites, but they exhibit enhanced catalytic activities in contrast with their monometallic counterparts [61].

- *The number of exposed metal active centres*

An additional factor to consider is the number of active metal centres exposed; the greater the number of active centres exposed, the higher the catalytic activity. Designing micro and nanostructures to expose more active metal centres and tuning the catalyst microscale can increase the number of exposed active metal centres. Metal centres are often exposed in large numbers in an open porous structure [61].

- *Conductivity*

To improve the conductivity of catalysts, the addition of conductivity-enhancing materials such as graphene and carbon nanotubes is vital. To date, oxygen chemistry has been tested on several FeCo-based catalysts which were prepared using various methods. For instance, FeCo metal-organic frameworks and FeCo-based alloys acquired composites embedded in carbon turned out to act as efficient oxygen chemistry catalysts and exhibit conductivity [61].

2.2.5. Onion-like carbon

The carbon onions are spherical or polyhedral carbon nanoparticles that are typically smaller than 10 nm, containing several fullerene-like carbon shells that have a defective or disordered structure to a certain extent [67]. Their small size, large external surface area and high conductivity make them appealing for energy storage applications [68–71]. OLC is typically synthesised from the high temperature annealing of nanodiamond particles with characteristic peaks at $2\theta = 43.7^{\circ}$ and 75.1° which correspond to the (111) and (220) diamond planes. A schematic representation of how carbon onions are structured is shown in **Figure 2.9**. The OLC has characteristic peaks at $2\theta = 25.7°$ and 42.5° corresponding to the (002) and (100) planes of

carbon. As an electrode material, OLC provides fast charge/discharge rates and shows suitable properties as a substrate for redox-active materials. Therefore, this type of carbon is a suitable candidate for application in batteries.

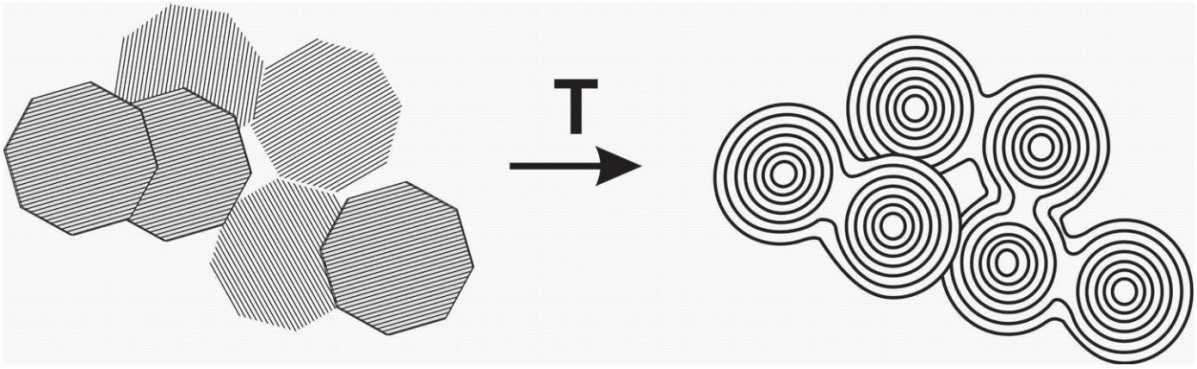

Figure 2. 9: A schematic representation of the onion-like carbon conglomerate formation from nanodiamonds (Adapted from [72]).

2.2.6. Zinc anode utilization.

In zinc-air batteries, shallow cycling remains one of the pitfalls which hamper the advancement in fully realizing electrically rechargeable zinc–air batteries. The cathode receives an inexhaustible oxygen supply from the environment; therefore, the zinc anode is the limiting electrode in the zinc-air configuration leading to battery operation termination. Despite this challenge, the zinc anode receives far less attention than it deserves. Balancing the zinc anode is of utmost importance in fully realizing the rechargeability of zinc-air batteries therefore excess zinc metal not involved in the electrochemical reaction should be greatly reduced. Maximizing zinc usage while maintaining cyclability is essential and the concept of zinc utilization, known as the depth of discharge (DOD) should be considered when cycling the battery [73]. Despite this, most reports in the currently available literature use excessive zinc amounts as anodes to demonstrate rechargeability with zinc-air batteries [74–77]. These reports use cycling protocols ranging from hundreds to thousands of cycles. Although the number of cycles is a valuable measure of the battery quality, it does not directly imply that the battery is

rechargeable. In contrast, if only 1% of the active material is consumed per cycle, one could theoretically achieve 100 discharge cycles without recharging the battery [73]. There is enormous difficulty in determining rechargeability for batteries that undergo shallow cycling therefore it is recommended that zinc-air batteries be cycled at an areal energy density of 35 $mWhcm^{-2}$ to compete with the lithium-ion battery pack [73,78]. It is additionally necessary for a zinc-air battery to have a minimum DOD of 0.20 (~20%) to meet the 100 Wh kg^{-1} technologically suitable threshold [11]. Multitudes of electrocatalysts for air-breathing electrodes have been investigated to aid with the rechargeability of zinc-air batteries, however, because of the cycling protocols that are not standardized, it is difficult to determine whether these variations are effective. Seventy (70) publications were reviewed in **Table 2.1** and only 7 meet the minimum metrics for translating these devices into technologically relevant devices. The last 7 publications highlighted in **Table 2.1** met the standards and they all have an areal energy of more than 35 mWh cm^{-2} which translates to more than 20% DOD.

Table 2. 1. Zn-air rechargeable batteries: a survey of electrocatalysts used as air-breathing electrodes. When multiple cycling experiments were provided, we selected the data that yielded the highest areal discharge energy from each report.

Year	**Catalyst**	**Current density [$mAcm^{-2}$]**	**Discharge Time [min]**	**Discharge Voltage [V]**	**Areal energy [$mWhcm^{-2}$]**	**Cycle life**	**References**
2020	AlNiCoRuMo	10	30	1.20	6.0	80 h	[79]
2022	AlNiCoRuMoCrFeTi	10	60	1.10	11.0	300 h / 150 cycles	[80]
2021	np−AlCoFeMoCr/Pt	20	30	1.12	11.2	50 cycles	[81]
2022	AlNiCoFeCrMoV-based HEO/CoNC	10	30	1.10	5.5	125 h / Cycles	[82]
2023	CrMnFeCoNi	8	10	1.10	1.47	720 cycles	[83]
2023	$Fe_{12}Ni_{23}Cr_{10}Co_{30}Mn_{25}$/CNT	5	7.5	1.20	0.75	256 h	[84]

2022	$Mn_{70}Ni_{7.5}Cu_{7.5}Co_{4.2}V_{4.2}Fe_2Mo_2Pd_{0.5}Pt_{0.5}Au_{0.5}Ru_{0.5}Ir_{0.5}$ Alloy (np-12)	10	30	1.16	5.8	240 cycles	[85]
2023	FeCoNiMnCu-1000(1 : 1)	10	10	1.10	1.83	200 h / 1005 cycles	[86]
2023	FeNiCoMnRu@CNT	-	-	-	-	-	[87]
2022	(PtPdAuAgCuIrRu) clusters@ $(AlNiCoFeCrMoTi)_3O_4$	10	30	1.20	6.0	250 cycles	[88]
2022	MnNiCuCoVFeMoPdPtAu RuIr/NG	2	30	1.25	1.25	300 h / 300 cycles	[89]
2020	AlFeCoNiCr	20	5	1.15	1.92	120 h / 720 cycles	[90]
2023	$Fe_6Ni_{20}Co_2Mn_2Cu_{1.5}$@rGO	10	30	1.1	5.5	300 h	[91]
2023	Co-N-C@ CoNiFe-LDH	5	5	1.18	0.492	950 h	[92]
2021	CC3	10	30	1.23	6.15	120 h / cycles	[93]

2016	NCNF-1000	10	5	1.20	1	83 h / 500 cycles	[94]
2015	NCNT/CoO-NiO-NiCo	20	5	1.22	2.03	100 cycles	[95]
2022	MoNiFe	10	-	1.20	-	450 cycles	[96]
2020	FeCo/ Co_2P@NPCF	10	5	1.15	0.958	642 cycles	[66]
2019	FeCo/FeCoNi@NCNTs-HF	5	20	1.21	2.02	240 h / 360 cycles	[97]
2021	FeCo-1/NSC	5	30	1.23	3.08	150 h	[98]
2023	FeCo/Co−N−C	50	-	1.22	-	-	[99]
2017	N-GCNT/FeCo-3	120	5	0.71	7.1	40 h / 240 cycles	[100]
2021	NPC/FeCo@NCNT	10	-	1.26	-	100 cycles	[101]
2020	FeCo/FeN2/ NHOPC	10	25	1.25	5.21	120 cycles	[102]
2023	Co/FeCo@$Fe(Co)_3O_4$	10	5	1.21	1.01	1000 cycles	[103]

2022	FeCo/LNCNT	5	20	1.1	1.83	400 h / 600 cycles	[104]
2023	FeCo@MNC	5	30	1.2	3.0	33.3 h / 33 cycles (est)	[105]
2023	FeOOH-CNT-FeCo/NC	10	5	1.27	1.09	229 h / 686 cycles	[106]
2019	FeCo@MNC	20	5	0.9	1.5	24 h	[107]
2022	FeCo@Co/N-C-8	5	-	1.18	-	200 h	[108]
2023	NF/CCO/FCH	10	10			1000 cycles	[109]
2021	CoNC@LDH	50	5	0.84	3.5	650 cycles	[110]
2015	NPMC-1000	2	5	1.0	0.167	30 h / 180 cycles	[111]
2017	Ni_3FeN	10	10	1.22	2.03	100 h / 310 cycles	[112]
2020	FeCoMoS@NG	2	5	1.20	0.2	70 h	[113]

2019	Co-Mn-Ni ternary spinel oxides (CMN-231)	10	5	1.23	1.025	100 cycles	[114]
2019	FeCoNi-CNF	20	5	0.90	1.5	22 h	[115]
2022	$Fe_4Co_1Ni_2$@hNCTs	10	10	1.14	1.19	110 h / 310 cycles	[116]
2017	Ternary spinel oxides, $M_{0.1}Ni_{0.9}Co_2O_4$ (M: Mn, Fe, Cu, Zn) (FNCO-01)	10	20	1.18	3.93	100 cycles	[117]
2022	Ternary $Pd_{45}Pt_{44}Ni_{11}$ SpNSs/C	10	10	1.10	1.83	220 h / 660 cycles	[118]
2021	MnCoNi-C-D	10	15	1.20	3.0	180 h	[119]
2022	Ox-MnCoNi-C	10	10	1.23	2.05	100 h / 303 cycles	[120]
2021	FeCoNi@HNC	5	10	1.22	1.02	200 cycles	[121]
2023	NiCoO2@NiCo LDH	10	15	1.18	2.95	260 h / 520 cycles	[122]

2024	Fe-NP/MNCF	-	-	-	-	180 h	[123]
2024	Co-NCS-5||Co2P-NCS-60	9.8	10	1.130	1.85	60 h	[124]
2024	Fe–N_4SP/NPS-HC	5	3.33	1.20	0.333	320 h / 2880 cycles	[125]
2024	$Fe_{3\%}Co_{3\%}Ni_{9\%}$-NC1000	5	10	1.25	1.04	250 h / 750 cycles	[126]
2024	Fe-FeN-C	10	5	1.2	1	407 h	[127]
2024	$CoMoO_4$-RuO_2	5	5	1.2	0.5	110 h	[128]
2024	CoN/MnO@NC	10	10	1.25	2.08	480 h / 720 cycles	[129]
2024	CoN_3NLF	5	-	1.2	-	300 h	[130]
2024	MnO-CeO_2@Cs + RuO_2	5	10	1.25	1.04	297 h	[131]
2023	Co/ Co_7Fe_3@PNCC	10	10	1.2	2	800 h	[132]
2024	FeCo-MI@TAP-900	5	20	1.1	1.83	1400 h / 2100 cycles	[133]
2024	FeCo/Co_2P/Fe_2P@NPC	10	120	1.1	22.0	720 h	[134]

2024	LSCNiO	2	5	1.17	0.195	166 h	[135]
2024	N, B, and F-doped PCNF	5	5	1.2	0.5	100 h	[136]
2024	Co–N–C 800	5	10	1.2	1	145.3 h / 430 cycles	[137]
2024	Ni-CAT/NiFe-LDH/CNFs	1	6	1.4	0.14	66 h	[138]
2023	$Fe_{0.2}Co_{0.8}$/N-C	10	10	1.27	2.12	550 h / 1650 cycles	[139]
2024	S-VN/Co/NS-MC	5	10	1.06	0.883	250 h	[140]
2024	$NiMoO_4 \cdot xH_2O$	5	9	1.2	0.9	1100 min / 60 cycles	[141]
2015	Directly grown MnO_x	15	120	1.27	38.2	15 cycles	[142]
2017	$Fe_{0.5}Co_{0.5}O_x$/NrGO	25	100.2	1.12	46.76	16 cycles	[143]
2014	dp-$MnCo_2O_4$/CNT	10	240	1.22	48.80	64 cycles / 768 h	[144]
2015	Co_3O_4 Nps	2	1500	1.20	60	5 cycles	[145]
2018	Co–N_x/C NRA	50	120	1.11	111	80 h / 20 cycles	[146]

2013	CoO/N-CNT and NiFe LDH	20	600	1.22	244	200 h / 10 cycles	[16]
2018	Ternary $Ni_{46}Co_{40}Fe_{14}$ (C@ NCF-900)	50	360	1.25	375	8 cycles	[147]

2.3. Electrochemical techniques

2.3.1. Voltammetry

Voltammetry refers to techniques in which a working electrode's potential is controlled and a current flow is measured.

2.3.1.1. Linear sweep voltammetry (LSV)

LSV is a technique which involves linearly scanning either a negative or a positive potential over time. In LSV, electrodes are dipped in a solution with an excess of supporting electrolyte to prevent the migration of charged reactants and products, so that electroactive species can only diffuse between electrode surfaces. The potential at the working electrode is changed linearly with time starting at potentials where no electrode reactions occur and moving to potentials where analytes are reduced (more negative values) or oxidised (more positive values) as demonstrated in **Figure 2.10 (a)**. The current is applied throughout the experiment with the resulting current-potential curve displayed in **Figure 2.10 (b)**. The parameters in a typical linear voltammogram are: i_p which is the peak current (maximum current value), E_p which is the peak potential (corresponding to i_p) and $E_{p/2}$ which is the half peak potential (the potential where $i = i_{p/2}$).

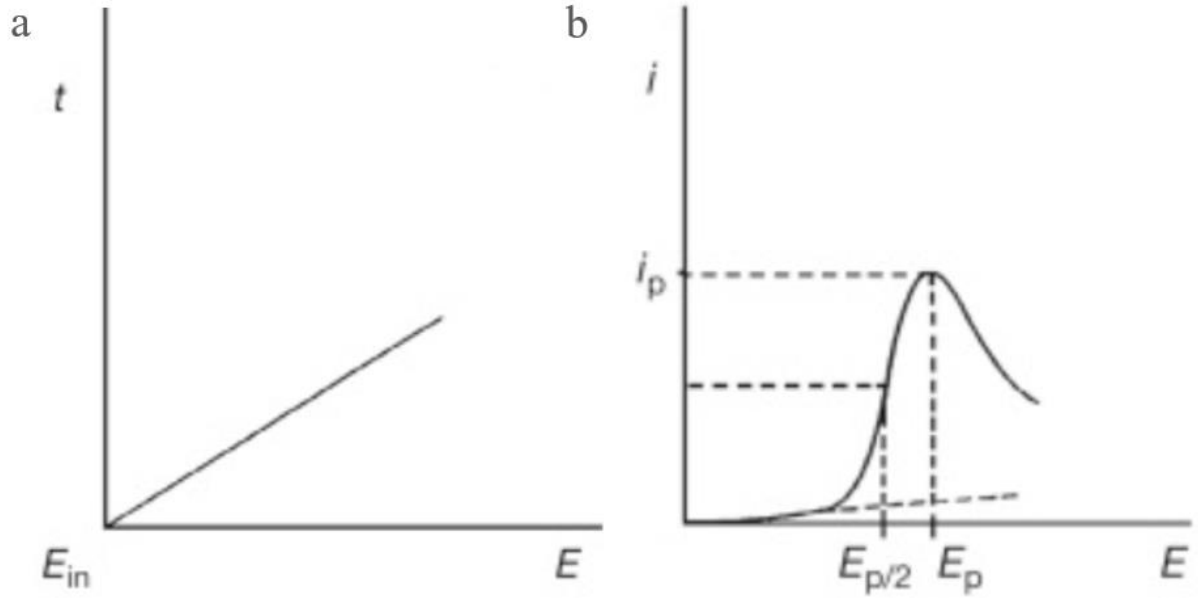

Figure 2. 10: (a) Potential waveforms of linear sweep voltammetry and (b) the corresponding voltammogram [148].

The ORR and OER behaviours are best visualized using LSV curves as demonstrated in **Figure 2.11**. The curves are obtained from RDE experiments and some kinetic parameters are indicated. Onset potential (E_{onset}) is the potential where ORR/OER starts. $E_{1/2}$ is the half-wave potential, and it is described as the potential where the diffusion-limiting current density reaches half. J_d is the diffusion-limited current density which is achieved by maintaining diffusion limits and ensuring the maximum transfer rate of the electrochemical species. η_{ORR} and η_{OER} are the overpotentials for ORR and OER respectively. An overpotential is a potential difference between ORR/OER catalytic potentials and the equilibrium potential (1.23V). The lower the overpotential, the easier it is to facilitate the oxygen reactions.

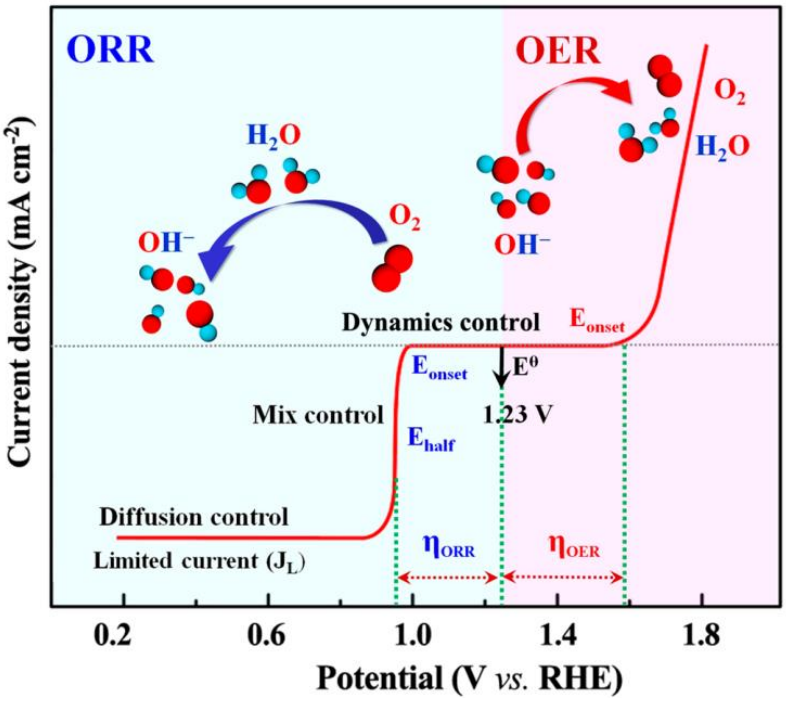

Figure 2. 11: ORR/OER polarization curves (Adapted from [60]).

Another interesting use of LSV in this research project was to obtain the discharge polarization curve for the ZAB and convert it to the power density curve (obtained by current density × voltage) (**Figure 2.12**). Therefore, the power density is simply the relationship between voltage and current density when a zinc-air battery is discharged. It is noticeable that with increasing current density, the voltage decreases. The discharge curve is divided into three regions, namely, activation, Ohm, and concentration polarization regions [59]. The activation polarization is mainly controlled by the ORR kinetics of the electrocatalyst, the Ohm polarization relies on the ionic resistance of the electrolyte while the concentration polarization occurs when O_2 is rapidly consumed at the air cathode [59].

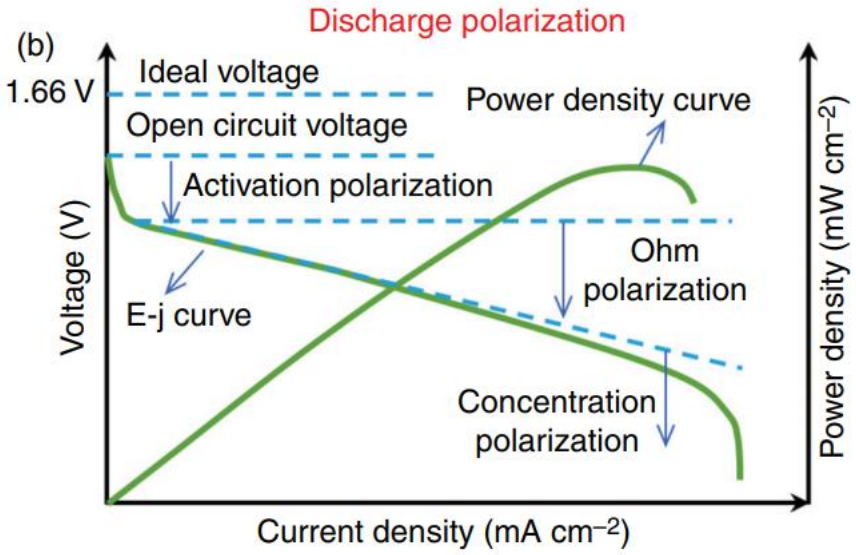

Figure 2. 12: Typical polarization curve of a zinc-air battery (adapted from [59].

2.3.1.2. Cyclic voltammetry

Cyclic voltammetry (CV) is an electrochemical technique commonly used to study the electron transfer-instigated chemical reactions of molecular species. The two main processes in a typical cyclic voltammogram include oxidation and reduction. Oxidation is the loss of electrons while reduction is the accumulation of electrons thus these reactions are dependent on one another. In a cyclic voltammogram, potential (E) (x-axis) is applied resulting in a current (i) (y-axis)

response as depicted in **Figure 2.13**. The region where charges (e.g. electrons) are transferred is called the faradaic region. The electron transfer causes oxidation or reduction to occur. The non-faradaic region is the region where oxidation or reduction (no electron transfer) does not occur. This region is the capacitive current region as demonstrated in **Figure 2.13**. To calculate the electrochemical active surface area (ECSA), the non-faradaic region is used.

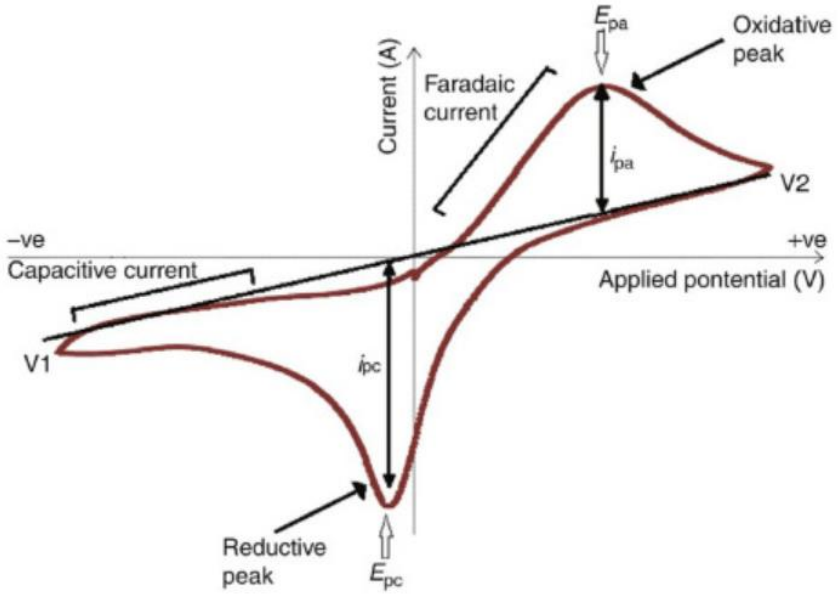

Figure 2. 13: A typical cyclic voltammogram depicting peak potential (E_{pc}) and peak current (i_{pa}) (Adapted from [148]).

2.3.2. Chronopotentiometry

Chronopotentiometry (CP) is an electrochemical technique in which a current pulse is applied at the working electrode while the potential is measured against the reference electrode for a given period. This technique is used to evaluate the electrocatalysis and the kinetic performances such as transport and adsorption near the electrode surface [150]. It is also commonly used during battery charge and discharge experiments. The measured potential changes suddenly when the current is first applied due to iR loss, and gradually thereafter as

concentration overpotential develops at the electrode surface as the concentration of the reactant is exhausted [151].

There are different types of chronopotentiometry techniques as shown in **Figure 2.14**. A constant current chronopotentiometry involves the application of anodic or cathodic current causing the oxidation or reduction of electroactive species at a constant rate (**Figure 2.14 (a)**). In response to the change in reaction ratio, the electrode potential fluctuates over time. For linearly rising current chronopotentiometry, the current is varied linearly instead of being kept constant (**Figure 2.14 (b)**). In current reversal chronopotentiometry, a sudden change in current from anodic to cathodic reduces the anodic product formed by the anodic reaction and the potential moves in as the cathodic product concentration increases (**Figure 2.14 (c)**). In cyclic chronopotentiometry, the process is repeatedly reversed (**Figure 2.14 (d)**). To determine a battery's specific capacity and to evaluate its cycling stability, cyclic chronopotentiometry and current reversal are often used.

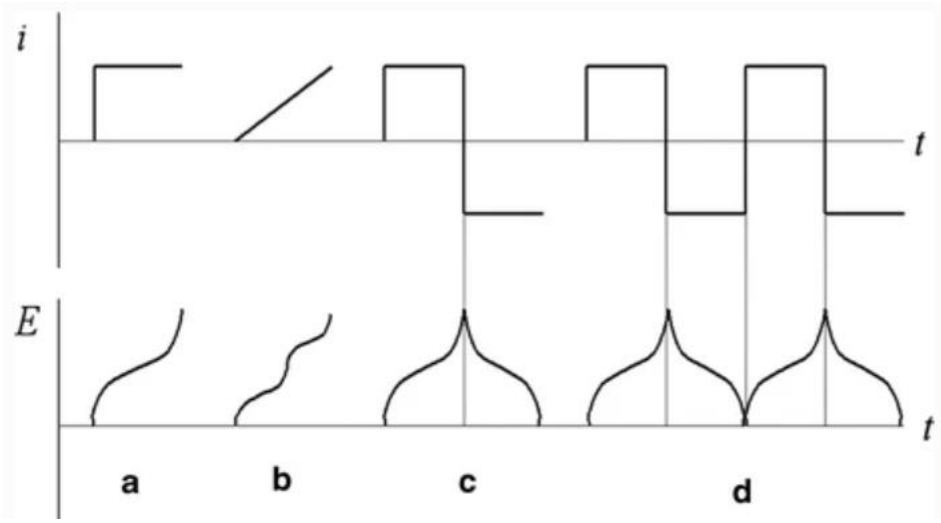

Figure 2. 14: Various types of chronopotentiometry experiments (a) chronopotentiometry at constant current (b) linearly rising current chronopotentiometry (c) current reversal chronopotentiometry (d) cyclic chronopotentiometry (adapted from [151]).

References

. (1) Olabi, A. G.; Abdelkareem, M. A. Energy Storage Systems towards 2050. Energy. Elsevier Ltd March 15, 2021. https://doi.org/10.1016/j.energy.2020.119634.

(2) Olabi, A. G. Renewable Energy and Energy Storage Systems. Energy. Elsevier Ltd 2017, pp 1–6. https://doi.org/10.1016/j.energy.2017.07.054.

(3) Zakeri, B.; Syri, S. Electrical Energy Storage Systems: A Comparative Life Cycle Cost Analysis. Renewable and Sustainable Energy Reviews. Elsevier Ltd 2015, pp 569–596. https://doi.org/10.1016/j.rser.2014.10.011.

(4) Olabi, A. G.; Onumaegbu, C.; Wilberforce, T.; Ramadan, M.; Abdelkareem, M. A.; Al – Alami, A. H. Critical Review of Energy Storage Systems. Energy 2021, 214. https://doi.org/10.1016/j.energy.2020.118987.

(5) Olabi, A. G.; Sayed, E. T.; Wilberforce, T.; Jamal, A.; Alami, A. H.; Elsaid, K.; Rahman, S. M. A.; Shah, S. K.; Abdelkareem, M. A. Metal-Air Batteries—a Review. Energies. MDPI November 1, 2021. https://doi.org/10.3390/en14217373.

(6) Zhang, J.; Zhou, Q.; Tang, Y.; Zhang, L.; Li, Y. Zinc-Air Batteries: Are They Ready for Prime Time? Chem Sci 2019, 10 (39), 8924–8929. https://doi.org/10.1039/c9sc04221k.

(7) Grande, L.; Paillard, E.; Hassoun, J.; Park, J. B.; Lee, Y. J.; Sun, Y. K.; Passerini, S.; Scrosati, B. The Lithium/Air Battery: Still an Emerging System or a Practical Reality? Advanced Materials 2015, 27 (5), 784–800. https://doi.org/10.1002/adma.201403064.

(8) Li, C. S.; Sun, Y.; Gebert, F.; Chou, S. L. Current Progress on Rechargeable Magnesium–Air Battery. Adv Energy Mater 2017, 7 (24). https://doi.org/10.1002/aenm.201700869.

(9) Liu, X.; Jiao, H.; Wang, M.; Song, W. li; Xue, J.; Jiao, S. Current Progresses and Future Prospects on Aluminium–Air Batteries. International Materials Reviews. Taylor and Francis Ltd. 2022, pp 734–764. https://doi.org/10.1080/09506608.2021.2006968.

(10) Banerjee, S.; Grover, V. Super Capacitors Review on Electrochemical Capacitor Technology: Role of Transition Metal-Based Oxides.

(11) Parker, J. F.; Ko, J. S.; Rolison, D. R.; Long, J. W. Translating Materials-Level Performance into Device-Relevant Metrics for Zinc-Based Batteries. Joule. Cell Press December 19, 2018, pp 2519–2527. https://doi.org/10.1016/j.joule.2018.11.007.

(12) Liu, J. N.; Zhao, C. X.; Wang, J.; Ren, D.; Li, B. Q.; Zhang, Q. A Brief History of Zinc-Air Batteries: 140 Years of Epic Adventures. Energy and Environmental Science. Royal Society of Chemistry September 26, 2022, pp 4542–4553. https://doi.org/10.1039/d2ee02440c.

(13) R 107]. https://royalsocietypublishing.org/.

(14) Grove-1997-Experiments-on-the-Gas-Voltaic-Battery-with-a-View-of-Ascertaining-the-Rationale-of-Its-Action-and-on-Its.

(15) Storey, O. W.; Birdsall, C. C.; Cahoon, N. C.; Thomas, U. B.; Howard, P. L.; White, J. C.; Herbert, W. S.; Kirk, R. C.; Morehouse, C. K.; Ellis, G. B.; Booe, J. M.; Heise, G. W.; Hackernmn, N.; Schumacher, E. A.; Vosburgh, W. C.; Brooks, P. S.; Coleman, J. J.; Musgrave, J.; Heise, G. W. THE ANNIVERSARY ISSUE ON PRIMARY CELL SYSTEMS FOREWORD Dry Cells of the Leclanch Type, 1902-1952-A Review.

(16) Li, Y.; Gong, M.; Liang, Y.; Feng, J.; Kim, J. E.; Wang, H.; Hong, G.; Zhang, B.; Dai, H. Advanced Zinc-Air Batteries Based on High-Performance Hybrid Electrocatalysts. Nat Commun 2013, 4. https://doi.org/10.1038/ncomms2812.

(17) Liu, X.; Yuan, Y.; Liu, J.; Liu, B.; Chen, X.; Ding, J.; Han, X.; Deng, Y.; Zhong, C.; Hu, W. Utilizing Solar Energy to Improve the Oxygen Evolution Reaction Kinetics in Zinc–Air Battery. Nat Commun 2019, 10 (1). https://doi.org/10.1038/s41467-019-12627-2.

(18) Gu, P.; Zheng, M.; Zhao, Q.; Xiao, X.; Xue, H.; Pang, H. Rechargeable Zinc-Air Batteries: A Promising Way to Green Energy. Journal of Materials Chemistry A. Royal Society of Chemistry 2017, pp 7651–7666. https://doi.org/10.1039/c7ta01693j.

(19) Amiinu, I. S.; Liu, X.; Pu, Z.; Li, W.; Li, Q.; Zhang, J.; Tang, H.; Zhang, H.; Mu, S. From 3D ZIF Nanocrystals to Co–Nx/C Nanorod Array Electrocatalysts for ORR, OER, and Zn–Air Batteries. Adv Funct Mater 2018, 28 (5). https://doi.org/10.1002/adfm.201704638.

(20) Spendelow, J. S.; Wieckowski, A. Electrocatalysis of Oxygen Reduction and Small Alcohol Oxidation in Alkaline Media. Physical Chemistry Chemical Physics 2007, 9 (21), 2654–2675. https://doi.org/10.1039/b703315j.

(21) Sun, Y.; Sun, S.; Yang, H.; Xi, S.; Gracia, J.; Xu, Z. J. Spin-Related Electron Transfer and Orbital Interactions in Oxygen Electrocatalysis. Advanced Materials. Wiley-VCH Verlag October 1, 2020. https://doi.org/10.1002/adma.202003297.

(22) Ipadeola, A. K.; Haruna, A. B.; Gaolatlhe, L.; Lebechi, A. K.; Meng, J.; Pang, Q.; Eid, K.; Abdullah, A. M.; Ozoemena, K. I. Efforts at Enhancing Bifunctional Electrocatalysis and Related Events for Rechargeable Zinc-Air Batteries. ChemElectroChem 2021, 1–22. https://doi.org/10.1002/celc.202101284.

(23) Li, Y.; Dai, H. Recent Advances in Zinc-Air Batteries. Chemical Society Reviews. Royal Society of Chemistry August 7, 2014, pp 5257–5275. https://doi.org/10.1039/c4cs00015c.

(24) Lee, S. M.; Kim, Y. J.; Eom, S. W.; Choi, N. S.; Kim, K. W.; Cho, S. B. Improvement in Self-Discharge of Zn Anode by Applying Surface Modification for Zn-Air Batteries with High Energy Density. J Power Sources 2013, 227, 177–184. https://doi.org/10.1016/j.jpowsour.2012.11.046.

(25) Cho, Y. Da; Fey, G. T. K. Surface Treatment of Zinc Anodes to Improve Discharge Capacity and Suppress Hydrogen Gas Evolution. In Journal of Power Sources; Elsevier B.V., 2008; Vol. 184, pp 610–616. https://doi.org/10.1016/j.jpowsour.2008.04.081.

(26) Wang, F.; Borodin, O.; Gao, T.; Fan, X.; Sun, W.; Han, F.; Faraone, A.; Dura, J. A.; Xu, K.; Wang, C. Highly Reversible Zinc Metal Anode for Aqueous Batteries. Nat Mater 2018, 17 (6), 543–549. https://doi.org/10.1038/s41563-018-0063-z.

(27) Li, Y.; Lu, J. Metal-Air Batteries: Will They Be the Future Electrochemical Energy Storage Device of Choice? ACS Energy Letters. American Chemical Society June 9, 2017, pp 1370–1377. https://doi.org/10.1021/acsenergylett.7b00119.

(28) Reier, T.; Oezaslan, M.; Strasser, P. Electrocatalytic Oxygen Evolution Reaction (OER) on Ru, Ir, and Pt Catalysts: A Comparative Study of Nanoparticles and Bulk Materials. ACS Catal 2012, 2 (8), 1765–1772. https://doi.org/10.1021/cs3003098.

(29) Cherevko, S.; Geiger, S.; Kasian, O.; Kulyk, N.; Grote, J. P.; Savan, A.; Shrestha, B. R.; Merzlikin, S.; Breitbach, B.; Ludwig, A.; Mayrhofer, K. J. J. Oxygen and Hydrogen Evolution Reactions on Ru, RuO2, Ir, and IrO2 Thin Film Electrodes in Acidic and Alkaline Electrolytes: A Comparative Study on Activity and Stability. Catal Today 2016, 262, 170–180. https://doi.org/10.1016/j.cattod.2015.08.014.

(30) Lim, B.; Jiang, M.; Camargo, P. H. C.; Cho, E. C.; Tao, J.; Lu, X.; Zhu, Y.; Xia, Y. Pd-Pt Bimetallic Nanodendrites with High Activity for Oxygen Reduction. https://www.science.org.

(31) Jia, Q.; Caldwell, K.; Strickland, K.; Ziegelbauer, J. M.; Liu, Z.; Yu, Z.; Ramaker, D. E.; Mukerjee, S. Improved Oxygen Reduction Activity and Durability of Dealloyed PtCox Catalysts for Proton Exchange Membrane Fuel Cells: Strain, Ligand, and Particle Size Effects. ACS Catal 2015, 5 (1), 176–186. https://doi.org/10.1021/cs501537n.

(32) Wei, L.; Ang, E. H.; Yang, Y.; Qin, Y.; Zhang, Y.; Ye, M.; Liu, Q.; Li, C. C. Recent Advances of Transition Metal Based Bifunctional Electrocatalysts for Rechargeable Zinc-Air Batteries. Journal of Power Sources. Elsevier B.V. November 30, 2020. https://doi.org/10.1016/j.jpowsour.2020.228696.

(33) Gong, M.; Dai, H. A Mini Review of NiFe-Based Materials as Highly Active Oxygen Evolution Reaction Electrocatalysts. Nano Research. Tsinghua University January 1, 2015, pp 23–39. https://doi.org/10.1007/s12274-014-0591-z.

(34) Zhu, H.; Zhang, S.; Huang, Y. X.; Wu, L.; Sun, S. Monodisperse MxFe3-XO4 (M = Fe, Cu, Co, Mn) Nanoparticles and Their Electrocatalysis for Oxygen Reduction Reaction. Nano Lett 2013, 13 (6), 2947–2951. https://doi.org/10.1021/nl401325u.

(35) Zhang, K.; Zhang, L.; Chen, X.; He, X.; Wang, X.; Dong, S.; Han, P.; Zhang, C.; Wang, S.; Gu, L.; Cui, G. Mesoporous Cobalt Molybdenum Nitride: A Highly Active Bifunctional Electrocatalyst and Its Application in Lithium-O2 Batteries. Journal of Physical Chemistry C 2013, 117 (2), 858–865. https://doi.org/10.1021/jp310571y.

(36) Fan, X.; Peng, Z.; Ye, R.; Zhou, H.; Guo, X. M3C (M: Fe, Co, Ni) Nanocrystals Encased in Graphene Nanoribbons: An Active and Stable Bifunctional Electrocatalyst

for Oxygen Reduction and Hydrogen Evolution Reactions. ACS Nano 2015, 9 (7), 7407–7418. https://doi.org/10.1021/acsnano.5b02420.

(37) Majee, R.; Islam, Q. A.; Bhattacharyya, S. Surface Charge Modulation of Perovskite Oxides at the Crystalline Junction with Layered Double Hydroxide for a Durable Rechargeable Zinc-Air Battery. ACS Appl Mater Interfaces 2019, 11 (39), 35853–35862. https://doi.org/10.1021/acsami.9b09299.

(38) Guo, X.; Hu, X.; Wu, D.; Jing, C.; Liu, W.; Ren, Z.; Zhao, Q.; Jiang, X.; Xu, C.; Zhang, Y.; Hu, N. Tuning the Bifunctional Oxygen Electrocatalytic Properties of Core-Shell Co3O4@NiFe LDH Catalysts for Zn-Air Batteries: Effects of Interfacial Cation Valences. ACS Appl Mater Interfaces 2019, 11 (24), 21506–21514. https://doi.org/10.1021/acsami.9b04217.

(39) Su, C. Y.; Cheng, H.; Li, W.; Liu, Z. Q.; Li, N.; Hou, Z.; Bai, F. Q.; Zhang, H. X.; Ma, T. Y. Atomic Modulation of FeCo–Nitrogen–Carbon Bifunctional Oxygen Electrodes for Rechargeable and Flexible All-Solid-State Zinc–Air Battery. Adv Energy Mater 2017, 7 (13). https://doi.org/10.1002/aenm.201602420.

(40) Wu, X.; Chen, F.; Jin, Y.; Zhang, N.; Johnston, R. L. Silver-Copper Nanoalloy Catalyst Layer for Bifunctional Air Electrodes in Alkaline Media. ACS Appl Mater Interfaces 2015, 7 (32), 17782–17791. https://doi.org/10.1021/acsami.5b04061.

(41) Zhang, W.; Zheng, W. Single Atom Excels as the Smallest Functional Material. Adv Funct Mater 2016, 26 (18), 2988–2993. https://doi.org/10.1002/adfm.201600240.

(42) Fu, G.; Cui, Z.; Chen, Y.; Li, Y.; Tang, Y.; Goodenough, J. B. Ni3Fe-N Doped Carbon Sheets as a Bifunctional Electrocatalyst for Air Cathodes. Adv Energy Mater 2017, 7 (1). https://doi.org/10.1002/aenm.201601172.

(43) Zhu, C.; Yin, Z.; Lai, W.; Sun, Y.; Liu, L.; Zhang, X.; Chen, Y.; Chou, S. L. Fe-Ni-Mo Nitride Porous Nanotubes for Full Water Splitting and Zn-Air Batteries. Adv Energy Mater 2018, 8 (36). https://doi.org/10.1002/aenm.201802327.

(44) Yang, H.; Zhang, Y.; Hu, F.; Wang, Q. Urchin-like CoP Nanocrystals as Hydrogen Evolution Reaction and Oxygen Reduction Reaction Dual-Electrocatalyst with Superior Stability. Nano Lett 2015, 15 (11), 7616–7620. https://doi.org/10.1021/acs.nanolett.5b03446.

(45) Anantharaj, S.; Ede, S. R.; Sakthikumar, K.; Karthick, K.; Mishra, S.; Kundu, S. Recent Trends and Perspectives in Electrochemical Water Splitting with an Emphasis on Sulfide, Selenide, and Phosphide Catalysts of Fe, Co, and Ni: A Review. ACS Catalysis. American Chemical Society December 2, 2016, pp 8069–8097. https://doi.org/10.1021/acscatal.6b02479.

(46) Wang, J.; Liao, T.; Wei, Z.; Sun, J.; Guo, J.; Sun, Z. Heteroatom-Doping of Non-Noble Metal-Based Catalysts for Electrocatalytic Hydrogen Evolution: An Electronic Structure Tuning Strategy. Small Methods. John Wiley and Sons Inc April 1, 2021. https://doi.org/10.1002/smtd.202000988.

(47) Kang, Q.; Li, M.; Shi, J.; Lu, Q.; Gao, F. A Universal Strategy for Carbon-Supported Transition Metal Phosphides as High-Performance Bifunctional Electrocatalysts towards Efficient Overall Water Splitting. ACS Appl Mater Interfaces 2020, 12 (17), 19447–19456. https://doi.org/10.1021/acsami.0c00795.

(48) Lu, F.; Zhou, M.; Zhou, Y.; Zeng, X. First-Row Transition Metal Based Catalysts for the Oxygen Evolution Reaction under Alkaline Conditions: Basic Principles and Recent Advances. Small. Wiley-VCH Verlag December 6, 2017. https://doi.org/10.1002/smll.201701931.

(49) Sarkar, A.; Velasco, L.; Wang, D.; Wang, Q.; Talasila, G.; de Biasi, L.; Kübel, C.; Brezesinski, T.; Bhattacharya, S. S.; Hahn, H.; Breitung, B. High Entropy Oxides for Reversible Energy Storage. Nat Commun 2018, 9 (1). https://doi.org/10.1038/s41467-018-05774-5.

(50) Haruna, A. B.; Onoh, E.; Ozoemena, K. I. Emerging High-Entropy Materials as Electrocatalysts for Rechargeable Zinc-Air Batteries. Curr Opin Electrochem 2023, 101264. https://doi.org/10.1016/j.coelec.2023.101264.

(51) Tomboc, G. M.; Zhang, X.; Choi, S.; Kim, D.; Lee, L. Y. S.; Lee, K. Stabilization, Characterization, and Electrochemical Applications of High-Entropy Oxides: Critical Assessment of Crystal Phase–Properties Relationship. Advanced Functional Materials. John Wiley and Sons Inc October 1, 2022. https://doi.org/10.1002/adfm.202205142.

(52) Dippo, O. F.; Vecchio, K. S. A Universal Configurational Entropy Metric for High-Entropy Materials. Scr Mater 2021, 201. https://doi.org/10.1016/j.scriptamat.2021.113974.

(53) Kaufman, J.; Esfarjani, K. Tunable Lattice Distortion in MgCoNiCuZnO5 Entropy-Stabilized Oxide. J Mater Res 2021, 36 (8), 1615–1623. https://doi.org/10.1557/s43578-021-00198-2.

(54) Rost, C. M.; Sachet, E.; Borman, T.; Moballegh, A.; Dickey, E. C.; Hou, D.; Jones, J. L.; Curtarolo, S.; Maria, J. P. Entropy-Stabilized Oxides. Nat Commun 2015, 6. https://doi.org/10.1038/ncomms9485.

(55) Mao, A.; Xiang, H. Z.; Zhang, Z. G.; Kuramoto, K.; Yu, H.; Ran, S. Solution Combustion Synthesis and Magnetic Property of Rock-Salt (Co 0.2 Cu 0.2 Mg 0.2 Ni 0.2 Zn 0.2)O High-Entropy Oxide Nanocrystalline Powder. J Magn Magn Mater 2019, 484, 245–252. https://doi.org/10.1016/j.jmmm.2019.04.023.

(56) Zhang, Y.; Ye, H. Y.; Zhang, W.; Xiong, R. G. Room-Temperature ABX3-Typed Molecular Ferroelectric: [C5H9-NH3][CdCl3]. Inorg Chem Front 2014, 1 (1), 118–123. https://doi.org/10.1039/c3qi00058c.

(57) Yang, Q.; Wang, G.; Wu, H.; Beshiwork, B. A.; Tian, D.; Zhu, S.; Yang, Y.; Lu, X.; Ding, Y.; Ling, Y.; Chen, Y.; Lin, B. A High-Entropy Perovskite Cathode for Solid Oxide Fuel Cells. J Alloys Compd 2021, 872. https://doi.org/10.1016/j.jallcom.2021.159633.

(58) Stygar, M.; Dąbrowa, J.; Moździerz, M.; Zajusz, M.; Skubida, W.; Mroczka, K.; Berent, K.; Świerczek, K.; Danielewski, M. Formation and Properties of High Entropy Oxides in Co-Cr-Fe-Mg-Mn-Ni-O System: Novel (Cr,Fe,Mg,Mn,Ni)3O4 and (Co,Cr,Fe,Mg,Mn)3O4 High Entropy Spinels. J Eur Ceram Soc 2020, 40 (4), 1644–1650. https://doi.org/10.1016/j.jeurceramsoc.2019.11.030.

(59) Dai, Y.; Yu, J.; Ni, M.; Shao, Z. Rational Design of Spinel Oxides as Bifunctional Oxygen Electrocatalysts for Rechargeable Zn-Air Batteries. Chemical Physics Reviews 2020, 1 (1). https://doi.org/10.1063/5.0017398.

(60) Zhao, Q.; Yan, Z.; Chen, C.; Chen, J. Spinels: Controlled Preparation, Oxygen Reduction/Evolution Reaction Application, and Beyond. Chemical Reviews. American Chemical Society August 9, 2017, pp 10121–10211. https://doi.org/10.1021/acs.chemrev.7b00051.

(61) Zhu, W.; Zhu, G.; Yao, C.; Chen, H.; Hu, J.; Zhu, Y.; Liang, W. Porous Amorphous FeCo Alloys as Pre-Catalysts for Promoting the Oxygen Evolution Reaction. J Alloys Compd 2020, 828, 154465. https://doi.org/10.1016/j.jallcom.2020.154465.

(62) Wang, Z.; Ang, J.; Zhang, B.; Zhang, Y.; Ma, X. Y. D.; Yan, T.; Liu, J.; Che, B.; Huang, Y.; Lu, X. FeCo/FeCoNi/N-Doped Carbon Nanotubes Grafted Polyhedron-

Derived Hybrid Fibers as Bifunctional Oxygen Electrocatalysts for Durable Rechargeable Zinc–Air Battery. Appl Catal B 2019, 254, 26–36. https://doi.org/10.1016/j.apcatb.2019.04.027.

(63) Huang, C.; Nie, J.; Xu, Z.; Zhang, X.; Tang, J.; Wang, B.; Huang, J.; Du, C.; Chen, J. One-Step Hydrothermal Synthesized 3D P–MoO3/FeCo LDH Heterostructure Electrocatalysts on Ni Foam for High-Efficiency Oxygen Evolution Electrocatalysis. Int J Hydrogen Energy 2021, 46 (24), 12992–13000. https://doi.org/10.1016/j.ijhydene.2021.01.145.

(64) Huang, C.; Nie, J.; Xu, Z.; Zhang, X.; Tang, J.; Wang, B.; Huang, J.; Du, C.; Chen, J. One-Step Hydrothermal Synthesized 3D P–MoO3/FeCo LDH Heterostructure Electrocatalysts on Ni Foam for High-Efficiency Oxygen Evolution Electrocatalysis. Int J Hydrogen Energy 2021, 46 (24), 12992–13000. https://doi.org/10.1016/j.ijhydene.2021.01.145.

(65) Liu, X.; Wang, L.; Yu, P.; Tian, C.; Sun, F.; Ma, J.; Li, W.; Fu, H. A Stable Bifunctional Catalyst for Rechargeable Zinc–Air Batteries: Iron–Cobalt Nanoparticles Embedded in a Nitrogen-Doped 3D Carbon Matrix. Angewandte Chemie 2018, 130 (49), 16398–16402. https://doi.org/10.1002/ange.201809009.

(66) Shi, Q.; Liu, Q.; Ma, Y.; Fang, Z.; Liang, Z.; Shao, G.; Tang, B.; Yang, W.; Qin, L.; Fang, X. High-Performance Trifunctional Electrocatalysts Based on FeCo/Co2P Hybrid Nanoparticles for Zinc–Air Battery and Self-Powered Overall Water Splitting. Adv Energy Mater 2020, 10 (10). https://doi.org/10.1002/aenm.201903854.

(67) Zeiger, M.; Jäckel, N.; Mochalin, V. N.; Presser, V. Review: Carbon Onions for Electrochemical Energy Storage. Journal of Materials Chemistry A. Royal Society of Chemistry 2016, pp 3172–3196. https://doi.org/10.1039/c5ta08295a.

(68) Wang, H.; Chen, Q.; Xiao, P.; Cao, L. Unlocking Zinc-Ion Energy Storage Performance of Onion-Like Carbon by Promoting Heteroatom Doping Strategy. ACS Appl Mater Interfaces 2022, 14 (7), 9013–9023. https://doi.org/10.1021/acsami.1c22016.

(69) Li, J.; Wang, N.; Deng, J.; Qian, W.; Chu, W. Flexible Metal-Templated Fabrication of Mesoporous Onion-like Carbon and Fe2O3@N-Doped Carbon Foam for Electrochemical Energy Storage. J Mater Chem A Mater 2018, 6 (27), 13012–13020. https://doi.org/10.1039/c8ta02417k.

(70) Portet, C.; Yushin, G.; Gogotsi, Y. Electrochemical Performance of Carbon Onions, Nanodiamonds, Carbon Black and Multiwalled Nanotubes in Electrical Double Layer Capacitors. Carbon N Y 2007, 45 (13), 2511–2518. https://doi.org/10.1016/j.carbon.2007.08.024.

(71) Samanta, A.; Raj, C. R. Bifunctional Nitrogen-Doped Hybrid Catalyst Based on Onion-like Carbon and Graphitic Carbon Encapsulated Transition Metal Alloy Nanostructure for Rechargeable Zinc-Air Battery. J Power Sources 2020, 455. https://doi.org/10.1016/j.jpowsour.2020.227975.

(72) Bokova-Sirosh, S. N.; Pershina, A. V.; Kuznetsov, V. L.; Ishchenko, A. V.; Moseenkov, S. I.; Orekhov, A. S.; Obraztsova, E. D. Raman Spectra for Characterization of Onion-like Carbon. In Journal of Nanoelectronics and Optoelectronics; 2013; Vol. 8, pp 106–109. https://doi.org/10.1166/jno.2013.1444.

(73) Deckenbach, D.; Schneider, J. J. A Long-Overlooked Pitfall in Rechargeable Zinc–Air Batteries: Proper Electrode Balancing. Adv Mater Interfaces 2023, 10 (15). https://doi.org/10.1002/admi.202202494.

(74) Chen, X.; Chen, D.; Li, G.; Sha, P.; Yu, J.; Yu, L.; Dong, L. FeNi Incorporated N Doped Carbon Nanotubes from Glucosamine Hydrochloride as Highly Efficient Bifunctional Catalyst for Long Term Rechargeable Zinc-Air Batteries. Electrochim Acta 2022, 428. https://doi.org/10.1016/j.electacta.2022.140938.

(75) Li, Y.; Xu, K.; Zhang, Q.; Zheng, Z.; Li, S.; Zhao, Q.; Li, C.; Dong, C.; Mei, Z.; Pan, F.; Dou, S. One-Pot Synthesis of FeNxC as Efficient Catalyst for High-Performance Zinc-Air Battery. Journal of Energy Chemistry 2022, 66, 100–106. https://doi.org/10.1016/j.jechem.2021.07.009.

(76) Li, W.; Chen, W.; Zhang, H.; Zhang, Z. Integratable Solid-State Zinc-Air Battery with Extended Cycle Life Inspired by Bionics. Chemical Engineering Journal 2022, 435. https://doi.org/10.1016/j.cej.2022.134900.

(77) Han, Y.; Duan, H.; Zhou, C.; Meng, H.; Jiang, Q.; Wang, B.; Yan, W.; Zhang, R. Stabilizing Cobalt Single Atoms via Flexible Carbon Membranes as Bifunctional Electrocatalysts for Binder-Free Zinc-Air Batteries. Nano Lett 2022, 22 (6), 2497–2505. https://doi.org/10.1021/acs.nanolett.2c00278.

(78) Hopkins, B. J.; Chervin, C. N.; Parker, J. F.; Long, J. W.; Rolison, D. R. An Areal-Energy Standard to Validate Air-Breathing Electrodes for Rechargeable Zinc–Air Batteries. Advanced Energy Materials. Wiley-VCH Verlag August 1, 2020. https://doi.org/10.1002/aenm.202001287.

(79) Jin, Z.; Lyu, J.; Zhao, Y. L.; Li, H.; Lin, X.; Xie, G.; Liu, X.; Kai, J. J.; Qiu, H. J. Rugged High-Entropy Alloy Nanowires with in Situ Formed Surface Spinel Oxide As Highly Stable Electrocatalyst in Zn-Air Batteries. ACS Mater Lett 2020, 2 (12), 1698–1706. https://doi.org/10.1021/acsmaterialslett.0c00434.

(80) Jin, Z.; Lyu, J.; Hu, K.; Chen, Z.; Xie, G.; Liu, X.; Lin, X.; Qiu, H. J. Eight-Component Nanoporous High-Entropy Oxides with Low Ru Contents as High-Performance Bifunctional Catalysts in Zn-Air Batteries. Small 2022, 18 (12). https://doi.org/10.1002/smll.202107207.

(81) Jin, Z.; Lyu, J.; Zhao, Y. L.; Li, H.; Chen, Z.; Lin, X.; Xie, G.; Liu, X.; Kai, J. J.; Qiu, H. J. Top-Down Synthesis of Noble Metal Particles on High-Entropy Oxide Supports for Electrocatalysis. Chemistry of Materials 2021, 33 (5), 1771–1780. https://doi.org/10.1021/acs.chemmater.0c04695.

(82) Yu, T.; Xu, H.; Jin, Z.; Zhang, Y.; Qiu, H. J. Noble Metal-Free High-Entropy Oxide/Co-N-C Bifunctional Electrocatalyst Enables Highly Reversible and Durable Zn-Air Batteries. Appl Surf Sci 2023, 610. https://doi.org/10.1016/j.apsusc.2022.155624.

(83) He, R.; Yang, L.; Zhang, Y.; Wang, X.; Lee, S.; Zhang, T.; Li, L.; Liang, Z.; Chen, J.; Li, J.; Ostovari Moghaddam, A.; Llorca, J.; Ibáñez, M.; Arbiol, J.; Xu, Y.; Cabot, A. A CrMnFeCoNi High Entropy Alloy Boosting Oxygen Evolution/Reduction Reactions and Zinc-Air Battery Performance. Energy Storage Mater 2023, 58, 287–298. https://doi.org/10.1016/j.ensm.2023.03.022.

(84) Cao, X.; Gao, Y.; Wang, Z.; Zeng, H.; Song, Y.; Tang, S.; Luo, L.; Gong, S. FeNiCrCoMn High-Entropy Alloy Nanoparticles Loaded on Carbon Nanotubes as Bifunctional Oxygen Catalysts for Rechargeable Zinc-Air Batteries. ACS Appl Mater Interfaces 2023. https://doi.org/10.1021/acsami.3c04120.

(85) Yu, T.; Zhang, Y.; Hu, Y.; Hu, K.; Lin, X.; Xie, G.; Liu, X.; Reddy, K. M.; Ito, Y.; Qiu, H. J. Twelve-Component Free-Standing Nanoporous High-Entropy Alloys for

Multifunctional Electrocatalysis. ACS Mater Lett 2022, 4 (1), 181–189. https://doi.org/10.1021/acsmaterialslett.1c00762.

(86) Yao, Y.; Li, Z.; Dou, Y.; Jiang, T.; Zou, J.; Lim, S. Y.; Norby, P.; Stamate, E.; Jensen, J. O.; Zhang, W. High Entropy Alloy Nanoparticles Encapsulated in Graphitised Hollow Carbon Tubes for Oxygen Reduction Electrocatalysis. Dalton Transactions 2023, 52 (13), 4142–4151. https://doi.org/10.1039/d2dt03637a.

(87) Zhang, Q.; Lian, K.; Liu, Q.; Qi, G.; Zhang, S.; Luo, J.; Liu, X. High Entropy Alloy Nanoparticles as Efficient Catalysts for Alkaline Overall Seawater Splitting and Zn-Air Batteries. J Colloid Interface Sci 2023, 646, 844–854. https://doi.org/10.1016/j.jcis.2023.05.074.

(88) Jin, Z.; Zhou, X.; Hu, Y.; Tang, X.; Hu, K.; Reddy, K. M.; Lin, X.; Qiu, H. J. A Fourteen-Component High-Entropy Alloy@oxide Bifunctional Electrocatalyst with a Record-Low ΔE of 0.61 V for Highly Reversible Zn-Air Batteries. Chem Sci 2022, 13 (41), 12056–12064. https://doi.org/10.1039/d2sc04461g.

(89) Lin, X.; Hu, Y.; Hu, K.; Lin, X.; Xie, G.; Liu, X.; Reddy, K. M.; Qiu, H. J. Inhibited Surface Diffusion of High-Entropy Nano-Alloys for the Preparation of 3D Nanoporous Graphene with High Amounts of Single Atom Dopants. ACS Mater Lett 2022, 4 (5), 978–986. https://doi.org/10.1021/acsmaterialslett.2c00245.

(90) Fang, G.; Gao, J.; Lv, J.; Jia, H.; Li, H.; Liu, W.; Xie, G.; Chen, Z.; Huang, Y.; Yuan, Q.; Liu, X.; Lin, X.; Sun, S.; Qiu, H. J. Multi-Component Nanoporous Alloy/(Oxy)Hydroxide for Bifunctional Oxygen Electrocatalysis and Rechargeable Zn-Air Batteries. Appl Catal B 2020, 268. https://doi.org/10.1016/j.apcatb.2019.118431.

(91) Gao, L.; Zhong, X.; Li, Z.; Hu, J.; Cui, S.; Wang, X.; Xu, B. Multi-Layer Reduced Graphene Oxide Encapsulates High-Entropy Alloy for Rechargeable Zinc-Air Batteries. Chemical Communications 2024. https://doi.org/10.1039/d3cc05069f.

(92) Arafat, Y.; Zhong, Y.; Azhar, M. R.; Asif, M.; Tadé, M. O.; Shao, Z. CoNiFe-Layered Double Hydroxide Decorated Co-N-C Network as a Robust Bi-Functional Oxygen Electrocatalyst for Zinc-Air Batteries. EcoMat 2023. https://doi.org/10.1002/eom2.12394.

(93) Henkelman, G.; Wei, L.; Chen, Y.; Liu, C.; Liu, F.; Li, H.; Chen, J.; Fei, J.; Yu, Z.; Yuan, Z.; Wang, C.; Zheng, H.; Liu, Z.; Xu, M. One-Dimensional van Der Waals Heterostructures as Efficient Metal-Free Oxygen Electrocatalysts. ACS Nano 2021, 15 (2), 3309–3319. https://doi.org/10.1021/acsnano.0c10242.

(94) Liu, Q.; Wang, Y.; Dai, L.; Yao, J. Scalable Fabrication of Nanoporous Carbon Fiber Films as Bifunctional Catalytic Electrodes for Flexible Zn-Air Batteries. Advanced Materials 2016, 28 (15), 3000–3006. https://doi.org/10.1002/adma.201506112.

(95) Liu, X.; Park, M.; Kim, M. G.; Gupta, S.; Wu, G.; Cho, J. Integrating NiCo Alloys with Their Oxides as Efficient Bifunctional Cathode Catalysts for Rechargeable Zinc–Air Batteries. Angewandte Chemie 2015, 127 (33), 9790–9794. https://doi.org/10.1002/ange.201503612.

(96) Dang, L.; Zhang, K.; Wang, Q.; Xu, C.; Wang, S. Fe-Alloyed MoNi Nanohybrids as Oxygen Evolution Reaction/Oxygen Reduction Reaction Bifunctional Electrocatalyst for Rechargeable Zinc–Air Batteries. Physica Status Solidi (A) Applications and Materials Science 2023, 220 (2). https://doi.org/10.1002/pssa.202200581.

(97) Wang, Z.; Ang, J.; Zhang, B.; Zhang, Y.; Ma, X. Y. D.; Yan, T.; Liu, J.; Che, B.; Huang, Y.; Lu, X. FeCo/FeCoNi/N-Doped Carbon Nanotubes Grafted Polyhedron-

Derived Hybrid Fibers as Bifunctional Oxygen Electrocatalysts for Durable Rechargeable Zinc–Air Battery. Appl Catal B 2019, 254, 26–36. https://doi.org/10.1016/j.apcatb.2019.04.027.

(98) Chang, S.; Zhang, H.; Zhang, Z. FeCo Alloy/N, S Dual-Doped Carbon Composite as a High-Performance Bifunctional Catalyst in an Advanced Rechargeable Zinc-Air Battery. Journal of Energy Chemistry 2021, 56, 64–71. https://doi.org/10.1016/j.jechem.2020.07.047.

(99) Zhong, J.; Zhu, Z.; Xu, Q.; Peng, L.; Luo, K.; Yuan, D. FeCo Alloy Nanoparticles Supported on Co-N-C Cubes Derived from Imidazolate Frameworks as a Bifunctional Electrocatalyst for Rechargeable Zinc-Air Batteries. Energy and Fuels 2023. https://doi.org/10.1021/acs.energyfuels.3c02221.

(100) Su, C. Y.; Cheng, H.; Li, W.; Liu, Z. Q.; Li, N.; Hou, Z.; Bai, F. Q.; Zhang, H. X.; Ma, T. Y. Atomic Modulation of FeCo–Nitrogen–Carbon Bifunctional Oxygen Electrodes for Rechargeable and Flexible All-Solid-State Zinc–Air Battery. Adv Energy Mater 2017, 7 (13). https://doi.org/10.1002/aenm.201602420.

(101) Hao, X.; Jiang, Z.; Zhang, B.; Tian, X.; Song, C.; Wang, L.; Maiyalagan, T.; Hao, X.; Jiang, Z. J. N-Doped Carbon Nanotubes Derived from Graphene Oxide with Embedment of FeCo Nanoparticles as Bifunctional Air Electrode for Rechargeable Liquid and Flexible All-Solid-State Zinc–Air Batteries. Advanced Science 2021, 8 (10). https://doi.org/10.1002/advs.202004572.

(102) Wang, Y.; Qiao, M.; Mamat, X. An Advantage Combined Strategy for Preparing Bi-Functional Electrocatalyst in Rechargeable Zinc-Air Batteries. Chemical Engineering Journal 2020, 402. https://doi.org/10.1016/j.cej.2020.126214.

(103) Xiong, Y.; Jiang, Z.; Gong, L.; Tian, X.; Song, C.; Maiyalagan, T.; Jiang, Z. J. Construction of Co/FeCo@Fe(Co)3O4 Heterojunction Rich in Oxygen Vacancies Derived from Metal–Organic Frameworks Using O2 Plasma as a High-Performance Bifunctional Catalyst for Rechargeable Zinc-Air Batteries. J Colloid Interface Sci 2023, 649, 36–48. https://doi.org/10.1016/j.jcis.2023.06.040.

(104) Wen, J.; Li, X.; Liu, Y.; Yang, M.; Liu, B.; Chen, H.; Li, H. Facile Crafting of Ultralong N-Doped Carbon Nanotube Encapsulated with FeCo Nanoparticles as Bifunctional Electrocatalyst for Rechargeable Zinc-Air Batteries. Microporous and Mesoporous Materials 2022, 336. https://doi.org/10.1016/j.micromeso.2022.111850.

(105) Fan, M.; Liu, P.; Cheng, Y.; Tang, H.; Jin, B.; Zhang, H. Fe-N4/Co-N4 Active Sites Engineered Porous Carbon with Encapsulated FeCo Alloy as an Efficient Bifunctional Catalyst for Rechargeable Zinc-Air Battery. J Alloys Compd 2023, 935. https://doi.org/10.1016/j.jallcom.2022.168107.

(106) Yang, P. Q.; Ko, T. E.; Tseng, C. M.; Wang, W. H.; Huang, C. C.; Tsai, J. E.; Fu, Y. C.; Li, Y. Y. FeOOH-Carbon Nanotube-FeCo/Nitrogen-Doped Porous Carbon as an Excellent Bifunctional Catalyst for Achieving High Power Performance in Rechargeable Zinc-Air Batteries. Journal of Industrial and Engineering Chemistry 2023, 121, 338–347. https://doi.org/10.1016/j.jiec.2023.01.037.

(107) Li, C.; Wu, M.; Liu, R. High-Performance Bifunctional Oxygen Electrocatalysts for Zinc-Air Batteries over Mesoporous Fe/Co-N-C Nanofibers with Embedding FeCo Alloy Nanoparticles. Appl Catal B 2019, 244, 150–158. https://doi.org/10.1016/j.apcatb.2018.11.039.

(108) Song, L.; Zhang, J.; Sarkar, S.; Zhao, C.; Wang, Z.; Huang, C.; Yan, L.; Zhao, Y. Interface Engineering of FeCo-Co Structure as Bifunctional Oxygen Electrocatalyst

for Rechargeable Zinc-Air Batteries via Alloying Degree Control Strategy. Chemical Engineering Journal 2022, 433. https://doi.org/10.1016/j.cej.2021.133686.

(109) Song, L.; Zhang, J.; Sarkar, S.; Zhao, C.; Wang, Z.; Huang, C.; Yan, L.; Zhao, Y. Interface Engineering of FeCo-Co Structure as Bifunctional Oxygen Electrocatalyst for Rechargeable Zinc-Air Batteries via Alloying Degree Control Strategy. Chemical Engineering Journal 2022, 433. https://doi.org/10.1016/j.cej.2021.133686.

(110) Zhao, C. X.; Liu, J. N.; Wang, J.; Ren, D.; Yu, J.; Chen, X.; Li, B. Q.; Zhang, Q. A ΔE = 0.63 V Bifunctional Oxygen Electrocatalyst Enables High-Rate and Long-Cycling Zinc–Air Batteries. Advanced Materials 2021, 33 (15). https://doi.org/10.1002/adma.202008606.

(111) Zhang, J.; Zhao, Z.; Xia, Z.; Dai, L. A Metal-Free Bifunctional Electrocatalyst for Oxygen Reduction and Oxygen Evolution Reactions. Nat Nanotechnol 2015, 10 (5), 444–452. https://doi.org/10.1038/nnano.2015.48.

(112) Fu, G.; Cui, Z.; Chen, Y.; Xu, L.; Tang, Y.; Goodenough, J. B. Hierarchically Mesoporous Nickel-Iron Nitride as a Cost-Efficient and Highly Durable Electrocatalyst for Zn-Air Battery. Nano Energy 2017, 39, 77–85. https://doi.org/10.1016/j.nanoen.2017.06.029.

(113) Ramakrishnan, S.; Balamurugan, J.; Vinothkannan, M.; Kim, A. R.; Sengodan, S.; Yoo, D. J. Nitrogen-Doped Graphene Encapsulated FeCoMoS Nanoparticles as Advanced Trifunctional Catalyst for Water Splitting Devices and Zinc–Air Batteries. Appl Catal B 2020, 279. https://doi.org/10.1016/j.apcatb.2020.119381.

(114) Wang, Q.; Xue, Y.; Sun, S.; Yan, S.; Miao, H.; Liu, Z. Facile Synthesis of Ternary Spinel Co–Mn–Ni Nanorods as Efficient Bi-Functional Oxygen Catalysts for

Rechargeable Zinc-Air Batteries. J Power Sources 2019, 435. https://doi.org/10.1016/j.jpowsour.2019.226761.

(115) Li, C.; Zhang, Z.; Wu, M.; Liu, R. FeCoNi Ternary Alloy Embedded Mesoporous Carbon Nanofiber: An Efficient Oxygen Evolution Catalyst for Rechargeable Zinc-Air Battery. Mater Lett 2019, 238, 138–142. https://doi.org/10.1016/j.matlet.2018.11.160.

(116) Tang, W.; He, J.; Teng, K.; Gao, L.; Qi, R.; Deng, Y.; Liu, R.; Li, A.; Fu, H.; Wang, C. A. Toward Highly Efficient Bifunctional Electrocatalysts for Zinc-Air Batteries: From Theoretical Prediction to a Ternary FeCoNi Design. Nanoscale 2022, 14 (46), 17447–17459. https://doi.org/10.1039/d2nr04741a.

(117) Lu, Y. T.; Chien, Y. J.; Liu, C. F.; You, T. H.; Hu, C. C. Active Site-Engineered Bifunctional Electrocatalysts of Ternary Spinel Oxides, M0.1Ni0.9Co2O4 (M: Mn, Fe, Cu, Zn) for the Air Electrode of Rechargeable Zinc-Air Batteries. J Mater Chem A Mater 2017, 5 (39), 21016–21026. https://doi.org/10.1039/c7ta06302d.

(118) Liu, K.; Huang, H.; Zhu, Y.; Wang, S.; Lyu, Z.; Han, X.; Kuang, Q.; Xie, S. Edge-Segregated Ternary Pd-Pt-Ni Spiral Nanosheets as High-Performance Bifunctional Oxygen Redox Electrocatalysts for Rechargeable Zinc-Air Batteries. J Mater Chem A Mater 2022, 10 (7), 3808–3817. https://doi.org/10.1039/d1ta10585j.

(119) Wang, X.; Zhang, J.; Ma, D.; Feng, X.; Wang, L.; Wang, B. Metal-Organic Framework-Derived Trimetallic Nanocomposites as Efficient Bifunctional Oxygen Catalysts for Zinc-Air Batteries. ACS Appl Mater Interfaces 2021, 13 (28), 33209–33217. https://doi.org/10.1021/acsami.1c02570.

(120) Rui, C.; Zhang, T.; Jiang, Y.; Xie, D.; Li, M.; Lu, Q.; Bu, Y. Highly Efficient and Stable Bifunctional Electrocatalyst with Alloy/Oxide Heterostructures for a

Rechargeable Zinc-Air Battery. Energy and Fuels 2022, 36 (20), 12816–12825. https://doi.org/10.1021/acs.energyfuels.2c02744.

(121) Liu, J.; Luo, Z.; Zhang, X.; Zheng, H.; Peng, L.; Qian, D.; Jia, C.; Sun-Waterhouse, D.; Waterhouse, G. I. N. FeCoNi Nanoalloys Embedded in Hierarchical N-Rich Carbon Matrix with Enhanced Oxygen Electrocatalysis for Rechargeable Zn-Air Batteries. J Mater Chem A Mater 2021, 9 (48), 27701–27708. https://doi.org/10.1039/d1ta09964g.

(122) Wu, Z.; Hu, X.; Cai, C.; Wang, Y.; Li, X.; Wen, J.; Li, B.; Gong, H. Controlled Three-Dimensional Leaf-like NiCoO2@NiCo Layered Double Hydroxide Heterostructures for Oxygen Evolution Electrocatalysts in Rechargeable Zn–Air Batteries. J Colloid Interface Sci 2023. https://doi.org/10.1016/j.jcis.2023.11.157.

(123) Wang, T.; Zhang, Q.; Lian, K.; Qi, G.; Liu, Q.; Feng, L.; Hu, G.; Luo, J.; Liu, X. Fe Nanoparticles Confined by Multiple-Heteroatom-Doped Carbon Frameworks for Aqueous Zn-Air Battery Driving CO2 Electrolysis. J Colloid Interface Sci 2024, 655, 176–186. https://doi.org/10.1016/j.jcis.2023.10.157.

(124) Wei, J.; Lou, J.; Hu, W.; Song, X.; Wang, H.; Yang, Y.; Zhang, Y.; Jiang, Z.; Mei, B.; Wang, L.; Yang, T.; Wang, Q.; Li, X. Superstructured Carbon with Enhanced Kinetics for Zinc-Air Battery and Self-Powered Overall Water Splitting. Small 2024. https://doi.org/10.1002/smll.202308956.

(125) Liu, J.; Chen, W.; Yuan, S.; Liu, T.; Wang, Q. High-Coordination Fe-N4SP Single-Atom Catalysts via the Multi-Shell Synergistic Effect for the Enhanced Oxygen Reduction Reaction of Rechargeable Zn-Air Battery Cathodes. Energy Environ Sci 2023. https://doi.org/10.1039/d3ee03183g.

(126) Zhai, W.; He, Y.; Duan, Y. e.; Guo, S.; Chen, Y.; Dai, Z.; Liu, L.; Tan, Q. Densely Populated Trimetallic Single-Atoms for Durable Low-Temperature Flexible Zinc-Air Batteries. Appl Catal B 2024, 342. https://doi.org/10.1016/j.apcatb.2023.123438.

(127) Lu, X.; Li, Y.; Dong, D.; Wan, Y.; Li, R.; Xiao, L.; Wang, D.; Liu, L.; Wang, G.; Zhang, J.; An, M.; Yang, P. Coexisting Fe Single Atoms and Nanoparticles on Hierarchically Porous Carbon for High-Efficiency Oxygen Reduction Reaction and Zn-Air Batteries. J Colloid Interface Sci 2024, 653, 654–663. https://doi.org/10.1016/j.jcis.2023.09.047.

(128) Chen, S.; Xu, J.; Chen, J.; Yao, Y.; Wang, Z.; Li, P.; Li, Y.; Wang, F. Ru Doping Induced Interface Engineering in Flower-Liked CoMoO4-RuO2 Boosts Oxygen Electrocatalysis for Rechargeable Zn-Air Battery. J Colloid Interface Sci 2024, 658, 230–237. https://doi.org/10.1016/j.jcis.2023.12.066.

(129) Niu, Y.; Jiang, G.; Gong, S.; Liu, X.; Shangguan, E.; Li, L.; Chen, Z. Engineering of Heterointerface of Ultrathin Carbon Nanosheet-Supported CoN/MnO Enhances Oxygen Electrocatalysis for Rechargeable Zn–Air Batteries. J Colloid Interface Sci 2024, 656, 346–357. https://doi.org/10.1016/j.jcis.2023.11.112.

(130) Liu, X.; Wang, Z.; Wang, J.; Tang, T.; Li, C.; Yu, J.; Zhang, S.; Deng, C. Unsaturated Cobalt-Nitrogen Atomic Sites in Necklace-like Hairy Fibers towards Highly Efficient Oxygen Electrocatalysis for Flexible Zn-Air Battery. Energy Storage Mater 2024, 103184. https://doi.org/10.1016/j.ensm.2024.103184.

(131) Wang, L.; Hu, X.; Li, H.; Huang, Z.; Huang, J.; Isimjan, T. T.; Yang, X. Engineering Built-in Electric Fields in Oxygen-Deficient MnO-CeO 2 @Cs Catalysts: Enhanced Performance and Kinetics for the Oxygen Reduction Reaction in Aqueous/Flexible Zinc–Air Batteries. Green Chemistry 2024. https://doi.org/10.1039/D3GC04537D.

(132) Lian, Y.; Yu, T.; Qu, Y.; Yuan, C.; Lu, Z.-H.; Guo, M. Interface Electronic Modulation of Monodispersed Co Metal-Co 7 Fe 3 Alloy Heterostructures for Rechargeable Zn–Air Battery. Ind Eng Chem Res 2024. https://doi.org/10.1021/acs.iecr.3c03149.

(133) Zheng, J.; Hu, G.; Liu, B.; Liu, Y.; Li, H.; Zhao, H.; Yang, M. In-Situ Spatial-Embedding Construction of FeCo Nucleus-Bound Carbon Skeletons for Durable Rechargeable Liquid and Flexible Zn-Air Batteries. Energy Storage Mater 2024, 65. https://doi.org/10.1016/j.ensm.2023.103106.

(134) Wang, B.; Liu, Q.; Yuan, A.; Shi, Q.; Jiang, L.; Yang, W.; Yang, T.; Hou, X. A Facile and Green Strategy for Mass Production of Dispersive FeCo-Rich Phosphides@N,P-Doped Carbon Electrocatalysts toward Efficient and Stable Rechargeable Zn-Air Battery and Water Splitting. J Mater Sci Technol 2024, 182, 1–11. https://doi.org/10.1016/j.jmst.2023.08.073.

(135) Anand, P.; Wong, M. S.; Fu, Y. P. Lanthanum Strontium Cobaltite-Based Perovskite as an Electrocatalyst for Zinc-Air Battery Application. J Energy Storage 2024, 77. https://doi.org/10.1016/j.est.2023.109917.

(136) Muthurasu, A.; Pathak, I.; Acharya, D.; Rosyara, Y. R.; Kim, H. Y. Cutting-Edge Nitrogen, Boron, and Fluorine Triply Doped Chain-like Porous Carbon Nanofibers: A Versatile Solution for High-Performance Zinc-Air Batteries and Self-Powered Water Splitting. J Mater Chem A Mater 2023. https://doi.org/10.1039/d3ta06387a.

(137) Zhang, W.; Pu, W.; Zhang, X.; Xiao, Y.; Liu, Y. Preparation of Co N Co-Doped Carbon Nanosheets Electrocatalyst for Efficient Oxygen Reduction Reaction in Zinc-Air Battery. Diam Relat Mater 2024, 142, 110810. https://doi.org/10.1016/j.diamond.2024.110810.

(138) Li, J.; Qin, Y.; Bai, Z.; Li, S.; Li, L.; Ouyang, B.; Kan, E.; Zhang, W. Investigating the Role of 3D Hierarchical Ni-CAT/NiFe-LDH/CNFs in Enhancing the Oxygen Evolution Reaction and Zn-Air Battery Performance. Appl Surf Sci 2024, 648. https://doi.org/10.1016/j.apsusc.2023.159080.

(139) Huang, H.; Liang, Q.; Guo, H.; Wang, Z.; Yan, G.; Wu, F.; Wang, J. Spray Pyrolysis Regulated FeCo Alloy Anchoring on Nitrogen–Doped Carbon Hollow Spheres Boost the Performance of Zinc–Air Batteries. Small 2024. https://doi.org/10.1002/smll.202310318.

(140) Deng, D.; Zhang, H.; Wu, J.; Tang, X.; Ling, M.; Dong, S.; Xu, L.; Li, H.; Li, H. Electronic Structure and Spin State Regulation of Vanadium Nitride via a Sulfur Doping Strategy toward Flexible Zinc-Air Batteries. Journal of Energy Chemistry 2024, 89, 239–249. https://doi.org/10.1016/j.jechem.2023.10.024.

(141) Ayyaluri, R. R.; Krishna, B. N. V.; Ankinapalli, O. R.; Yu, J. S. Facile Hydrothermal Synthesis of NiMoO4·xH2O Nanorods-like Structures as Bifunctional Oxygen Electrocatalysts for Rechargeable Zinc-Air Batteries. J Energy Storage 2024, 78, 110171. https://doi.org/10.1016/j.est.2023.110171.

(142) Sumboja, A.; Ge, X.; Goh, F. W. T.; Li, B.; Geng, D.; Hor, T. S. A.; Zong, Y.; Liu, Z. Manganese Oxide Catalyst Grown on Carbon Paper as an Air Cathode for High-Performance Rechargeable Zinc-Air Batteries. Chempluschem 2015, 80 (8), 1341–1346. https://doi.org/10.1002/cplu.201500183.

(143) Wei, L.; Karahan, H. E.; Zhai, S.; Liu, H.; Chen, X.; Zhou, Z.; Lei, Y.; Liu, Z.; Chen, Y. Amorphous Bimetallic Oxide–Graphene Hybrids as Bifunctional Oxygen Electrocatalysts for Rechargeable Zn–Air Batteries. Advanced Materials 2017, 29 (38). https://doi.org/10.1002/adma.201701410.

(144) Ge, X.; Liu, Y.; Goh, F. W. T.; Hor, T. S. A.; Zong, Y.; Xiao, P.; Zhang, Z.; Lim, S. H.; Li, B.; Wang, X.; Liu, Z. Dual-Phase Spinel MnCo2O4 and Spinel MnCo 2O4/Nanocarbon Hybrids for Electrocatalytic Oxygen Reduction and Evolution. ACS Appl Mater Interfaces 2014, 6 (15), 12684–12691. https://doi.org/10.1021/am502675c.

(145) Li, B.; Ge, X.; Goh, F. W. T.; Hor, T. S. A.; Geng, D.; Du, G.; Liu, Z.; Zhang, J.; Liu, X.; Zong, Y. Co3O4 Nanoparticles Decorated Carbon Nanofiber Mat as Binder-Free Air-Cathode for High Performance Rechargeable Zinc-Air Batteries. Nanoscale 2015, 7 (5), 1830–1838. https://doi.org/10.1039/c4nr05988c.

(146) Amiinu, I. S.; Liu, X.; Pu, Z.; Li, W.; Li, Q.; Zhang, J.; Tang, H.; Zhang, H.; Mu, S. From 3D ZIF Nanocrystals to Co–Nx/C Nanorod Array Electrocatalysts for ORR, OER, and Zn–Air Batteries. Adv Funct Mater 2018, 28 (5). https://doi.org/10.1002/adfm.201704638.

(147) Nam, G.; Son, Y.; Park, S. O.; Jeon, W. C.; Jang, H.; Park, J.; Chae, S.; Yoo, Y.; Ryu, J.; Kim, M. G.; Kwak, S. K.; Cho, J. A Ternary Ni46Co40Fe14 Nanoalloy-Based Oxygen Electrocatalyst for Highly Efficient Rechargeable Zinc–Air Batteries. Advanced Materials 2018, 30 (46). https://doi.org/10.1002/adma.201803372.

(148) Bontempelli, G.; Dossi, N.; Toniolo, R. Polarography/Voltammetry. In Reference Module in Chemistry, Molecular Sciences and Chemical Engineering; Elsevier, 2018. https://doi.org/10.1016/B978-0-12-409547-2.14326-4.

(149) Azam, M. A.; Mupit, M. Carbon Nanomaterial-Based Sensor: Synthesis and Characterization. In Carbon Nanomaterials-Based Sensors; Elsevier, 2022; pp 15–28. https://doi.org/10.1016/B978-0-323-91174-0.00015-9.

(150) Le, X. T.; Viel, P.; Tran, D. P.; Grisotto, F.; Palacin, S. Surface Homogeneity of Anion Exchange Membranes: A Chronopotentiometric Study in the Overlimiting Current

Range. Journal of Physical Chemistry B 2009, 113 (17), 5829–5836. https://doi.org/10.1021/jp900138v.

(151) Electrochemistry of Insertion Materials for Hydrogen and Lithium. http://www.springer.com/series/7386.

CHAPTER 3

Characterization and electrochemical techniques

A brief overview of some of the characterization techniques is presented in this chapter, along with electrochemical measurement techniques and RZAB fabrication.

3.1. Characterization techniques

3.1.1. X-ray diffraction

X-ray diffraction is a technique used to investigate the crystallinity of materials. The components (ions, atoms, or molecules) in the crystalline material are arranged regularly so that X-rays are scattered by a periodic array of particles with long-range order. There are either constructive or destructive interferences between the scattered X-rays from the sample however detectors can only detect the signals where constructive interference occurs as shown in **Figure 3.1**. As the incident X-ray beam passes through the material, it scatters in different directions travelling to different optical path lengths. X-ray beam incident angle and crystal plane distance affect this path length, and this is summarized by Bragg's equation:

$$n\lambda = 2dsin\theta$$

Where n is an integer, indicating the order of the diffraction peak (i.e., n=1 for the first peak, n=2 for the second peak, etc.), λ is the wavelength of the X-rays, d is the spacing between the crystal planes and θ is the angle between the incident X-rays and the crystal planes. Bragg's equation allows for the distance between the lattice planes of the materials to be calculated by measuring the angle θ and knowing the wavelength λ of the X-rays used. This technique is used for bulk sample analysis.

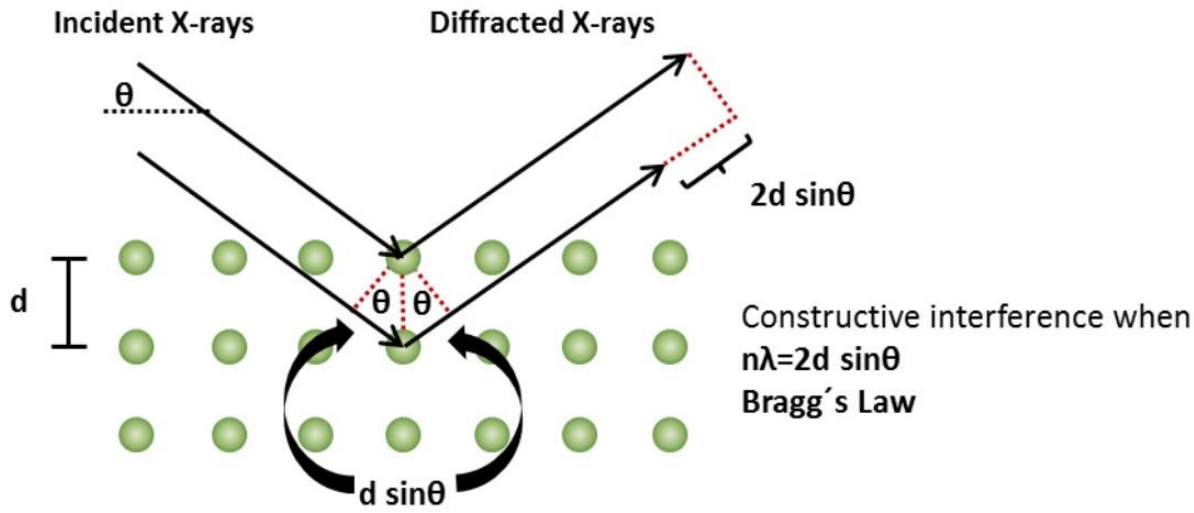

Figure 3. 1: Bragg's equation schematic representation.

3.1.2. XPS

X-ray photoelectron spectroscopy (XPS) is a sensitive quantitative spectroscopic technique used to measure the chemical states of almost all elements (except Hydrogen and Helium) and the surface composition of materials. The technique is unique and helps in understanding the surface chemistry of materials. Materials exposed to monochromatic X-rays emit photoelectrons from surface atoms with energies corresponding to each element present in the sample. The electrons from the top 100 Å get emitted and have enough energy to reach the detector resulting in an XPS spectra. **Figure 3.2** shows the simplified diagram of the XPS. The electron binding energy (BE) can be determined by measuring the kinetic energy (KE) of emitted electrons since the energy of the X-ray with a certain wavelength is fixed. The binding energy is determined as follows:

$$BE = h\upsilon - KE - \varphi$$

Where φ is the work function of the spectrometer. Atoms have specific orbital levels and therefore specific binding energies for removing electrons from each level. Additionally, the amount of energy shift (chemical shift) at the photoelectron peak position can be used to

determine if an element exists as a compound (and what kind) since the bonding energy of elements varies slightly depending on their bonding state and chemical environment.

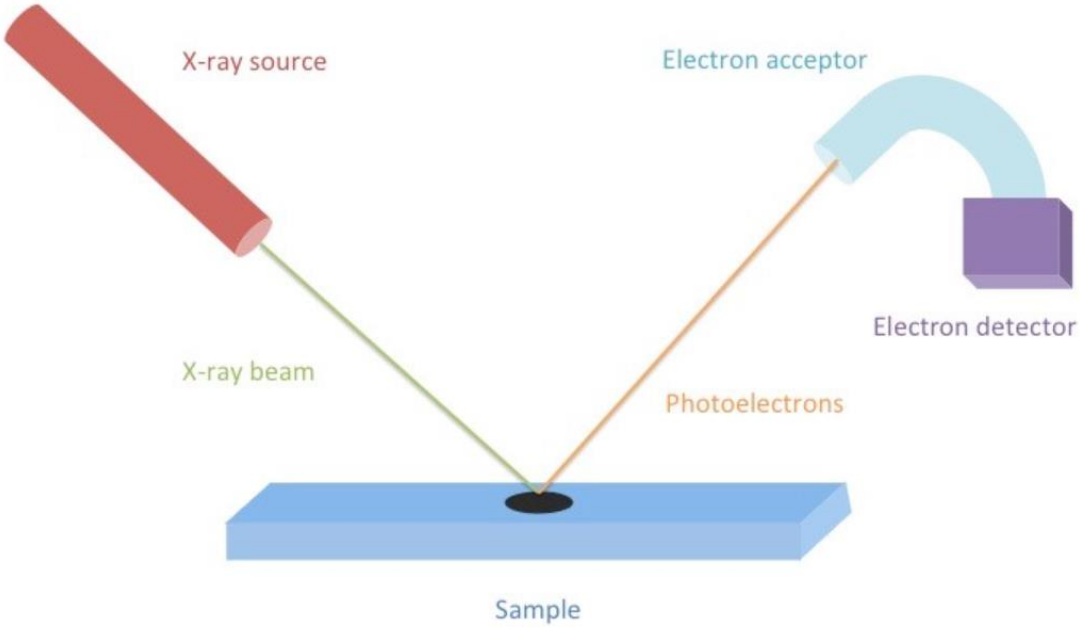

Figure 3. 2: XPS simplified diagram.

3.1.3. Transmission electron microscopy

Transmission electron microscopy is an analytical technique used in analysing the internal structure of solids using a high-energy electron beam which transmits through the solid sample. After an electron flux passes through a thin sample of the specimen under study, a photographic image is captured. The TEM resolution is obtained from the wavelength of electron reflux (λ), spherical aberration and angle of convergence (α) [1]. It is theoretically determined as follows:

$$r = 0.61\frac{\lambda}{\alpha}$$

It is impossible to obtain the theoretical resolution due to lens aberrations therefore the electron flux wavelength is inversely proportional to electron voltage [1]. The different parts of TEM are shown in **Figure 3.3**. Fluorescent screens, photographic film, and CCD cameras are among

the imaging devices that can be used [2]. The specimen is prepared by embedding the material and cutting it into ultrathin sections so that the electron beam can penetrate the sample.

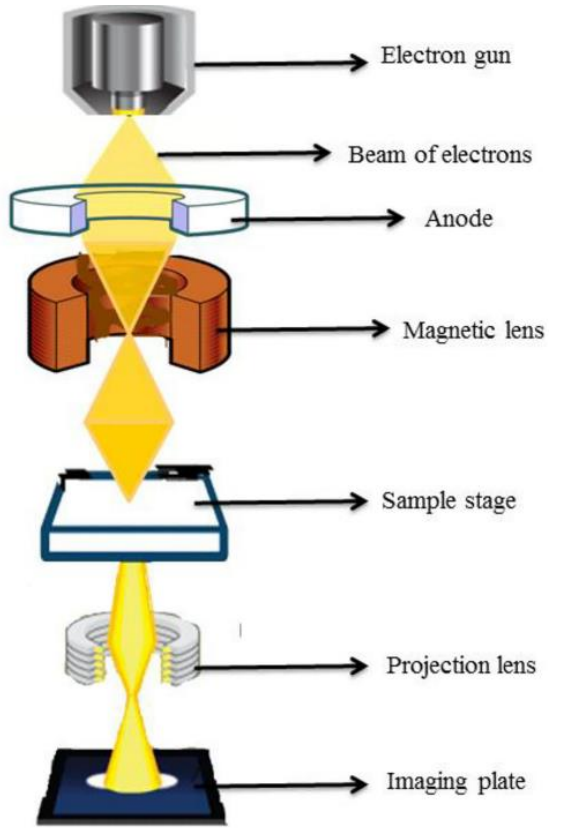

Figure 3. 3: Transmission electron microscopy (TEM) (adapted from [2]).

3.1.4. Raman spectroscopy

This technique measures the scattered intensity of molecular vibrations giving the Raman shift spectrum. Vibrational transitions in the molecule's ground state are the basis for this theory. Raman is a light scattering technique which involves the shift of an excited incident beam of radiation resulting from inelastic interactions between the photon and the sample molecules. A molecule's vibration changes the polarizability or shape of its electron distribution, resulting in Raman scattering [3]. Raman spectroscopy measures the change in polarizability of molecular bonds more intensely for pi bonds of symmetric molecules (e.g. aromatic and olefinic C=C) than for sigma bonds of atoms with different electronegativity (e.g. C-O, C-N and O-H). The

technique is non-destructive and provides information about crystallinity, chemical structure, molecular interactions, phase, and polymorphs.

3.2. Electrochemical measurements

The electrochemical characterizations were carried out to determine the ORR and OER kinetics. The Biologic SP300/VSP300 powered by EC lab was used for the three-electrode electrochemical measurements. The glassy carbon electrode was used as the working electrode (WE), the silver-silver chloride (Ag/AgCl) soaked in 3 M KCl was used as the reference electrode (RE) and the Pt wire was used as the counter electrode (CE). The three-electrode set-up is depicted in **Figure 3.4**. To saturate the electrolyte with O_2, the oxygen gas was passed through the gas inlet and bubbled into the electrolyte. The glassy carbon electrode was modified with electrocatalysts of choice before testing for ORR and OER.

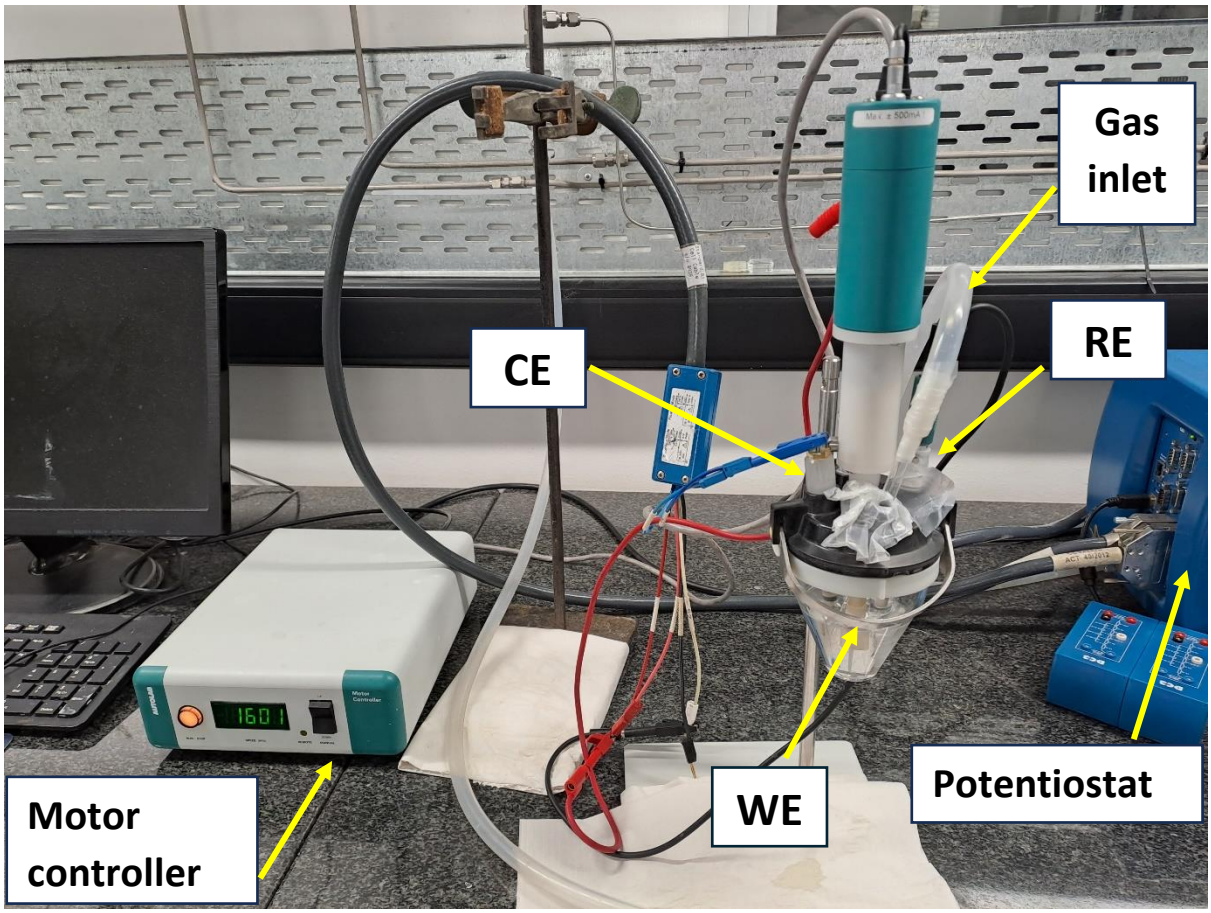

Figure 3. 4: The three-electrode system used for RDE experiments.

3.3. Rechargeable zinc-air battery fabrication

A home-made cell was fabricated to measure the performance of the catalysts in rechargeable zinc-air batteries. A zinc plate with a thickness of 0.25 mm was used as the anode and the gas diffusion layer (carbon paper) coated with the catalyst as the air cathode. The carbon paper with a geometric area of 1 cm^2 was used and 10 mg of the catalyst was loaded on the paper. **Figure 3.5** shows pictures of the fabricated anode and cathode. For the electrolyte, 0.2 M zinc acetate was dissolved in 6 M KOH to form zincate ($Zn(OH)_4^{2-}$) and ensure reversible zinc electrochemical reactions at the anode [4]. To prepare the catalyst slurry, 10 mg of the powder was dissolved in 20 µL of water, 180 µL of isopropanol and 20 µL of PTFE and stirred on a magnetic stirrer. The coated catalyst was oven-dried at 80 ℃ for 30 min. A rechargeable zinc-air battery with a mixture of Pt/C and IrO_2 (mass ratio of 1:1) as the catalyst was assembled in the same way for comparison.

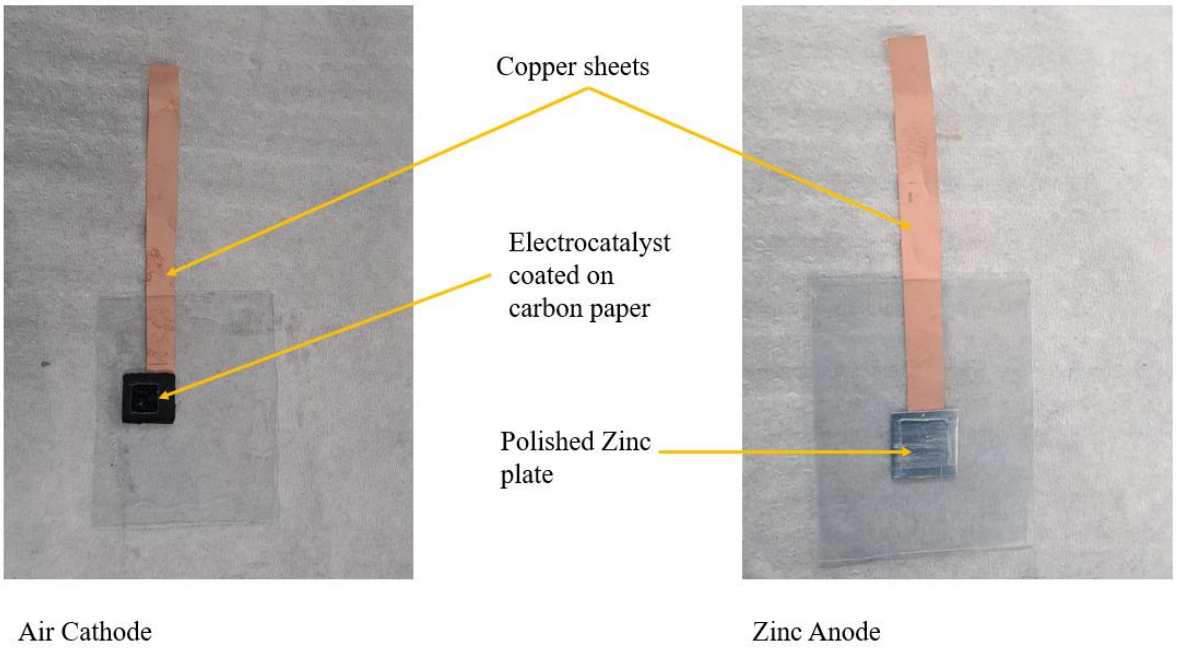

Figure 3. 5: Left: the air cathode with the electrocatalyst coated on the gas diffusion layer. Right: The zinc anode with the polished zinc plate.

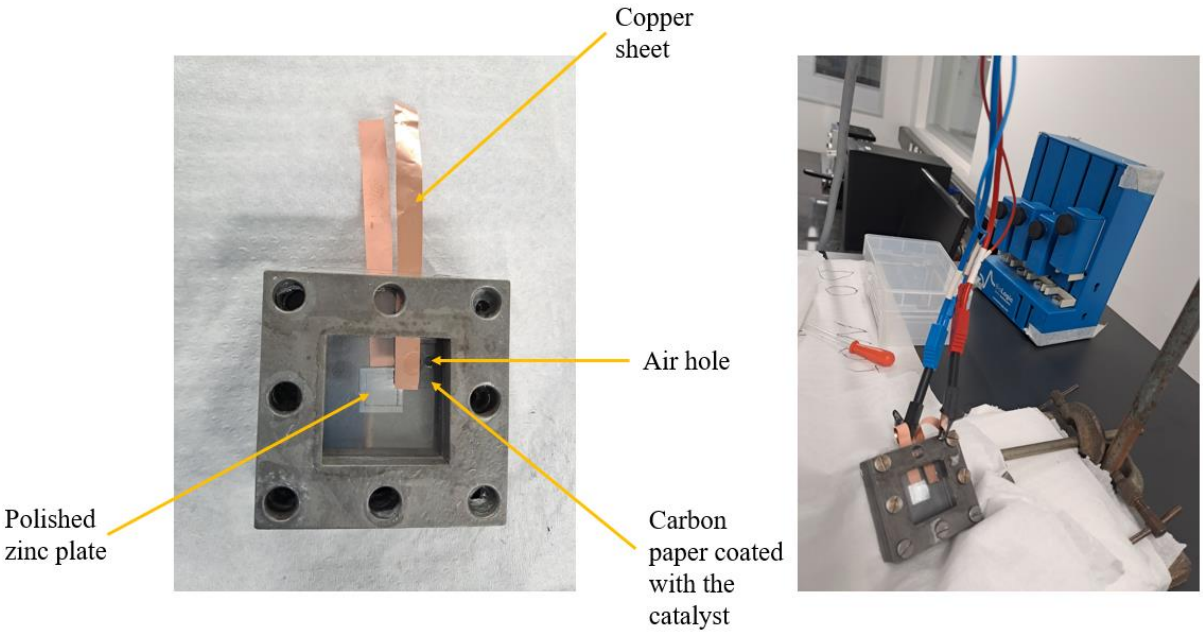

Figure 3. 6: Left: The fully assembled ZAB cell. Right: The ZAB cell that is connected to the battery tester.

3.4. References

(1) Stachowiak, G. W.; Batchelor, A. W.; Stachowiak, G. B. Surface Micrography and Analysis; 2004; pp 165–220. https://doi.org/10.1016/S0167-8922(04)80024-5.

(2) Munir, N.; Hanif, M.; Dias, D. A.; Abideen, Z. The Role of Halophytic Nanoparticles towards the Remediation of Degraded and Saline Agricultural Lands. https://doi.org/10.1007/s11356-021-16139-9/Published.

(3) Kim, S.-G.; Park, O.-K.; Lee, J. H.; Ku, B.-C. Layer-by-Layer Assembled Graphene Oxide Films and Barrier Properties of Thermally Reduced Graphene Oxide Membranes. *Carbon letters* **2013**, *14* (4), 247–250. https://doi.org/10.5714/cl.2013.14.4.247.

(4) Li, Y.; Gong, M.; Liang, Y.; Feng, J.; Kim, J. E.; Wang, H.; Hong, G.; Zhang, B.; Dai, H. Advanced Zinc-Air Batteries Based on High-Performance Hybrid Electrocatalysts. *Nat Commun* **2013**, *4*. https://doi.org/10.1038/ncomms2812.

CHAPTER 4

Onion-like carbon supported high-entropy spinel oxides [$(CoCuFeMnNi)_3O_4$] for robust rechargeable zinc-air batteries.

4.1. Introduction

The looming energy crisis fuelled by overreliance on fossil fuels encouraged the resurgence of century-old zinc-air batteries [1]. This technology is appealing due high theoretical energy density (1086 W h kg^{-1}) with an ample supply of oxygen from the atmosphere, an abundance of raw materials, environmental friendliness, and years of safety validation. In comparison to lithium-ion batteries, primary zinc-air batteries have a 3x higher energy density thus they offer compelling "beyond lithium-ion" technologies [2].

Electrocatalysts of low cost and durability are key to unlocking the full potential of rechargeable zinc-air batteries. The key reactions that accompany the rechargeable zinc-air battery at the air-breathing cathode are oxygen reduction reaction (ORR) and oxygen evolution reaction (OER) and these reactions are without a doubt sluggish [3]. Oxygen is a multiple bonded heteroatom therefore an electrocatalyst is required to aid in breaking the multiple bonds. Noble metal catalysts are known to promote such reactions with Pt known to be an excellent ORR catalyst while IrO_2 and RuO_2 are well-known OER catalysts [4]. However, these catalysts have prohibitive prices which hinder their widespread application. Their lack of sustainability and poor durability fuelled intense research into transition metal-based alloys and oxides.

High entropy materials, termed the new "gold rush" are receiving tremendous interest due to their favourable characteristics, specifically the high stability which is essential in the long-term operation of the battery [5]. High entropy oxides (HEOs) are particularly favourable

because oxides are known to exhibit improved bifunctionality due to adjustments in surface cation oxidation states induced by bulk metal cations in response to reaction conditions [6].

This chapter focuses on developing high entropy spinel oxides ($HESO_x$) for bifunctional ORR/OER activities. To circumvent the poor conductivity of the $HESO_x$, onion-like carbon (OLC) was used as the catalyst support. The catalyst was further treated with acid to improve the physicochemical properties which further enhanced the electrocatalytic and RZAB performances.

4.2. Experimental

4.2.1. Chemicals and materials

The reagents in this study were of analytical grade and were used without further purification. The precursors, $Co(NO_3)_2.6H_2O$, $Cu(NO_3)_2.3H_2O$, $Fe(NO_3)_3.9H_2O$, $Mn(NO_3)_2.4H_2O$, $Ni(NO_3)_2.6H_2O$, ethylene glycol and citric acid were purchased from Sigma-Aldrich. The onion-like carbon (OLC) was obtained by annealing denoted nanodiamonds (98-99% purity, NaBond Technologies Co.) at a temperature of 1300 ℃ as described in the literature [7]. Commercial Pt/C (10 wt. %) and IrO_2 (99.9%) were also obtained from Sigma-Aldrich.

4.2.2. Synthesis

(i) Synthesis of the spinel-based high-entropy oxides $(CoCuFeMnNi)_3O_4$).

The high entropy spinel oxide was synthesized using a one-step powder-forming Pechini method. Briefly, stoichiometric amounts of the metal nitrate salts were prepared, and each metal nitrate salt was then dissolved in de-ionized water and magnetically stirred to obtain adequate homogeneity. Citric acid, 0.4966 g (3.34 mL) was dissolved in deionized water, and this was followed by the addition of 0.4242 g (2.63 mL) ethylene glycol to obtain the CA-EG mixture. The metal nitrate solutions were mixed and added dropwise into the CA-EG mixture and left to stir while heating at 90 ℃. The solution eventually dehydrated into a gel but was

kept at 90 ℃ until the gel burnt, ultimately forming a black metal oxide crystalline powder. The crystalline powder was calcined at 500 ℃ and maintained for 6 h in the air to eliminate any carbonaceous materials. The obtained $(CoCuFeMnNi)_3O_4$ was then annealed at 550℃ for 6 h under a constant Ar atmosphere. The procedure is summarised in **Scheme 4.1**.

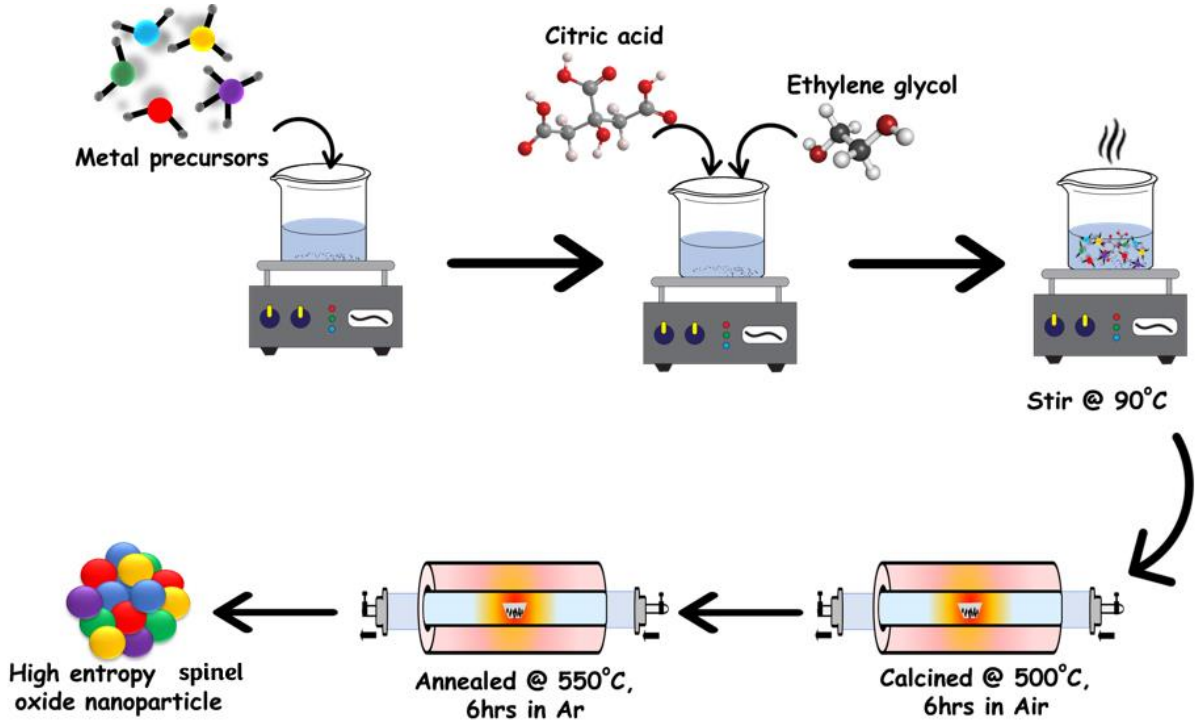

Scheme 4. 1: The schematic representation for the preparation of high entropy spinel oxides $(CoCuFeMnNi)_3O_4$.

(ii) Loading $HESO_x$-550 onto onion-like carbon (OLC).

To briefly expand on the nomenclature, $HESO_x$-550/OLC denotes a composite that consists of 10% $(CoCuFeMnNi)_3O_4$ ($HESO_x$-550) and 90% OLC. The number 550 represents the annealing temperature for the materials. $HESO_x$-550/OLC_{AT} denotes the composite which was acid-treated. To synthesize $HESO_x$-550/OLC_{AT}, 360 mg of OLC was stirred in 20 ml of ethylene glycol in a 3-necked flask. Into this, a solution of 4 ml water, 4 ml ethylene glycol, 0.5 ml HCl (32%) and 40 mg $HESO_x$-550 was added dropwise. A separate mixture of NaOH (0.40 g) in H_2O (0.80 ml) mixed in EG (2.8 ml) was prepared and added to the mixture of H_2O,

EG, HCl and $HESO_x$-550. The reaction mixture was heated at 125 ℃ for 3 h, under nitrogen atmosphere. After cooling to room temperature, the solid products were washed with distilled water until the filtrate pH became neutral. The product was dried at 40 ℃ in a vacuum oven. The procedure is schematically represented in **Scheme 4.2**. The synthesis of $HESO_x$-550/OLC follows the same procedure except that HCl and NaOH were omitted in the sample preparation.

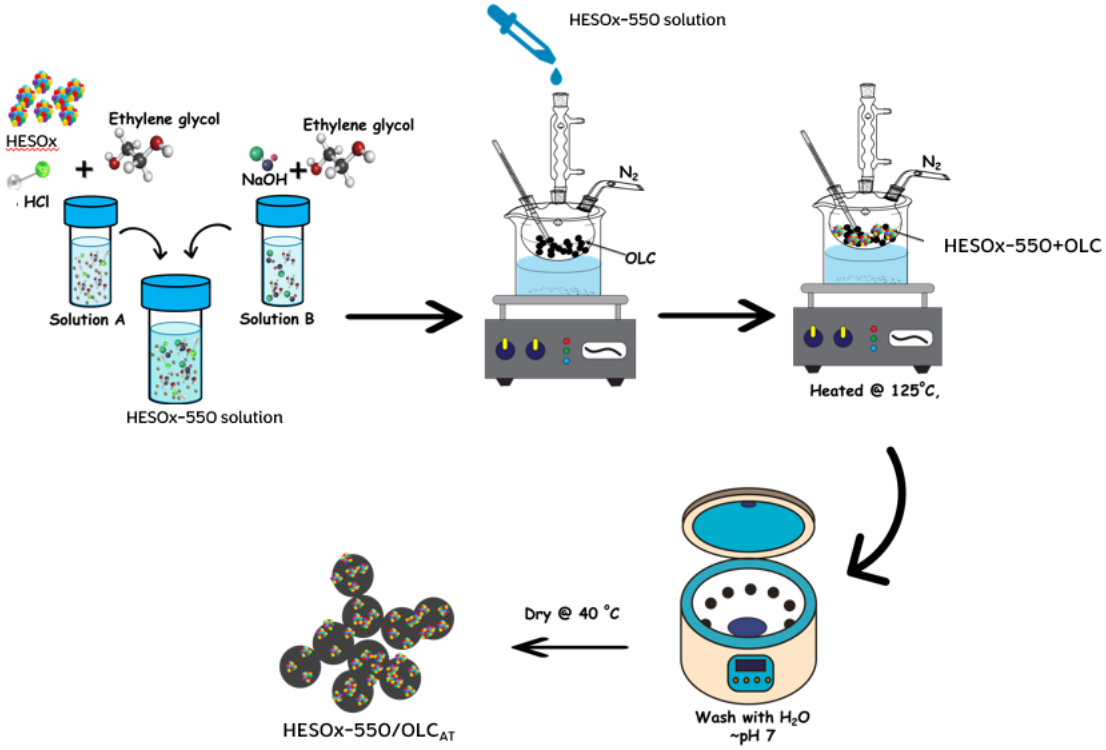

Scheme 4. 2: The schematic representation for loading $HESO_x$-550 onto onion-like carbon (OLC).

4.2.3. Characterizations

XRD characterizations were performed on the Bruker D2 phaser. The Zeiss Auriga Field emission scanning microscopy (SEM) powered by SmartSEM was used to obtain SEM images and the Oxford X-max with Aztech software was used to obtain EDX data. TEM characterizations were carried out using JOEL JEM 2100 at 2000 KV coupled with a Thermo Fischer detector to obtain the EDS images. Thermogravimetric analyses of the samples were

carried out using TGA 4000-Perkim Elmer at a heating rate of 10 ℃ /min, under air (20 ml/min) from 35-900 ℃.

4.2.4. Electrochemical measurements

The electrochemical measurements were carried out at room temperature using the biologic VSP300 potentiostat powered by EC lab. A three-electrode system was used which includes the glassy carbon electrode as the working electrode, Ag/AgCl (filled with saturated KCl solution) as the reference electrode and Pt rod as the counter electrode. O_2-saturated 1 M KOH was used as the electrolyte for both ORR and OER. Linear sweep voltammograms (LSV) were conducted at a scan rate of 5 mV/s. Using the geometrical area of the electrode (0.196 cm^2), the current density was normalized, and the potentials were converted to reversible hydrogen electrode (RHE) using the following Nernst equation:

$E_{RHE} = E_{Ag/AgCl} + 0.059 \times pH + 0.1976$

To calculate the overpotential (η) for OER the following formula was used:

$$\eta\ (V) = E_{RHE} - 1.23$$

The polarization curves were used to calculate the tafel slopes which follow the linear equation:

$$\eta = b(\log j) + a$$

Where b is the Tafel slope and j is the disk current density.

H_2O_2 Selectivity and electron transfer numbers (n) were calculated using the following equations:

H_2O_2 Selectivity: $$\%H_2O_2 = 200\left(\frac{\frac{I_{ring}}{N}}{I_{disk}+\frac{I_{ring}}{N}}\right)$$

Electron transfer number: $$n = \left(\frac{4I_{disk}}{I_{disk}+\frac{I_{ring}}{N}}\right)$$

4.2.5. Rechargeable Zinc-air batteries

A home-made cell was fabricated to measure the performance of the catalysts in rechargeable zinc-air batteries. A zinc plate with a thickness of 0.25 mm was used as the anode and the gas diffusion layer (carbon paper) coated with the catalyst as the air cathode. The carbon paper with a geometric area of 1 cm^2 was used and 10 mg of the catalyst was loaded on the paper. For the electrolyte, 0.2 M zinc acetate was dissolved in 6 M KOH to form zincate ($Zn(OH)_4^{2-}$) and ensure reversible zinc electrochemical reactions at the anode [2]. To prepare the catalyst slurry, 10 mg of $HESO_x$-550/OLC or $HESO_x$-550/OLC_{AT} was dissolved in 20 µL of water, 180 µL of isopropanol and 20 µL of PTFE and stirred on a magnetic stirrer. The coated catalyst was oven-dried at 80 ℃ for 30 min. A rechargeable zinc-air battery with a mixture of Pt/C and IrO_2 (mass ratio of 1:1) as the catalyst was assembled in the same way for comparison.

The biologic battery tester/VSP300 potentiostat was used to collect the reported data on rechargeable zinc-air batteries. The long-term stability was first conducted under shallow cycling conditions at 2 mA cm^{-2} with 30 min discharge and 30 min charge (1 h per cycle). The catalyst was then subjected to harsh cycling conditions (6 h per cycle then 12 h per cycle) to meet the minimum required depth of discharge. To calculate the DOD, the following equation was used:

$$DOD_{Zn} = \frac{A_{cathode} \times j \times t}{A_{Zn} \times h_{Zn} \times \rho_{Zn} \times 819.73}$$

where $A_{cathode}$ is the area of the air cathode, A_{zn} is the area of the zinc anode, j is the current density, t is the discharge time, h_{zn} is the height of the zinc plate and ρ_{Zn} is the density of the zinc plate (it is assumed to be the bulk zinc density of 7.14 g cm^{-3}) [8].

The areal energy density was calculated as follows:

Areal energy density = Current density × discharge voltage × discharge time.

4.3. Results and Discussion

4.3.1. Physical Characteristics

Figure 4.1 (a) depicts the X-ray diffraction patterns for $HESO_x$-550, $HESO_x$-550/OLC, $HESO_x$-550/OLC_{AT} and OLC. The unique crystal structure of the $HESO_x$-550 has diffraction peaks appearing at 18.4°, 30.4°, 35.7°, 37.4°, 43,5°, 53.9°, 57.6° and 62.5° can be attributed to the (111), (220), (311), (222), (400), (422), (511) and (440) miller indices respectively. These diffraction peaks correspond to those of a typical inverse spinel such as Fe_3O_4. Since $HESO_x$ crystallographic information files (.cif) do not exist in the literature, we modelled it using Fe_3O_4 as the parent inverse spinel structure. $HESO_x$-Ozoemena.cif essentially matched the conventional Fe_3O_4 inverse spinel structure, as shown in **Figure 4.1 (a)**. There are slight variations in crystal lattice because $HESO_x$ contains five transition metals with different atomic radii, rather than just one metal such as in Fe_3O_4.

Besides the identified spinel phase, there is a distinct peak at 38.8° which can be attributed to CuO. The Jahn-Teller effect leads to the isolation of Cu whereby the oxygen sublattice around the Cu ion is locally deformed making it difficult for CuO to diffuse into the spinel phase [9].

The XRD pattern of the onion-like carbon (OLC) used to form the $HESO_x$ composites is included in **Figure 4.1. (a)**. The peaks at 2θ = 25.7° and 42.5° correspond to the (002) and (100) carbon characteristic peaks. The absence of 2θ = 43.7˚ and 75.1˚ which correspond to the (111) and (220) diamond planes indicate the purity of the OLC sample which was synthesized from high-temperature annealing of the nanodiamond particles. The $HESO_x$-550/OLC and $HESO_x$-550/OLC_{AT} diffractogram is an amalgam of OLC and pristine $HESO_x$-550. The structure of these composites typifies a spinel crystal system with detectable characteristic peaks at 2θ = 30.0°, 35.3˚, 43.1˚, 57.3 and 62.6˚ which correspond to the (220), (311), (400), (511) and (440) respectively. The other characteristic peaks (those at 2θ = 18.3˚ and 30.5˚) were either engulfed by the prominent OLC peak at 2θ = 25.6˚ (002) or disappeared into the

background due to lower composite amounts of the metal atoms thereby reducing the detectability of the atoms in those planes. That is the OLC comprised 90% of the composite whilst 10% was the $HESO_x$ (refer to the experimental procedure). Acid treatment induced an increase in graphitic carbon diffraction and a significant decrease in $HESO_x$ diffraction. Notably, when compared to the pristine sample, some peaks have either shifted to lower angles indicating a change in lattice parameters leading to lattice expansion. The benefits of this are enhanced ionic conductivity, reduced resistance to charge transfer, and lower overpotentials, thereby improving the reaction kinetics of the $HESO_x$-550/OLC and $HESO_x$-550/OLC_{AT}. **Figure 4.1 (b)** shows the fitted (002) with full width at half maximum (FWHM) values for OLC, $HESO_x$-550/OLC and $HESO_x$-550/OLC_{AT}. The FWHM value for $HESO_x$-550/OLC_{AT} (4.94°) is higher than that of $HESO_x$-550/OLC (3.57°). A higher FWHM value implies smaller particle sizes and therefore larger surface area. The smaller FWHM value suggests a perfect crystalline structure while a larger FWHM value implies defects or imperfections in the crystalline plane thus $HESO_x$-550/OLC_{AT} is more defective than $HESO_x$-550/OLC.

The morphology of the pristine sample and the composites were characterized by TEM as shown in **Figure 4.1 (c-e)**. The HESOx-550 nanocrystals appear to be spherical with different sizes (**Figure 4.1 (c)**). The $HESO_x$ was formed from metal ions with different atomic radii explaining the different sizes. **Figure 4.1 (d)** shows the TEM image for $HESO_x$-550/OLC with spherical OLC rings, however, the shape is destroyed once acid treatment is introduced for $HESO_x$-550/OLC_{AT} in **Figure 4.1 (e)**. **Scheme 4.3** shows how acid treatment changes the OLC structure.

The high-resolution TEM images (HRTEM) for the pristine $HESO_x$-550 are displayed in **Figure 4.1 (f)**. The lattice fringe spacings were measured to be 0.25 nm, 0.29 nm and 0.47 nm which correspond to the interplanar spacing of (311), (220) and (111) planes of a spinel crystalline structure which agrees with the obtained XRD results. The HRTEM image of the

$HESO_x$-550/OLC is shown in **Figure 4.1. (g)** indicating an interlayer distance of 0.337 nm which corresponds to a typically graphitic carbon (002) plane [10,11] and this strongly agrees with the XRD.

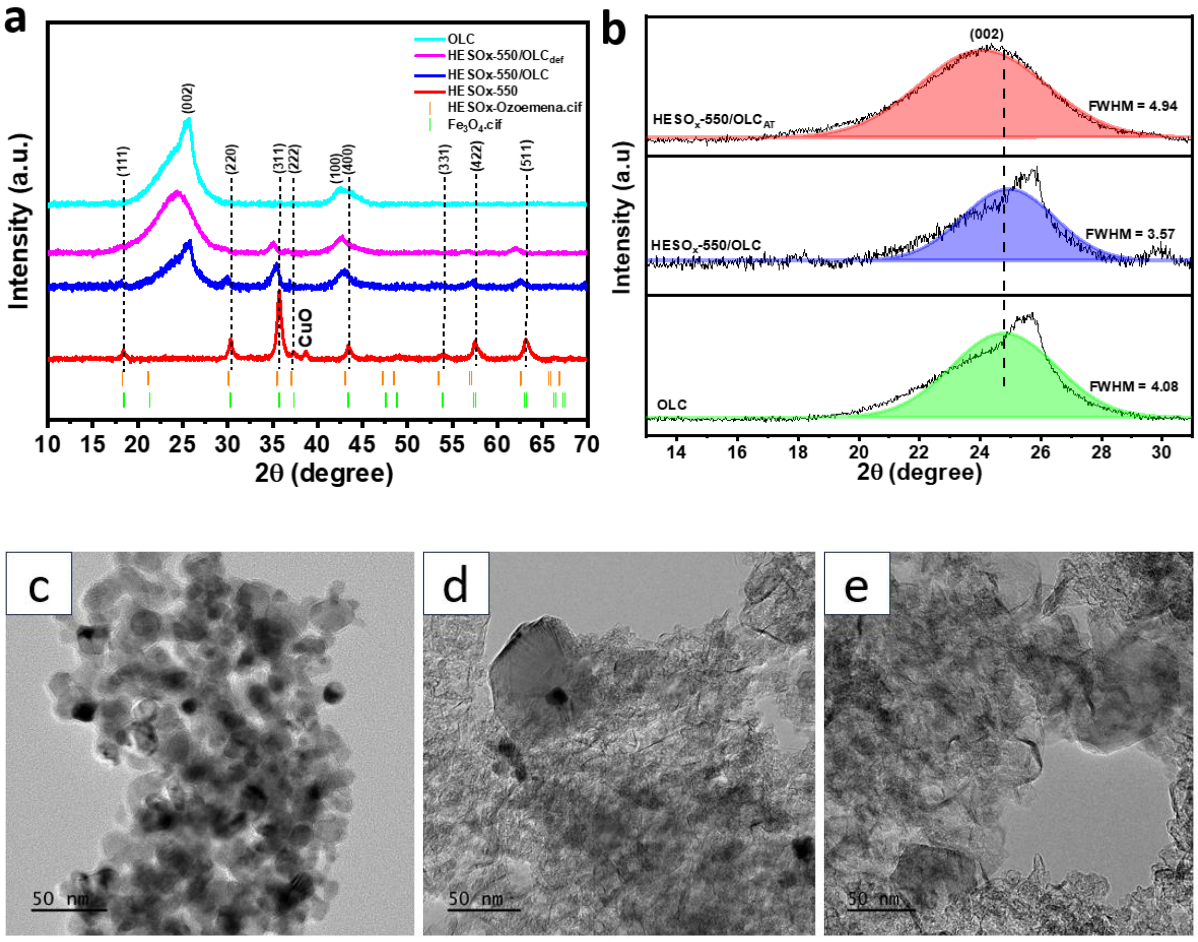

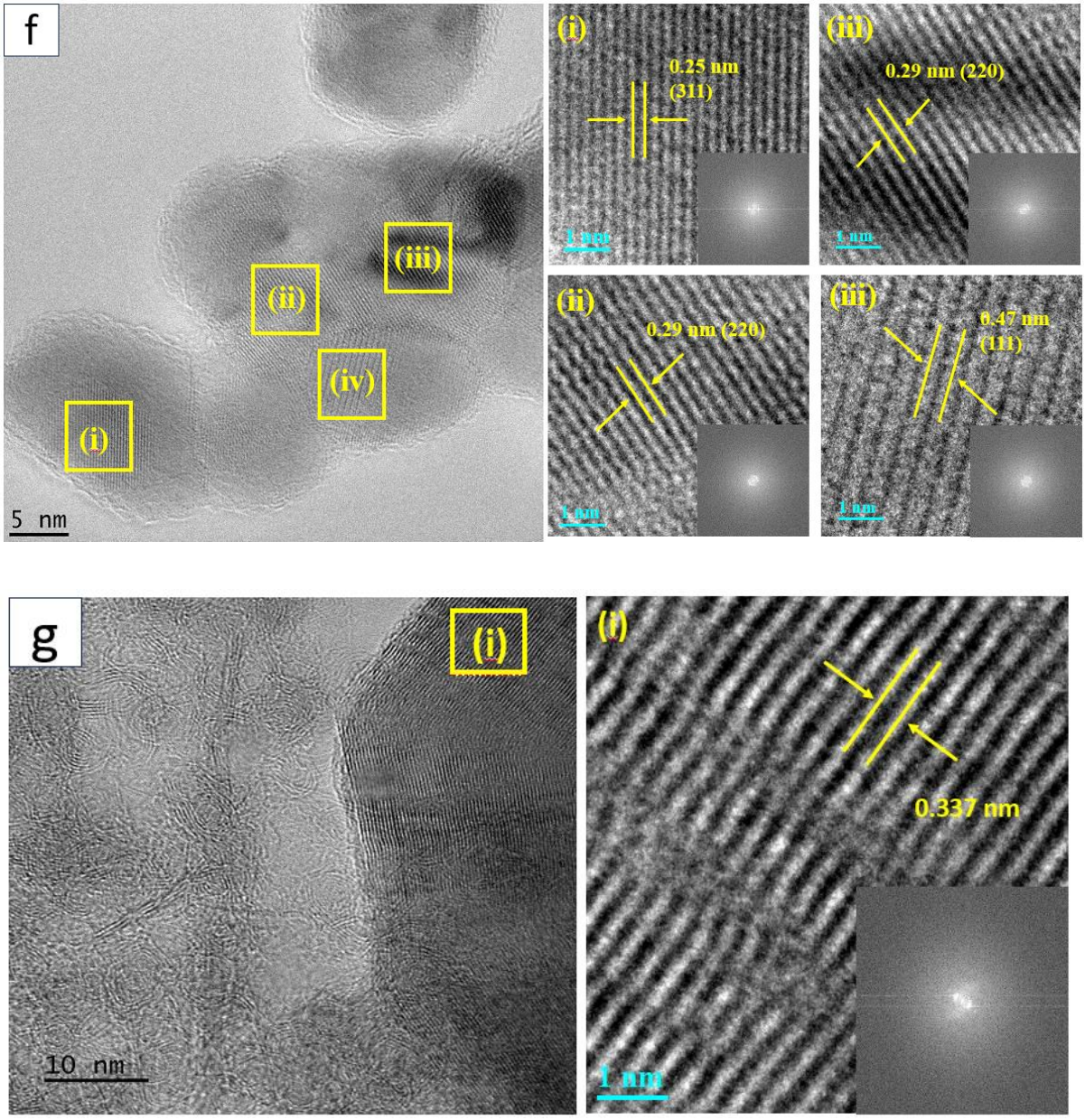

Figure 4. 1: (a) The XRD patterns for $HESO_x$-550, $HESO_x$-550/OLC, $HESO_x$-550/OLC_{AT} and OLC (b) The fitted (002) peaks for OLC, $HESO_x$-550/OLC and $HESO_x$-550/OLC_{AT} with FWHM values. The TEM images for (c) $HESO_x$-550 (d) $HESO_x$-550/OLC (e) $HESO_x$-550/OLC_{AT}. HRTEM images for (f) $HESO_x$-550 and (g) $HESO_x$-550/OLC.

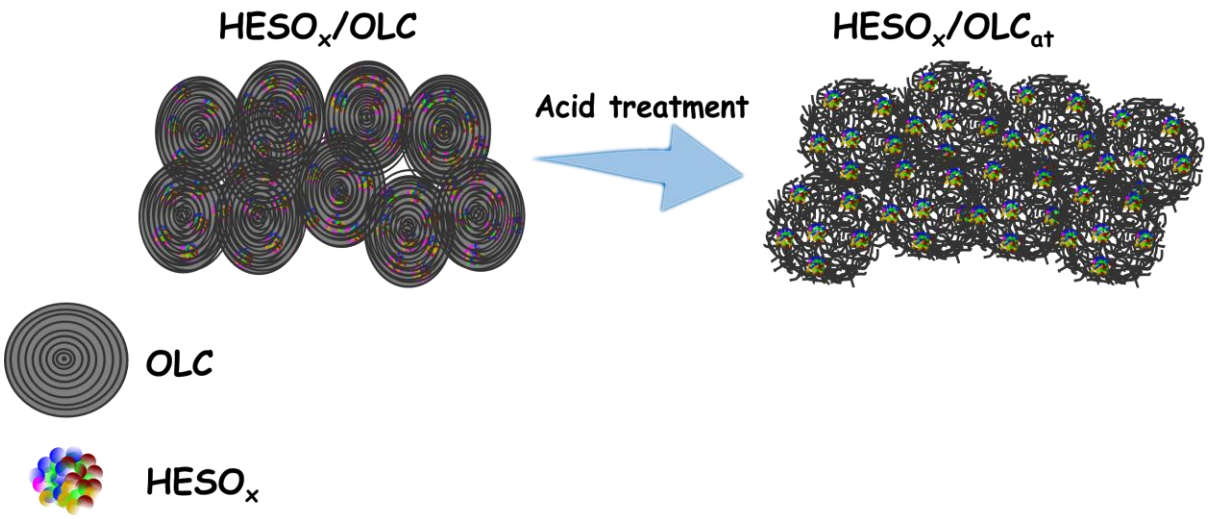

Scheme 4. 3: A scheme depicting the change in the OLC structure after acid treatment.

Raman

Figure 4.2 (a) shows the Raman spectra of $HESO_x$-550. Five Raman modes, that is A_{1g} + E_g + $3F_{2g}$ were observed for the $HESO_x$-550 and are similar to that of ferrite in a spinel structure at ambient conditions. The modes below 600 cm^{-1} are linked to the motion of oxygen atoms in octahedral BO_6 and those above 600 cm^{-1} are linked to the motion of oxygen atoms in the tetrahedral AO_4 group. F_{2g} (1) is due to the translational movement of four oxygen atoms along with a metal ion at the tetrahedral site. The E_g mode is because of the symmetric bending of oxygen regarding the metal ion while F_{2g} (3) is a result of the asymmetric bending of oxygen. F_{2g} (2) is due to the asymmetric stretching of Fe (Ni) and O while the A_{1g} is a result of the symmetric stretching of oxygen atoms on Fe–O (and Ni–O) bonds in the tetrahedral sites.

Figure 4.2 (b & c) shows the Raman spectra for the $HESO_x$ composites with characteristics for sp^2 carbon disorder-induced (D) and graphite (G) bands. The two strong peaks at 1342 cm^{-1} and 1532 cm^{-1} are attributed to the G and D band respectively. The D-band represents the defect sites associated with vacancies therefore the higher intensity of this band implies more defects [12]. The integrated intensity ratio I_D/I_G for the $HESO_x$-550/OLC_{AT} shows a significant increase compared to $HESO_x$-550/OLC implying higher defect density. The I_D/I_G ratio also

provides the degree of functionalization therefore the increased ratio in $HESO_x$-550/OLC_{AT} provides evidence that the onion-like carbon was functionalized with HCl. As a result of functionalization, the sp^2 of a carbon bond becomes sp^3 hybridized.

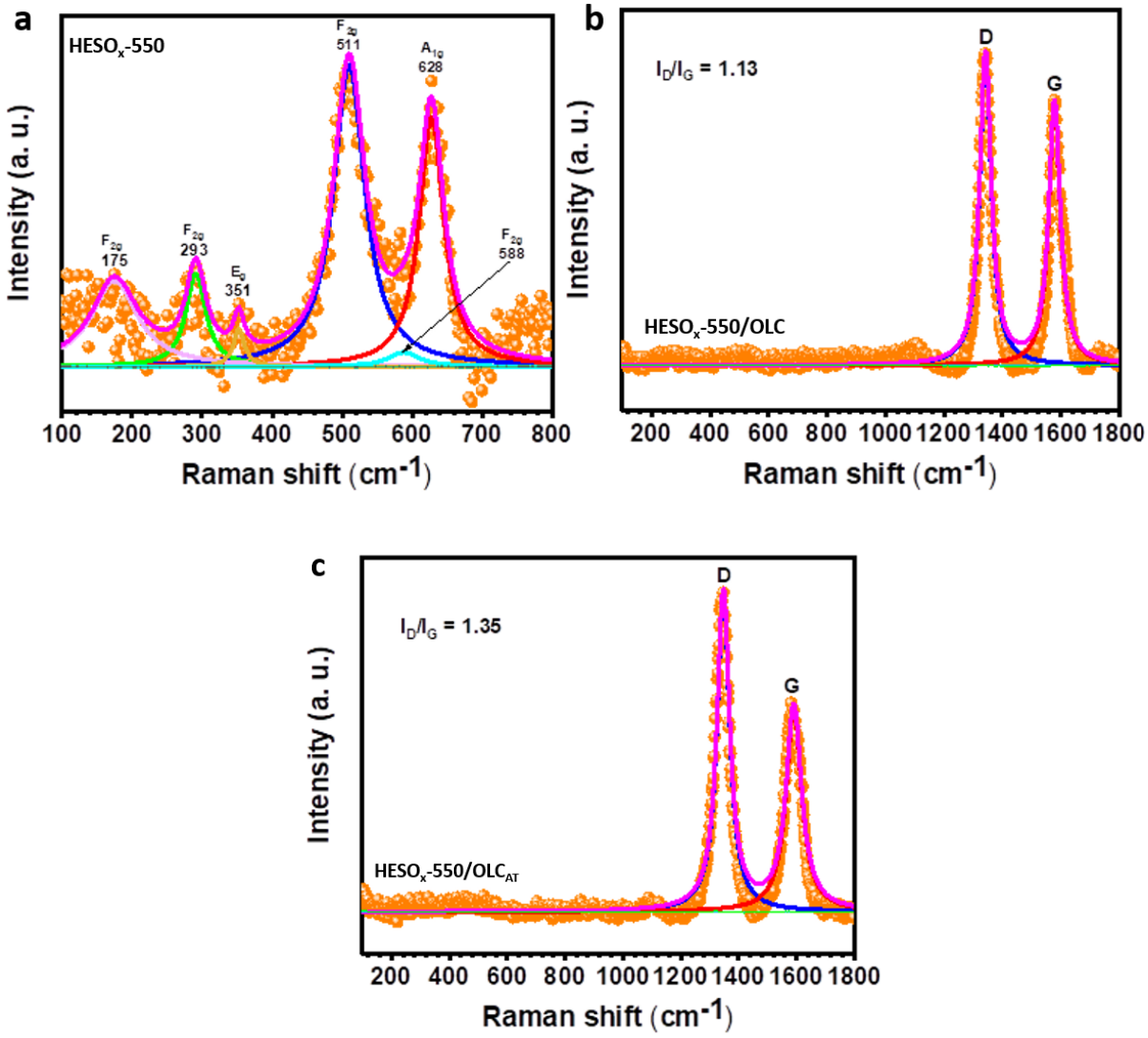

Figure 4. 2: The Raman spectra for (a) $HESO_x$-550 (b) $HESO_x$-550/OLC and (c) $HESO_x$-550/OLC_{AT}.

XPS

X-ray photoelectron spectroscopy was used to analyse the surface composition and chemical states of the catalysts. Previous studies established the vital role played by oxygen vacancies in promoting improved ORR catalytic activities in oxides. In the presence of vacant oxygen

sites, oxygen species can be adsorbed and desorbed, and more efficient mass transport processes can be achieved [13]. The O1s spectra shown in **Figure 4.3 (a)** were analysed. Three major peaks were observed for the pristine $HESO_x$-550 sample with 529.1 eV, 529.5 eV and 531.1 eV binding energies corresponding to lattice oxygen (O_L), defects site with low oxygen coordination (O_v), physically and chemically adsorbed water on the material surface (O_a) [13],[14]. These binding energies shifted to more positive values when OLC was introduced to the samples. The oxygen vacancy content in $HESO_x$-550/OLC_{AT} (74.90%) is much higher than that of $HESO_x$-550/OLC (65.90%) and $HESO_x$-550 (49.99%) representing higher ORR catalytic activity.

Figure 4.3 (b-f) represents the high-resolution XPS of Co 2P, Cu 2P, Fe 2P, Mn 2P and Ni 2P for $HESO_x$-550, $HESO_x$-550/OLC and $HESO_x$-550/OLC_{AT}. The Co 2P has doublet peaks at 779.9 eV and 794.9 eV for $HESO_x$-550 and these are attributed to Co $2P_{3/2}$ and Co $2P_{1/2}$ caused by spin orbit coupling. Co exists in Co^{2+} (779.6 eV for $2P_{3/2}$) and Co^{3+} (781.3 eV for $2P_{3/2}$) oxidation states. The doublet $2P_{3/2}$ and $2P_{1/2}$ peaks are observed at 934.2 eV and 952.1 eV for Cu. Cu exists in Cu^{+} (933.1 eV) and Cu^{2+} (934.7 eV) oxidation states for the $2P_{3/2}$ orbital. Fe 2P displays a peak at 709.9 eV which is assigned to Fe^{2+} and a peak at 712.2 eV assigned to Fe^{3+} for the Fe $2P_{3/2}$ orbital. Mn 2P has two peaks at 641.5 eV and 643.4 eV assigned to Mn^{3+} ($2P_{3/2}$) and Mn^{4+}($2_{P3/2}$) respectively. The binding energies for Ni 2P are 854.1 eV ($2P_{3/2}$) and 855.4 eV ($2P_{3/2}$) for Ni^{2+} and Ni^{3+} respectively. The above-mentioned binding energies are for $HESO_x$-550. In comparison to $HESO_x$-550, the introduction of OLC to the samples changed the local chemical environments of the Co 2P, Cu 2P, Fe 2P, Mn 2P and Ni 2P elements. The metal oxidation states for the elements in $HESO_x$-550/OLC and $HESO_x$-550/OLC_{AT} shifted to higher binding energies when compared to $HESO_x$-550. This shift implies the electrons transfer from these elements to the surrounding atoms.

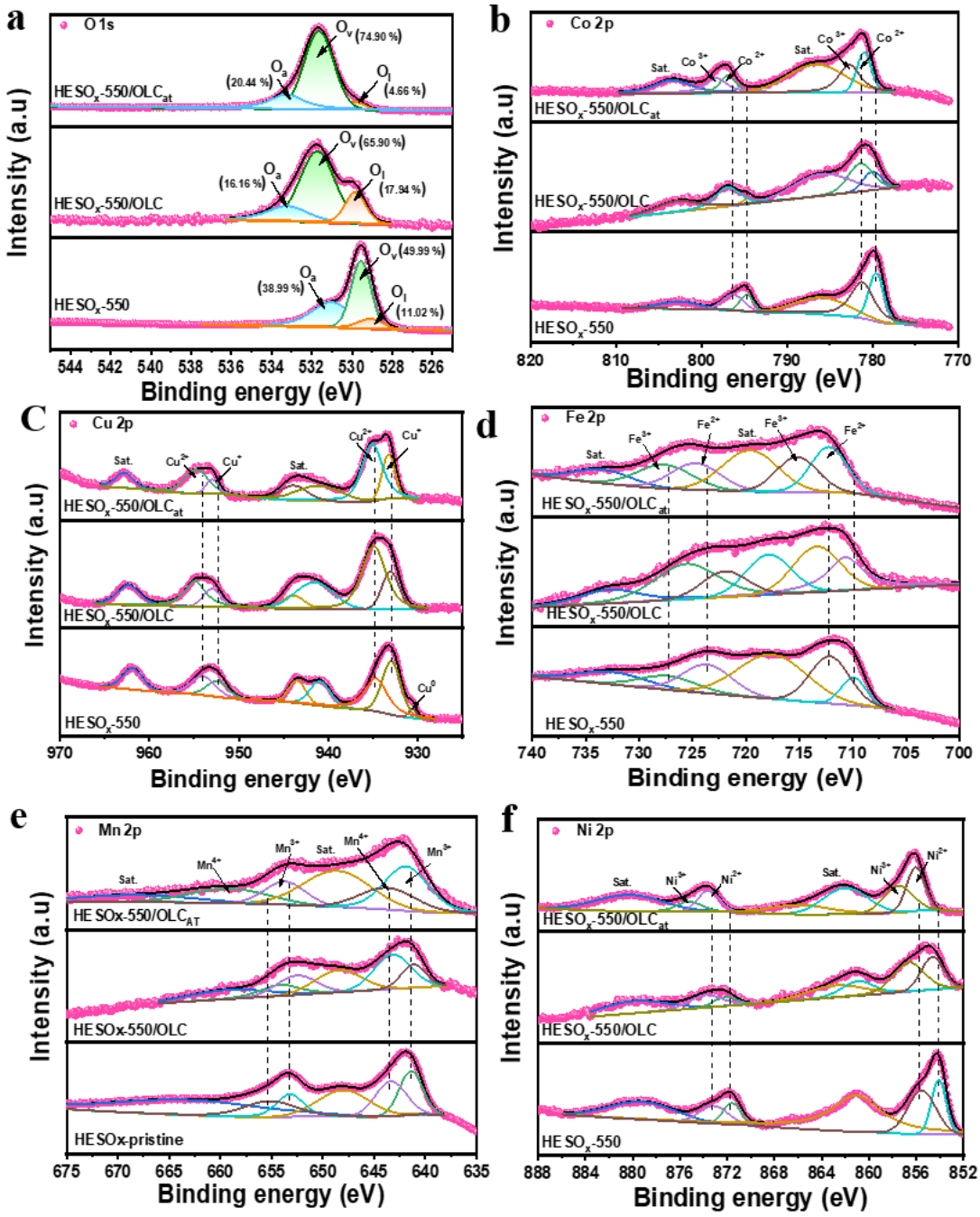

Figure 4. 3: XPS spectra of (a) O1s, (b) Co 2p, (c) Cu 2p, (d) Fe 2p, (e) Mn 2p and (f) Ni 2p.

TGA

The TGA curves and their corresponding first derivative thermogravimetry (DTG) curves for HESOx-550, $HESO_x$-550/OLC, $HESO_x$-550/OLC_{AT} and OLC are depicted in **Figure 4.4**. Carbon is a highly combustible material thus the OLC sample was completely burnt in the air leaving no residue and this implies the high purity of the sample (**Figure 4.4 (a)**). However,

the $HESO_x$-550/OLC and $HESO_x$-550/OLC_{AT} have a 6.1% residue implying that there are metals left after the OLC burnt. The degradation is not observed in $HESO_x$-550 compared to $HESO_x$-550/OLC and $HESO_x$-550/OLC_{AT} due to the absence of carbon in the sample. $HESO_x$-550 shows very high thermal stability which is one of the favourable characteristics for high-entropy materials. The small degradation of -2.1% in the $HESO_x$-550 sample is attributed to the removal of adsorbed species on the surface of the sample [15]. DTG graphs and their respective temperature of earliest mass change rate (T_{max}) values are indicated in **Figure 4.4 (b).** A single typical DTG peak is observed for $HESO_x$-550/OLC, $HESO_x$-550/OLC_{AT} and OLC which is attributed to the combustion of carbon during thermal degradation in air. The absence of the peak in $HESO_x$-550 is due to the absence of carbon in the sample. $HESO_x$-550/OLC_{AT} has the earliest T_{max} (528.4 ℃) followed by $HESO_x$-550/OLC (622.4 ℃) and OLC (750.3 ℃). Observing a lower T_{max} indicates that less heat energy is required to overcome the high density of defects in sp^3 hybridized carbon bonds [16]. This finding is consistent with the Raman spectroscopy data which proved that $HESO_x$-550/OLC_{AT} is more defective and functionalized.

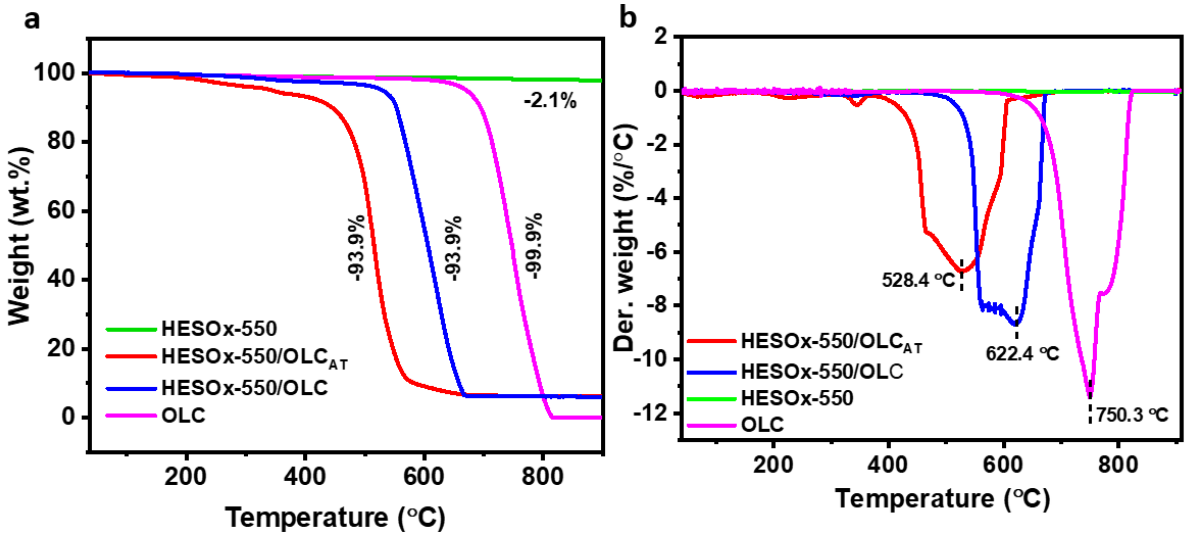

Figure 4. 4: (a) TGA and (b) DTG for $HESO_x$-550, $HESO_x$-550/OLC_{AT}, $HESO_x$-550/OLC and OLC.

UPS

Ultraviolet photon spectroscopy (UPS) studies were performed to analyse the work function (ϕ) ($E_{vac} - E_F$) and determine the Fermi level position with regards to the valence band maximum ($E_F - E_{VMB}$) of the $HESO_x$ samples. **Figure 4.5 (a)** lays out the full UPS spectra for all three $HESO_x$ samples while **Figures 4.5 (b) & (c)** outline the secondary emission and the zoomed area near the valence band respectively for $HESO_x$-550. The zoomed-in area for $HESO_x$-550/OLC and $HESO_x$-550/OLC_{AT} are included in the supporting documents (**Figure S3**).

The work functions (WF) of oxides were calculated using the following equation: $\Phi = h\nu - (E_{cut\text{-}off} - E_{VB})$ where Φ represents the work function, $h\nu$ is the incident photoelectron energy of He (I), which is 21.2 eV. The work functions are 5.37 eV, 5.35 eV and 5.46 eV for $HESO_x$-550, $HESO_x$-550/OLC and $HESO_x$-550/OLC_{AT} respectively. $HESO_x$-550/OLC_{AT} has the highest WF meaning it requires more energy to change its electronic state [17]. An increase in oxygen vacancies implies a reduced work function indicating that the electron donation activation barrier between the electrocatalyst surface and the reactant is lower. This data contradicts the O1s XPS.

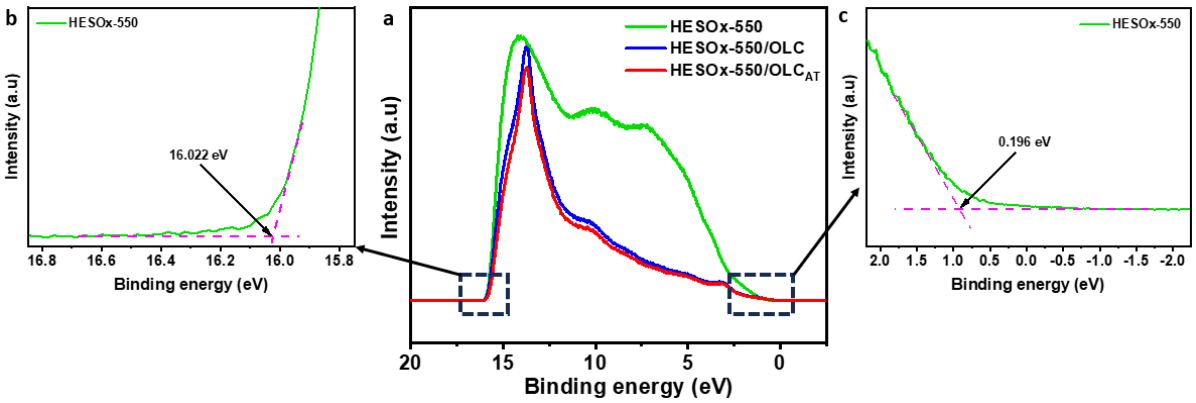

Figure 4. 5: (a) UPS spectrum for $HESO_x$ samples. (b) Left plot: Secondary electron emission for $HESO_x$-550 (c) Right plot: The zoomed area near the valence band for $HESO_x$-550.

BET

The physical properties of the $HESO_x$ samples such as surface area, pore volume and pore diameter were analysed using BET and are summarised in **Table 4.1.** The addition of OLC to the $HESO_x$-550 catalysts brought significant improvement to the physical properties of the composites. The surface area of the $HESO_x$-550 composites was increased due to the superior surface area of OLC which is one of its favourable characteristics. It was found that the treatment of $HESO_x$-500/OLC with HCl affected its porous structure to a certain extent. Treatment with HCl increased the surface area from 387.97 m^2/g to 434.21 m^2/g and the pore volume from 0.987 cm^3/g to 1.11 cm^3/g for $HESO_x$-550/OLC and $HESO_x$-550/OLC_{AT} respectively. The increase in textural parameters in $HESO_x$-550/OLC_{AT} may be attributed to the change in the onion-like structure to a more disordered structure which exposes more active sites. The $HESO_x$-550/OLC_{AT} undergoes pore and surface engineering through acid treatment. A decrease in pore diameter can be observed from 124.45 Å, 101.79 Å and 100.09 Å for $HESO_x$-550, $HESO_x$-550/OLC and $HESO_x$-550/OLC_{AT} respectively. The smallest pore diameter enhances the shielding effect for molecules with larger diameters by limiting the adsorbates and solvents thereby increasing the adsorption capacity of a catalyst [18]. This favours electrocatalysis by allowing smaller molecules such as O_2 and OH^- to diffuse and eliminate larger molecules such as CO_2.

Table 4. 1. Brunauer-Emmett-Teller (BET) textural of the as-prepared HESOx-550 catalyst and composites.

Samples	**BET parameters**		
	BET Surface Area (m^2/g)	Pore Volume (cm^3/g)	Pore diameter (Å)
$HESO_x$-550	14.83	0.0461	124.45
$HESO_x$-550/OLC	387.97	0.987	101.79
$HESO_x$-550/OLC_{AT}	434.21	1.11	100.09

EPR

Electron paramagnetic resonance (EPR) was applied to identify oxygen vacancies in $HESO_x$ samples as shown in **Figure 4.6**. There was no signal for $HESO_x$-550. The strong EPR signal with a g-value of 2.068 can be ascribed to the unpaired electrons in the $HESO_x$ composites indicating the existence of oxygen vacancies in the samples. As the EPR signal intensity increases so does the amount of oxygen vacancies [19]. The intensity of $HESO_x$-550/OLC_{AT} is higher than that of $HESO_x$-550/OLC therefore $HESO_x$-550/OLC_{AT} is rich in oxygen vacancies. These results are consistent with those of the O1s XPS. Oxygen vacancies are advantageous for catalysis as they promote adsorption and reactivity of gases such as O_2 [20]. Despite the contradiction observed in the UPS, the EPR corroborates the O1s XPS by proving that $HESO_x$-550/OLC_{AT} has more oxygen vacancies than $HESO_x$-550/OLC.

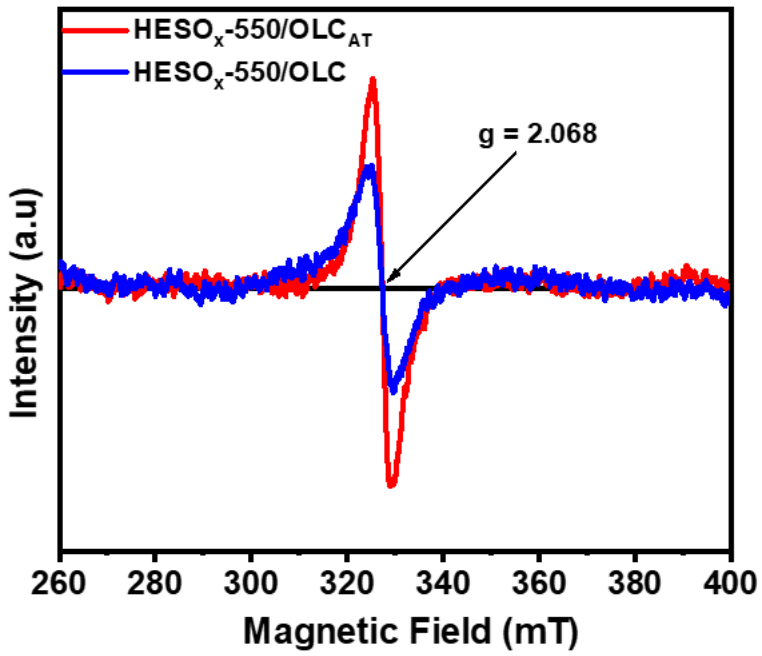

Figure 4. 6: EPR spectra recorded at room temperature for $HESO_x$-550/OLC and $HESO_x$-550/OLC_{AT}.

4.3.2. Electrochemical measurements

. The prepared $HESO_x$ materials were studied as potential bifunctional electrocatalysts for ORR and OER in alkaline solutions. The ORR performances of these materials were measured in 1 M KOH oxygen-saturated environment at 1600 rpm as depicted in **Figure 4.7 (a)**. $HESO_x$-550/OLC_{AT} ($E_{1/2}$ = 0.83 V) and $HESO_x$-550/OLC ($E_{1/2}$ = 0.82 V) exhibited slightly similar ORR activities based on the half-half wave potential ($E_{1/2}$) values. The commercial Pt/C ($E_{1/2}$ = 0.93 V) exhibits better ORR activity than the $HESO_x$ composites due to the noble nature of the Pt which is the best-known catalyst for ORR [21–23]. With the increase in rotation rates, the current density increases as shown in **Figure 4.7 (b) & (c)**. The insert is the Levich analysis for the $HESO_x$-550/OLC_{AT} and $HESO_x$-550/OLC. The $HESO_x$-550/OLC_{AT} exhibits better electron transfer (3.4) compared to $HESO_x$-550/OLC (2.7). The electron transfer mechanism for $HESO_x$-550/OLC_{AT} was further proved using RRDE measurements. RRDE polarization curves (**Figure S4**) for $HESO_x$-550/OLC_{AT} were recorded at 1600 rpm and used to calculate

the electron transfer numbers (n) and the H_2O_2 selectivity. **Figure 4.7 (d)** further shows that the electron transfer for the HESOx-550/OLC_{AT} is less than the required 4 electrons which corroborates the results obtained from the RDE measurements. The H_2O_2 selectivity of 50% was obtained suggesting the reaction occurs through the $2e^-$ pathway.

The ORR stability for the $HESO_x$-550/OLC_{AT} was performed using accelerated durability tests at 50 mV/s. After 30k cycles, the $E_{1/2}$ value for $HESO_x$-550/OLC_{AT} shifted to a negative potential as depicted in **Figure 4.7 (e)**. The $\Delta E_{1/2}$ value for $HESO_x$-550/OLC_{AT} after 30k cycles (**Figure S5**) is 15 mV which is better than the high entropy catalyst reported in the literature [24].

The OER performances of the prepared catalysts were measured in an O_2-saturated 1 M KOH electrolyte at a scan rate of 5 mV/s. As depicted by the polarization curves (**Figure 4.7 (g)**) $HESO_x$-550/OLC_{AT} demonstrated the lowest overpotential (300 mV) to reach the current density of 10 mA cm^{-2} compared to $HESO_x$-550/OLC (370 mV) and the OER benchmark catalyst, IrO_2 (450 mV). The effectively promoted OER activity for $HESO_x$-550/OLC_{AT} is also illustrated by the smallest Tafel slope (48.37 mV dec^{-1}) compared to $HESO_x$-550/OLC (82.97 mV dec^{-1}) and IrO_2 (98.45 mV dec^{-1}) (**Figure 4.7 (h)**). The $HESO_x$-550/OLC_{AT} electrochemical activities were further compared to the ones in the literature (**Table S2**). $HESO_x$-550/OLC_{AT} has better electrocatalytic performances compared to most catalysts in the literature. Chrono-potentiometric measurements for $HESO_x$-550/OLC_{AT} and $HESO_x$-550/OLC were recorded at 10 mA cm^{-2} for 10 h to test for OER stability as illustrated in **Figure 4.7 (i)**. For practical applications, the catalyst should be durable. The HESOx-550/OLC_{AT} potential remains at 1.53 V for the 10 h duration, however, the potential for $HESO_x$-550/OLC (1.66 V) quickly degraded after 6 h. This proves that the $HESO_x$-550/OLC_{AT} catalyst is more sustainable and durable than the $HESO_x$-550/OLC. The excellent ORR and OER parameters are owed to the improved physicochemical properties of the $HESO_x$-550/OLC_{AT}.

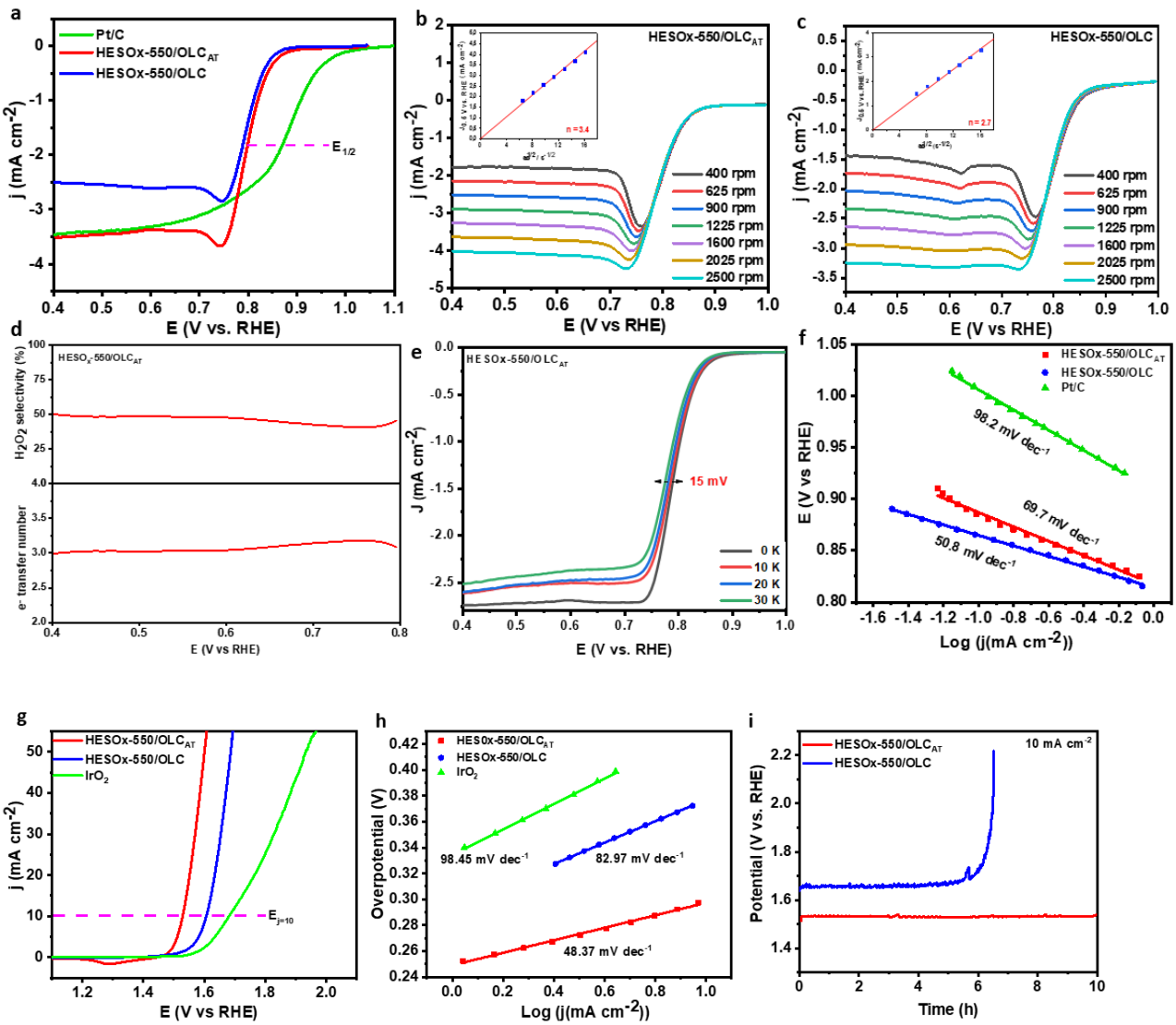

Figure 4. 7: (a) ORR polarization curves at 1600 rpm in O_2 saturated 1 M KOH. ORR polarization curves for (b) $HESO_x$-550/OLC_{AT} and (c) $HESO_x$-550/OLC at different rotation speeds. The insert in (b) & (c) is a representation of the Levich analysis based on the RPMs. (d) The electron transfer number and amount of hydrogen peroxide (H_2O_2) produced in an alkaline medium for $HESO_x$-550/OLC_{AT}. (e) The durability of HESOx-550/OLC_{AT} after different CV cycles. (f) ORR Tafel slopes for all the samples. (g) OER polarization curves at 1600 rpm in O_2 saturated 1 M KOH. (h) OER tafel slopes. (i) Chronopotentiometry measurements for the prepared samples.

4.3.3. DFT

Density functional theory (DFT) calculations were carried out to determine the Gibbs free energy for the ORR/OER intermediates on the $CoCuFeMnNi)_3O_4$ (311) and OLC (002) surfaces**. Table 4.2.** shows all ORR/OER intermediates and their Gibbs free energies for $HESO_x$-550/OLC and $HESO_x$-550/OLC_{AT}. The rate-determining step in OER is the reaction between O* and the electrolyte to form OOH* [25]. This reaction involves the highest energy barrier. The Gibbs free energy difference between OOH* and O* for $HESO_x$-550/OLC is 22.695 eV while that of $HESO_x$-550/OLC_{AT} is 22.354 eV. $HESO_x$-550/OLC_{AT} displayed a lower energy barrier for the OER rate-determining step than $HESO_x$-550/OLC making it a more desirable OER catalyst. The O* to OH* step is considered the rate-determining step for ORR therefore the energy barrier for $HESO_x$-550/OLC_{AT} is 1.01 eV which is lower than that of $HESO_x$-550/OLC (1.1251 eV) therefore it is a more desirable catalyst for ORR. The catalyst with a lower energy barrier for ORR/OER agrees with the experimentally obtained data which suggested $HESO_x$-550/OLC_{AT} to be the best catalyst for both ORR and OER. These results demonstrate that acid-treating the catalyst significantly reduced the energy barriers for the rate-determining steps in OER and ORR.

Table 4. 2: Summary of Gibbs free and adsorption energies for ORR/OER intermediates.

Catalyst	**Adsorbate**	**Gibbs Free energy (eV)**	**Adsorption energy (eV)**
$HESO_x$-550/OLC	O*	-1.618	-1.618
	O_2*	-3.384	-24.110
	H*	-1.097	-1.097
	OH*	-2.743	-10.773
	OOH*	-24.314	-53.925

	H_2O_2*	-4.725	-45.193
$HESO_x$-550/OLC_{AT}	O*	-1.620	-1.620
	O_2*	-3.320	-24.046
	H*	-1.090	-1.090
	OH*	-2.630	-10.659
	OOH*	-23.974	-53.585
	H_2O_2*	-4.676	-45.144

4.3.4. Rechargeable Zinc-Air batteries

Owing to the desirable bifunctional activity of the catalysts during ORR and OER, the catalysts were further tested for applicability in rechargeable zinc-air batteries. The potential difference between OER potential @ 10 mA cm^{-2} ($E_{j=10}$) and half-wave ($E_{1/2}$) ORR potential for $HESO_x$-550/OLC_{AT} (ΔE = 0.70 V) is less than that of $HESO_x$-550/OLC (ΔE = 0.78 V) and Pt/C-IrO_2 (0.75 V) suggesting better performance in rechargeable zinc-air batteries (**Figure 4.8 (a)**). The "bifunctionality index" (ΔE) is a measure of a catalyst's ability to facilitate both the forward and reverse direction of a reaction therefore the smaller the value, the better the bifunctionality. The rechargeable zinc-air batteries were constructed using $HESO_x$-550/OLC_{AT} and $HESO_x$-550/OLC as the catalysts at the air cathode, a polished zinc plate as the anode and an alkaline aqueous electrolyte containing 6 M KOH + 0.2 M Zinc acetate. Rechargeable zinc-air batteries with the air cathode consisting of the commercial Pt-C/IrO_2 (1:1 ratio) were assembled for comparison. The schematic of the RZAB is shown in **Figure 4.8 (b)**.

The power density plots extracted from the discharge profiles of all catalysts are illustrated in **Figure 4.8 (c)**. The $HESO_x$-550/OLC_{AT} battery has a peak power density of 154.3 mW cm^{-2} which is lower than that of Pt/C-IrO_2 (200.6 mW cm^{-2}), but, higher than that of $HESO_x$-

550/OLC (141.0 mW cm^{-2}). The notable high-power density for the Pt/C-IrO_2 battery is likely to be due to the higher metal content (10%Pt/C+99.9% IrO_2) in the catalyst compared to the $HESO_x$-550/OLC_{AT} (only 10%). The noble nature of the Pt also plays an important role in the power density as it is the best-known ORR catalyst [26–28]. Although the peak power density of Pt/C-IrO_2 surpasses that of HESOx-550/OLC_{AT}, Pt/C-IrO_2 suffers from poor stability. The high-power density of $HESO_x$-550/OLC_{AT} compared to $HESO_x$-550/OLC can be ascribed to the larger surface area of $HESO_x$-550/OLC_{AT} making its contact with the electrolyte more effective therefore increasing the catalytic efficiency of the catalyst [29].

Figure 4.8 (d) shows the voltage gaps of the $HESO_x$-550/OLC_{AT} catalyst at various current densities. Notably, the gaps are less than 1 V indicating lower potential differences between ORR/OER, therefore excellent bifunctionality for $HESO_x$-550/OLC_{AT}. The galvanostatic discharge potential of the electrode only declines gradually with increasing current densities indicating good rate capability for $HESO_x$-550/OLC_{AT} (**Figure 4.8 (e)**). The stability of the $HESO_x$-550/OLC_{AT} and Pt/C-IrO_2 catalysts were tested during shallow cycling by galvanostatic discharge-charge cycles at a low current density of 2 mA cm^{-2} as shown in **Figure 4.9 (a)**. Each cycle is 1 h long with 30 min discharging and 30 min charging. The initial discharge voltages are 1.29 V, 1.25 V and 1.32 V for $HESO_x$-550/OLC_{AT}, $HESO_x$-550/OLC (**Figure S9** in the supporting documents) and Pt/C-IrO_2 respectively. These voltages are superior to most catalysts reported in the literature (**Table 2.1**). The initial voltage gaps (ΔE) between the discharging and the charging for HESOx-550/OLC_{AT}, HESOx-550/OLC (**Figure S9**) and Pt/C-IrO_2 are 0.58 V, 0.65 V and 0.54 V respectively at 2 mA cm^{-2}. Although Pt/C-IrO_2 exhibits the best voltage gap, the value quickly increases to 0.82 V after 20 h indicating the poor stability of the material. However, the $HESO_x$-550/OLC_{AT} and $HESO_x$-550/OLC (**Figure S9**) catalysts maintain a steady voltage gap over long cycling periods indicating the good stability effect introduced by the high entropy materials. The $HESO_x$-550/OLC_{AT} battery

continues to display good working performance by maintaining a discharge voltage which is above 1.2 V for a period of over 303 h (303 cycles) while the standard cell (Pt/C-IrO_2) only lasted for less than 100 h before the voltage drops to the set minimum of 0.8 V. Generally, a decline in discharge voltage as the battery cycle indicates diminished reversibility.

Due to the superiority of the $HESO_x$-550/OLC_{AT}, the stability of the catalyst was further tested during deep discharging and charging processes as illustrated in **Figure 4.9 (b)**. The battery noticeably deteriorates quickly at a high current density of 10 $mAcm^{-2}$ and long cycling times due to harsh conditions. The discharge voltage for Pt/C-IrO_2 quickly declines after the first cycle due to the carbon support detaching from Pt [30]. It is recommended that researchers cycle zinc-air batteries at 35 mWh cm^{-2} to compete with Li-ion batteries [31]. However, due to non-standardized cycling protocols, most papers in the literature fall below the minimum areal energy as shown in **Table 2.1**. In **Figure 4.8 (b)** the cell was first cycled at an areal energy of 37.2 mWh cm^{-2} then the cycle length was increased after 42 h to obtain an even higher areal energy of 73.2 mWh cm^{-2}. These areal energies are higher than most reported in the literature (**Table 2.1**). Although the cell shows slight deterioration after 80 h, the catalyst proved its potential applicability towards recharging zinc-air batteries. An areal capacity of >10 mAh cm^{-2} is recommended when cycling RZABs [8,32]. **Figure 4.8 (f)** shows the areal capacity under shallow cycling conditions while **Figure 4.9 (c)** shows the areal capacity under harsh DOD conditions. The areal capacity under shallow cycling conditions is 10 times lower than the recommended therefore this proves that discharging/charging the battery faster and using a small current density is not the best way to prove the battery rechargeability since the minimum required metric for scale-up is not met. **Figure 4.9 (d)** shows the discharging and charging of the $HESO_x$-550/OLC_{AT} rechargeable zinc-air battery under constant DOD conditions. The $HESO_x$-550/OLC_{AT} battery has an initial ΔE of 0.66 V which is superior to that of Pt/C-IrO_2 (ΔE = 0.75 V). The $HESO_x$-550/OLC_{AT} battery remains stable for up to 68 h and deteriorates

until it reaches a stable ΔE of 1.04 V. This ΔE is maintained from the 88th h till the 316th h of cycling. Although the battery quickly deteriorates, good stability is maintained as cycling continues. **Figure S11** in the supporting documents shows the zinc plate before and after cycling the $HESO_x$-550/OLC_{AT} at 10 mA cm^{-2} for 316 hours. Most of the zinc was consumed and clear deposition on the zinc plate was observed. The Pt/C-IrO_2 battery dies after 175 h proving the instability of the catalyst. The durability of $HESO_x$-550/OLC_{AT} in rechargeable zinc-air batteries is owed to the increased oxygen vacancies which stabilize the crystal structure of the catalyst.

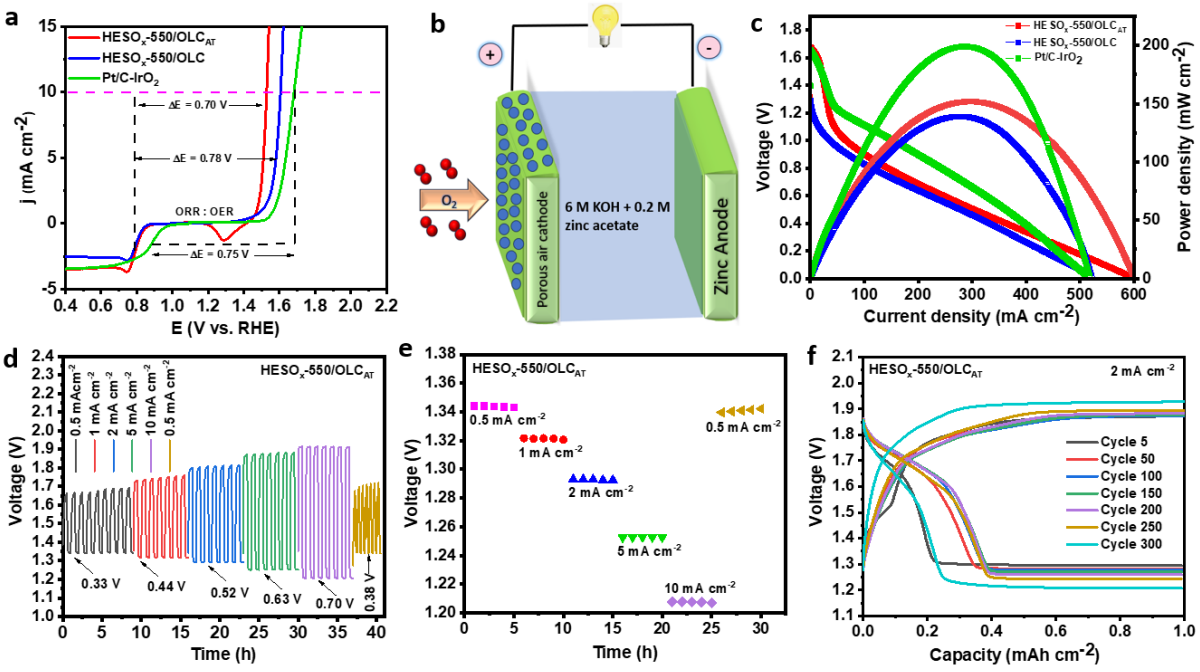

Figure 4. 8: (a) ORR/OER bifunctional curves. (b) Schematic representation of the zinc-air battery (c) The power density comparison between HESOx-550/OLC_{AT}, HESOx-550/OLC and Pt/C-IrO_2. (d) $HESO_x$-550/OLC_{AT} voltage gaps (ΔE) at different current densities (e) $HESO_x$-550/OLC_{AT} discharge curves at different current densities (f) Capacity curves at different cycles for the $HESO_x$-550/OLC_{AT} at 2 mA cm^{-2}.

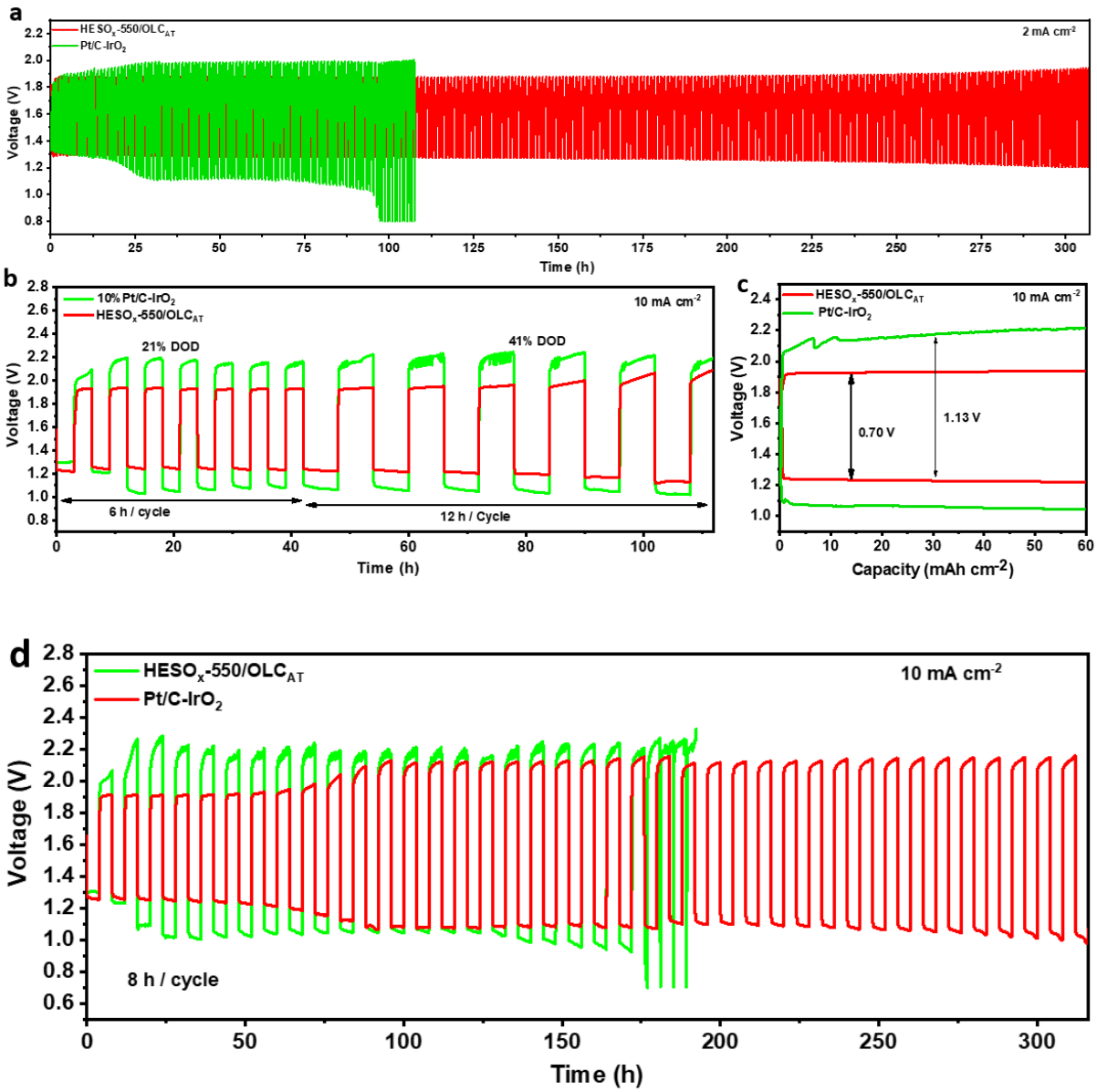

Figure 4. 9: (a) Discharge-Charge curves at 1 h per cycle. (b) The cycling performances for $HESO_x$-550/OLC_{AT} and Pt/C-IrO_2 under harsh DOD conditions (c) The discharge-charge capacity curves during deep discharging and charging conditions (6 h discharge and 6 h charge). (d) Continuous discharge-charge profiles for $HESO_x$-550/OLC_{AT} and Pt/C-IrO_2.

4.4. Summary

Highly efficient acid-treated high entropy spinel oxides supported on onion-like carbon as the favourable electrocatalysts for zinc-air batteries were successfully synthesized and tested for ORR/OER activity. The acid treatment introduced defects on the catalyst and exposed

$(CoCuFeMnNi)_3O_4$ which uniformly anchored on the carbon support. The introduced defects improved the electrocatalytic activity of the catalyst and a small ΔE of 0.70 V was achieved. Due to the exceptional bifunctionality of $HESO_x$-550/OLC_{AT}, the catalyst was further applied in RZABs and exhibited superior power density (154.3 mW cm^{-2}) and rate capability, excellent stability under shallow and harsh cycling conditions. The highest achieved areal energy density was 73.2 mWh cm^{-2} which is higher than most catalysts reported in the literature therefore this catalyst stands a chance in real-world device applications.

4.5. References

(1) Liu, J. N.; Zhao, C. X.; Wang, J.; Ren, D.; Li, B. Q.; Zhang, Q. A Brief History of Zinc-Air Batteries: 140 Years of Epic Adventures. Energy and Environmental Science. Royal Society of Chemistry September 26, 2022, pp 4542–4553. https://doi.org/10.1039/d2ee02440c.

(2) Li, Y.; Gong, M.; Liang, Y.; Feng, J.; Kim, J. E.; Wang, H.; Hong, G.; Zhang, B.; Dai, H. Advanced Zinc-Air Batteries Based on High-Performance Hybrid Electrocatalysts. Nat Commun 2013, 4. https://doi.org/10.1038/ncomms2812.

(3) Amiinu, I. S.; Liu, X.; Pu, Z.; Li, W.; Li, Q.; Zhang, J.; Tang, H.; Zhang, H.; Mu, S. From 3D ZIF Nanocrystals to Co–Nx/C Nanorod Array Electrocatalysts for ORR, OER, and Zn–Air Batteries. Adv Funct Mater 2018, 28 (5). https://doi.org/10.1002/adfm.201704638.

(4) Liu, W.; Niu, X.; Feng, J.; Yin, R.; Ma, S.; Que, W.; Dai, J.; Tang, J.; Wu, F.; Shi, W.; Liu, X.; Cao, X. Tunable Heterogeneous FeCo Alloy-Mo0.82N Bifunctional Electrocatalysts for Temperature-Adapted Zn-Air Batteries. ACS Appl Mater Interfaces 2023, 15 (12), 15344–15352. https://doi.org/10.1021/acsami.2c21616.

(5) Pitike, K. C.; Kc, S.; Eisenbach, M.; Bridges, C. A.; Cooper, V. R. Predicting the Phase Stability of Multicomponent High-Entropy Compounds. Chemistry of Materials 2020, 32 (17), 7507–7515. https://doi.org/10.1021/acs.chemmater.0c02702.

(6) Gayen, P.; Saha, S.; Bhattacharyya, K.; Ramani, V. K. Oxidation State and Oxygen-Vacancy-Induced Work Function Controls Bifunctional Oxygen Electrocatalytic Activity. ACS Catal 2020, 10 (14), 7734–7746. https://doi.org/10.1021/acscatal.0c01541.

(7) Choudhury, S.; Srimuk, P.; Raju, K.; Tolosa, A.; Fleischmann, S.; Zeiger, M.; Ozoemena, K. I.; Borchardt, L.; Presser, V. Carbon Onion/Sulfur Hybrid Cathodes: Via

Inverse Vulcanization for Lithium-Sulfur Batteries. Sustain Energy Fuels 2018, 2 (1), 133–146. https://doi.org/10.1039/c7se00452d.

(8) Parker, J. F.; Ko, J. S.; Rolison, D. R.; Long, J. W. Translating Materials-Level Performance into Device-Relevant Metrics for Zinc-Based Batteries. Joule. Cell Press December 19, 2018, pp 2519–2527. https://doi.org/10.1016/j.joule.2018.11.007.

(9) Wang, Y.; Li, H.; Liu, H.; Yang, L.; Zeng, C. Preparation and Formation Mechanism of Cr-Free Spinel-Structured High Entropy Oxide (MnFeCoNiCu)3O4. Ceram Int 2023, 49 (2), 1940–1946. https://doi.org/10.1016/j.ceramint.2022.09.159.

(10) Li, J.; Wang, N.; Deng, J.; Qian, W.; Chu, W. Flexible Metal-Templated Fabrication of Mesoporous Onion-like Carbon and Fe2O3@N-Doped Carbon Foam for Electrochemical Energy Storage. J Mater Chem A Mater 2018, 6 (27), 13012–13020. https://doi.org/10.1039/c8ta02417k.

(11) Portet, C.; Yushin, G.; Gogotsi, Y. Electrochemical Performance of Carbon Onions, Nanodiamonds, Carbon Black and Multiwalled Nanotubes in Electrical Double Layer Capacitors. Carbon N Y 2007, 45 (13), 2511–2518. https://doi.org/10.1016/j.carbon.2007.08.024.

(12) Kim, S.-G.; Park, O.-K.; Lee, J. H.; Ku, B.-C. Layer-by-Layer Assembled Graphene Oxide Films and Barrier Properties of Thermally Reduced Graphene Oxide Membranes. Carbon letters 2013, 14 (4), 247–250. https://doi.org/10.5714/cl.2013.14.4.247.

(13) Danyang, L.; Liping, S.; Qiang, L.; Tian, X.; Lihua, H.; Hui, Z. High-Entropy Oxide (Fe0.2Zn0.2Co0.2Ni0.2Cu0.2)Fe2O4: An Efficient and Stable Spinel-Type Electrocatalyst for H2O2 Production in Alkaline Media. J Alloys Compd 2022, 913. https://doi.org/10.1016/j.jallcom.2022.165148.

(14) Wang, B.; Yao, J.; Wang, J.; Chang, A. Spinel-Type High-Entropy (Co0.2Mn0.2Fe0.2Zn0.2Ti0.2)3O4 Oxides Constructed from Disordered Cations and Oxygen Vacancies. Journal of Alloys and Compounds. Elsevier Ltd March 15, 2022. https://doi.org/10.1016/j.jallcom.2021.163188.

(15) Tatar, D.; Ullah, H.; Yadav, M.; Kojčinović, J.; Šarić, S.; Szenti, I.; Skalar, T.; Finšgar, M.; Tian, M.; Kukovecz, Á.; Kónya, Z.; Sápi, A.; Djerdj, I. High-Entropy Oxides: A New Frontier in Photocatalytic CO2 Hydrogenation. ACS Applied Materials and Interfaces 2024, 16 (23), 29946–29962. https://doi.org/10.1021/acsami.4c00478.

(16) Farivar, F.; Lay Yap, P.; Karunagaran, R. U.; Losic, D. Thermogravimetric Analysis (TGA) of Graphene Materials: Effect of Particle Size of Graphene, Graphene Oxide and Graphite on Thermal Parameters. C (Basel) 2021, 7 (2), 41. https://doi.org/10.3390/c7020041.

(17) Lu, H.; Liu, Z.; Yan, X.; Li, D.; Parent, L.; Tian, H. Electron Work Function-a Promising Guiding Parameter for Material Design. Sci Rep 2016, 6. https://doi.org/10.1038/srep24366.

(18) Liu, W.; Zhang, Y.; Wang, S.; Bai, L.; Deng, Y.; Tao, J. Effect of Pore Size Distribution and Amination on Adsorption Capacities of Polymeric Adsorbents. Molecules 2021, 26 (17). https://doi.org/10.3390/molecules26175267.

(19) Chang, B.; Ai, Z.; Shi, D.; Zhong, Y.; Zhang, K.; Shao, Y.; Zhang, L.; Shen, J.; Wu, Y.; Hao, X. P-n Tungsten Oxide Homojunctions for Vis-NIR Light-Enhanced Electrocatalytic Hydrogen Evolution. J Mater Chem A Mater 2019, 7 (33), 19573–19580. https://doi.org/10.1039/c9ta06589j.

(20) Daiyan, R.; Saputera, W. H.; Zhang, Q.; Lovell, E.; Lim, S.; Ng, Y. H.; Lu, X.; Amal, R. 3D Heterostructured Copper Electrode for Conversion of Carbon Dioxide to Alcohols at Low Overpotentials. Adv Sustain Syst 2019, 3 (1). https://doi.org/10.1002/adsu.201800064.

(21) Liu, D.; Zhang, J.; Liu, D.; Li, T.; Yan, Y.; Wei, X.; Yang, Y.; Yan, S.; Zou, Z. N-Doped Graphene-Coated Commercial Pt/C Catalysts toward High-Stability and Antipoisoning in Oxygen Reduction Reaction. Journal of Physical Chemistry Letters 2022, 13 (8), 2019–2026. https://doi.org/10.1021/acs.jpclett.1c04005.

(22) Zhao, J.; Fu, C.; Ye, K.; Liang, Z.; Jiang, F.; Shen, S.; Zhao, X.; Ma, L.; Shadike, Z.; Wang, X.; Zhang, J.; Jiang, K. Manipulating the Oxygen Reduction Reaction Pathway on Pt-Coordinated Motifs. Nat Commun 2022, 13 (1). https://doi.org/10.1038/s41467-022-28346-0.

(23) Zhu, X.; Tan, X.; Wu, K. H.; Haw, S. C.; Pao, C. W.; Su, B. J.; Jiang, J.; Smith, S. C.; Chen, J. M.; Amal, R.; Lu, X. Intrinsic ORR Activity Enhancement of Pt Atomic Sites by Engineering the D-Band Center via Local Coordination Tuning. Angewandte Chemie - International Edition 2021, 60 (40), 21911–21917. https://doi.org/10.1002/anie.202107790.

(24) Yu, T.; Zhang, Y.; Hu, Y.; Hu, K.; Lin, X.; Xie, G.; Liu, X.; Reddy, K. M.; Ito, Y.; Qiu, H. J. Twelve-Component Free-Standing Nanoporous High-Entropy Alloys for Multifunctional Electrocatalysis. ACS Mater Lett 2022, 4 (1), 181–189. https://doi.org/10.1021/acsmaterialslett.1c00762.

(25) He, R.; Yang, L.; Zhang, Y.; Wang, X.; Lee, S.; Zhang, T.; Li, L.; Liang, Z.; Chen, J.; Li, J.; Ostovari Moghaddam, A.; Llorca, J.; Ibáñez, M.; Arbiol, J.; Xu, Y.; Cabot, A. A CrMnFeCoNi High Entropy Alloy Boosting Oxygen Evolution/Reduction Reactions and Zinc-Air Battery Performance. Energy Storage Mater 2023, 58, 287–298. https://doi.org/10.1016/j.ensm.2023.03.022.

(26) Li, C.; Baek, J. B. Recent Advances in Noble Metal (Pt, Ru, and Ir)-Based Electrocatalysts for Efficient Hydrogen Evolution Reaction. ACS Omega. American Chemical Society January 14, 2020, pp 31–40. https://doi.org/10.1021/acsomega.9b03550.

(27) Bhalothia, D.; Krishnia, L.; Yang, S. S.; Yan, C.; Hsiung, W. H.; Wang, K. W.; Chen, T. Y. Recent Advancements and Future Prospects of Noble Metal-Based Heterogeneous Nanocatalysts for Oxygen Reduction and Hydrogen Evolution Reactions. Applied Sciences (Switzerland). MDPI AG November 1, 2020, pp 1–19. https://doi.org/10.3390/app10217708.

(28) Wang, C.; An, C.; Qin, C.; Gomaa, H.; Deng, Q.; Wu, S.; Hu, N. Noble Metal-Based Catalysts with Core-Shell Structure for Oxygen Reduction Reaction: Progress and Prospective. Nanomaterials. MDPI July 1, 2022. https://doi.org/10.3390/nano12142480.

(29) Chen, S.; Xu, J.; Chen, J.; Yao, Y.; Wang, Z.; Li, P.; Li, Y.; Wang, F. Ru Doping Induced Interface Engineering in Flower-Liked CoMoO4-RuO2 Boosts Oxygen Electrocatalysis for Rechargeable Zn-Air Battery. J Colloid Interface Sci 2024, 658, 230–237. https://doi.org/10.1016/j.jcis.2023.12.066.

(30) Liu, Q.; Wang, Y.; Dai, L.; Yao, J. Scalable Fabrication of Nanoporous Carbon Fiber Films as Bifunctional Catalytic Electrodes for Flexible Zn-Air Batteries. Advanced Materials 2016, 28 (15), 3000–3006. https://doi.org/10.1002/adma.201506112.

(31) Hopkins, B. J.; Chervin, C. N.; Parker, J. F.; Long, J. W.; Rolison, D. R. An Areal-Energy Standard to Validate Air-Breathing Electrodes for Rechargeable Zinc–Air Batteries. Advanced Energy Materials. Wiley-VCH Verlag August 1, 2020. https://doi.org/10.1002/aenm.202001287.

(32) Zhang, J.; Zhou, Q.; Tang, Y.; Zhang, L.; Li, Y. Zinc-Air Batteries: Are They Ready for Prime Time? Chem Sci 2019, 10 (39), 8924–8929. https://doi.org/10.1039/c9sc04221k.

Chapter 5

Hybrid FeCo-Fe_2CoO_4/C bifunctional electrocatalysts for high-performance rechargeable zinc-air batteries.

5.1. Introduction

The global energy crisis has raised concerns for decades thus the development of green and sustainable energy sources is paramount. Existing sustainable energy sources such as solar and wind were proposed to tackle severe environmental issues related to the use of fossil fuels, however, these are intermittent since they are weather dependent [1]. The development of electrochemical energy storage devices is considered the most promising strategy for tackling the global energy crisis [2],[3]. Supercapacitors, lithium-ion and metal-air batteries are the most common electrochemical energy storage devices [4],[5].

Batteries have attracted great attention as the most favoured electrochemical energy storage devices because of their large-scale storage [6]. Oxygen chemistry plays an essential role in the operation of devices such as metal-air batteries [4]. Particularly stable and effective electrocatalysts in the cathode are required for the operation of the devices to overcome the energy barrier involved in breaking the multiple bonded oxygen [7],[8]. However, due to poor kinetics encountered during electrocatalysis reactions, there is a technological barrier to the wide range application of this technology.

Rechargeable Zn-air batteries are amongst the most promising electrochemical energy storage devices because of their cost-effectiveness, abundance of raw materials, environmental friendliness, and high specific energy [9],[2],[10]. During the operation of RZABs, zinc is oxidised at the anode in the presence of an electrolyte to release zinc oxide, water and two electrons [3]. The key cathodic processes involved in the discharge-charge of a rechargeable

Zn-air battery are oxygen reduction/evolution reactions [9],[4],[3]. The reactions occur in an alkaline solution.

The sluggish kinetics during ORR and OER have limited the overall efficiency of the Zinc-air batteries. Therefore, there is a need for an efficient bifunctional electrocatalyst to enhance ORR and OER in the air cathode [11]. Noble metals (e.g. Pt, Pd) and noble metal-oxides (e.g RuO_2, IrO_2) are commonly applied as catalysts for ORR and OER but they have rare sources, high cost, and poor stability and they are unable to successfully promote both reactions [4],[9]. The use of non-precious metal-based electrocatalysts with great efficiency and cost-effectiveness has risen to mitigate problems that occur whenever noble precious-metal-based electrocatalysts are used. Transition metal-based oxides and alloys have been widely employed since they are abundant in nature and show improved kinetics in electrocatalysis [2],[11]. Bimetallic electrocatalysts offer an inherent polarization between two different metals which enhance the transfer of charge and greatly stimulate the catalytic activity.

In this study, a hybrid of FeCo alloy and oxide (FeCo-Fe_2CoO_4/C) was synthesized using $FeCl_2$, $CoCl_2.6H_2O$ and Vulcan carbon as precursors. The material was then modified by annealing followed by microwaving to give two samples (the annealed and microwave sample) which were investigated for ORR and OER performance in an alkaline electrolyte. The best performing sample was further tested for applicability in rechargeable zinc-air batteries.

5.2. Experimental

5.2.1. Chemicals and materials

Iron (ii) chloride ($FeCl_2$), cobalt (ii) chloride hexahydrate ($CoCl_2.6H_2O$), platinum on carbon (Pt/C), Iridium oxide (IrO_2), ethylene glycol ($HOCH_2CH_2OH$), Polyvinylpyrrolidone ($(C_6H_9NO)_n$) and nafion were purchased from Sigma Aldrich.

5.2.2. Synthesis of Fe_2CoO_4-FeCo/C

The FeCo-Fe_2CoO_4/C catalysts were prepared by a simple reduction method [12]. Briefly, solutions of 114 mg $FeCl_2$ and 101 mg $CoCl_2.6H_2O$ were prepared in 10 mL distilled water and stirred for 20 min. Under vigorous stirring $FeCl_2$ solution was slowly added to $CoCl_2.6H_2O$ solution and the mixture was allowed to stir for 20 min after which 175 mg of Vulcan carbon support was dispersed. Following ultrasonication for 30 min, the suspensions were heated with constant magnetic stirring until the solvent evaporation was completed to obtain a dense, thick slurry. This slurry was then oven-dried at 60 ℃ and ground into a fine dark powder. Under the flowing Ar/H_2 atmosphere, the powder was heated for 2 h at 300 ℃, annealed for 2 h at 500 ℃ in a tube furnace, and then cooled to room temperature. The annealed product (FeCo-Fe_2CoO_4/C_{Ann}) was then separated into two parts, one was left annealed then the other was microwaved. For microwaving, ethylene glycol was added to the FeCo-Fe_2CoO_4/C_{Ann} powder and the solution was stirred for 30 min. The addition of 32.1 mg Polyvinylpyrrolidone (PVP) was followed by continuous stirring for 20 min. The solution was then subjected to rapid microwave irradiation at 600 W for 15 min. Once the black powders reached room temperature, they were centrifuged five times with acetone and five times with water, respectively, to eliminate any remains of ethylene glycol and other impurities. After oven drying overnight at 100 ℃, the FeCo-Fe_2CoO_4/C_{MW} was ground into a fine dark powder. The procedure is summarized in **scheme 5.1** below.

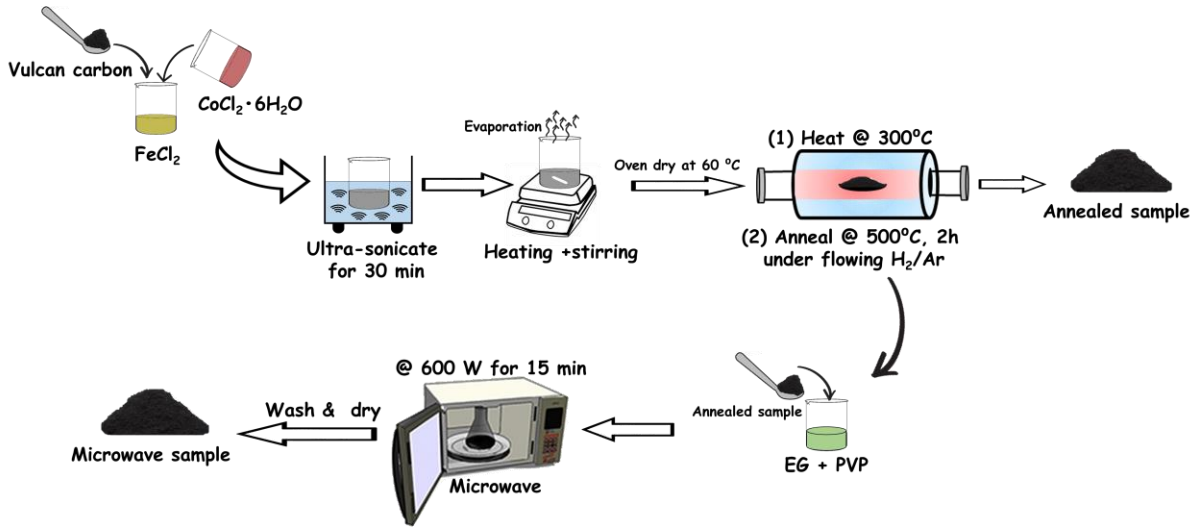

Scheme 5. 1: The schematic representation for the synthesis of FeCo-Fe_2CoO_4/C catalysts.

5.2.3. Physical characterization

Transmission electron microscopy (TEM) was used to examine the morphologies of the obtained samples. X-ray diffraction (XRD, Bruker D2 phaser) was used to determine the crystallinity and purity of the samples. X-ray photoelectron spectroscopy (XPS) characterized their chemical composition. Nitrogen adsorption-desorption (Brunauer-Emmet-Teller, BET) was used to determine the electrocatalysts' surface area and pore volume. To investigate the thermal stability of the electrocatalysts, Thermogravimetric analysis (TGA) was used. TGA 4000-Perkim Elmer at a heating rate of 10°C /min, under airflow (20ml/min, 4 bar) from 35-900 ℃ was used.

5.2.4. Electrochemical measurements

The electrochemical measurements were carried out with a three-electrode system at room temperature using the Biologic SP300 potentiostat powered by EC lab. The glassy carbon electrode modified with the catalyst was used as the working electrode, Ag/AgCl filled with saturated 3 M KCl solution as the reference electrode and the Pt rod as the counter electrode.

The catalyst ink was prepared by adding 950 µL of ethanol and 50 µL of Nafion to 10 mg of the catalyst. The mixture was sonicated for 2 h to form a homogeneous catalyst ink. Before drop casting, the glassy carbon electrode was polished with an alumna slurry and washed with ultra-pure water. 30 µL of ink was drop cast on the GC and allowed to dry before running the electrochemical measurements.

Both OER and ORR were performed in 1 M KOH solution saturated with O_2. A scan rate of 10 mV/s was used for linear sweep voltammetry (LSV) measurements. Calibration of all potentials was done using the reversible hydrogen electrode (RHE) which is as follows:

$E_{RHE} = E_{Ag/AgCl} + 0.059pH + 0.197$

The electron transfer number was calculated using the Koutecky-Levich (KL) equation:

$$\frac{1}{j} = \frac{1}{j_k} + \left(\frac{1}{0.62nFD^{\frac{2}{3}}\upsilon^{-\frac{1}{6}}C}\right)\omega^{-\frac{1}{2}}$$

Where j is the current density, j_k is the kinetic current density, n is the number of electrons, F is the Faraday constant (96 485.3321 C/mol), D is the diffusion coefficient of O_2 ($1.93 \times 10^{-5} cm^2 s^{-1}$), υ is the viscosity of the solution ($1.009 \times 10^{-2} cm^2 s^{-1}$), C_{O_2} is the concentration of oxygen dissolved in solution ($1.26 \times 10^{-3} mol L^{-1}$) and ω is the rotation speed [13], [14].

5.2.5. Zinc-air battery assembling and testing

The zinc-air battery was assembled using the zinc plate with 0.25 mm thickness as the anode, 0.2 M zinc acetate dissolved in 6 M KOH as the electrolyte and carbon paper coated with the electrocatalyst (loading ~10 mg/cm^2). The tests were carried out using the Biologic battery tester. The Pt/C-IrO_2 was assembled using the 1:1 catalyst ratio for comparison.

The specific capacity was calculated using the formula:

Specific capacity = $\frac{Discharge\ current \times discharge\ time}{the\ mass\ of\ Zn\ consumed}$

5.3. Results and discussion

5.3.1. Physical Characterizations

The XRD patterns for the FeCo-Fe_2CoO_4/C electrocatalysts are shown in **Figure 5.1 (a)**. FeCo alloy (PDF 00-049-1568) and Fe_2CoO_4 oxide (PDF 01-079-7693) diffraction peaks were observed simultaneously in the XRD patterns, concluding the successful synthesis of the hybrid oxide and alloy. In both FeCo-Fe_2CoO_4/C_{Ann} and FeCo-Fe_2CoO_4/C_{MW}, typical peaks of the FeCo alloy phase were observed at 44.8°, 65.5° and 82.8° corresponding to crystal planes (110), (200) and (211) respectively [15]. The remaining peaks can be attributed to Fe_2CoO_4 formed when Fe^{2+} was oxidised to Fe^{3+} and combined with Co^{2+} during the reaction to form cobalt ferrite [16]. The iron-cobalt oxide (Fe_2CoO_4) crystal planes are (220), (311), (400), (440), (422), (511) and (440) which appear at 30.1°,35.5°,43.0°, 53.4°, 56.6° and 62.5° respectively. These peaks are synonymous with a typical spinel structure with $Fd\bar{3}m$ space group symmetry [17]. There are no obvious differences in the XRD patterns (miller indices are the same) for FeCo-Fe_2CoO_4/C_{Ann} and FeCo-Fe_2CoO_4/C_{MW} however FeCo-Fe_2CoO_4/C_{Ann} has broader peaks than FeCo-Fe_2CoO_4/C_{MW}. **Figure 5.1. (b) & (c)** show the fitted (311) and (110) peaks respectively for both samples. It is observed that for the (311) peak, FeCo-Fe_2CoO_4/C_{Ann} has an FWHM value of 0.375° which is higher than that of FeCo-Fe_2CoO_4/C_{MW} (0.303°). The values are 0.506° and 0.467° for FeCo-Fe_2CoO_4/C_{Ann} and FeCo-Fe_2CoO_4/C_{MW} respectively in the (110) peak. When the FWHM is smaller, the crystal structure is more perfect, while a larger number indicates there are imperfections or defects in the lattice of the crystal. The average crystallite sizes were calculated from the predominant (311) and (110) peaks using the Debye-Scherrer equation [18].

$$D = \frac{0.94\lambda}{B cos\theta}$$

D is the crystallite size, λ is the x-ray wavelength (1.5408 Å), B is the FWHM and θ is the Bragg diffraction angle. The crystallite sizes for FeCo-Fe_2CoO_4/C_{Ann} and FeCo-Fe_2CoO_4/C_{MW} were found to be 143.6 nm and 177.8 nm for the (311) peak respectively. The sizes for the (110) were 106.4 nm and 115.3 nm for FeCo-Fe_2CoO_4/C_{Ann} and FeCo-Fe_2CoO_4/C_{MW} respectively. The different crystallite sizes in FeCo-Fe_2CoO_4/C_{Ann} and FeCo-Fe_2CoO_4/C_{MW} are attributed to the samples containing both the alloy and oxide. The (311) is attributed to Fe_2CoO_4 (oxide) while the (110) is attributed to FeCo (alloy). These values suggest that FeCo-Fe_2CoO_4/C_{Ann} has a smaller crystallite size than FeCo-Fe_2CoO_4/C_{MW}. Smaller crystallite size is associated with higher surface area leading to improved ORR/OER kinetics therefore FeCo-Fe_2CoO_4/C_{Ann} is expected to show better electrochemical performances [19]. Subjecting the sample to microwave irradiation increased the crystallite size of the catalyst which is undesirable.

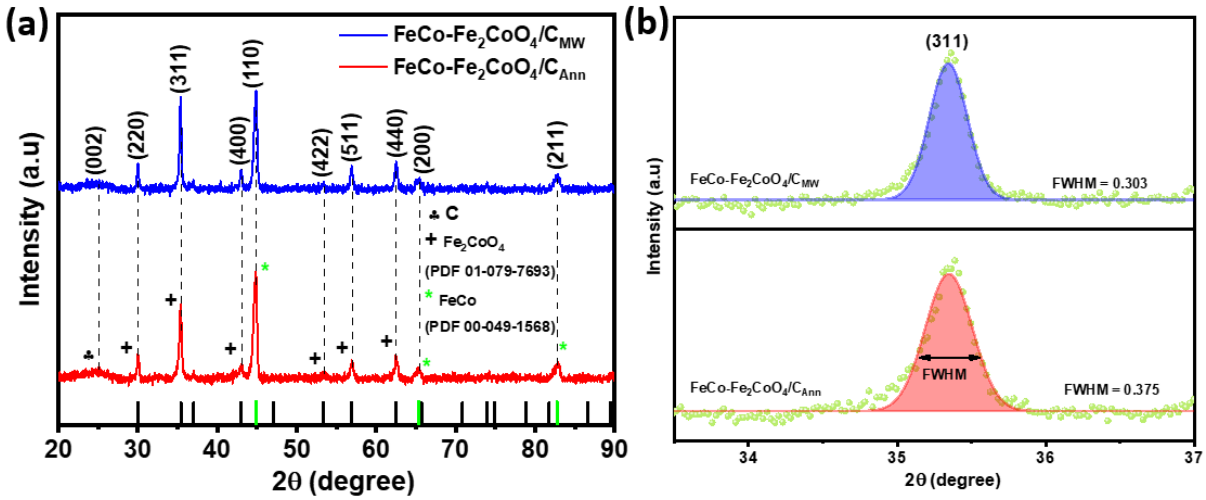

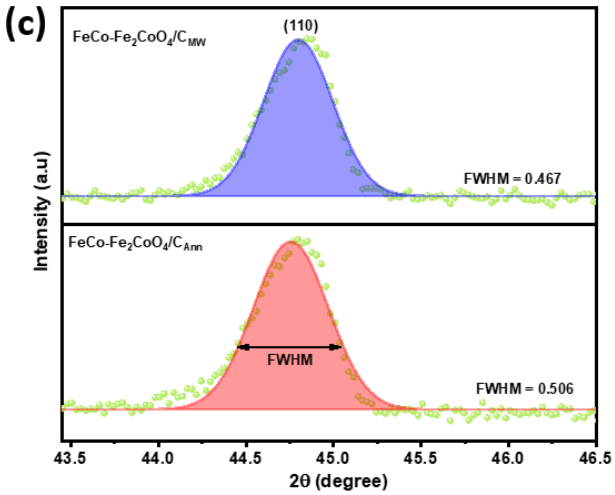

Figure 5. 1: (a) The XRD patterns for FeCo-Fe_2CoO_4/C_{Ann} and FeCo-Fe_2CoO_4/C_{MW}. The fitted (b) (311) peaks and (c) (110) peaks with FWHM values for FeCo-Fe_2CoO_4/C_{Ann} and FeCo-Fe_2CoO_4/C_{MW}.

The SEM images for FeCo-Fe_2CoO_4/C_{Ann} and FeCo-Fe_2CoO_4/C_{MW} are depicted in **Figure 5.2. (a) & (b)** respectively. The FeCo-Fe_2CoO_4 particles were identified and circled in the SEM images. The shape is nearly similar to that of iron-cobalt-based materials observed in the literature [20],[21]. The annealed FeCo-Fe_2CoO_4 shows smooth, regularly shaped particles while microwaved FeCo-Fe_2CoO_4 also has smooth particles however the shape is irregular. It is clear from the SEM images that microwaving the FeCo-Fe_2CoO_4/C_{Ann} sample destroyed the shape of the particles. The FeCo-Fe_2CoO_4 particles were supported on a porous carbon matrix which was identified as small, agglomerated particles which are dominant in the images. **Figure 5.2. (c) & (d)** shows the TEM images for FeCo-Fe_2CoO_4/C_{Ann} and FeCo-Fe_2CoO_4/C_{MW} respectively. The catalysts were suspended on Vulcan carbon supports. The Vulcan carbon can be seen as small sponge-like particles in both samples. The big and dark particles were identified as FeCo-Fe_2CoO_4. The annealed FeCo-Fe_2CoO_4 has cubic-like particles while microwaved FeCo-Fe_2CoO_4 has agglomerated particles with distorted irregular shapes. Particle agglomeration is unfavourable as it leads to loss of catalytic activity [22]. **Figures 5.2 (e-i) & (j-n)** show the EDS images for the FeCo-Fe_2CoO_4/C_{Ann} and FeCo-Fe_2CoO_4/C_{MW} respectively.

The Fe, Co and O are not well dispersed in the FeCo-Fe_2CoO_4/C_{Ann} however introducing microwave irradiation led to the homogeneous distribution of Fe, Co, and O in the FeCo-Fe_2CoO_4/C_{MW} sample. The PVP surfactant added during the synthesis of FeCo-Fe_2CoO_4/C_{MW} played a major role in dispersing the particles.

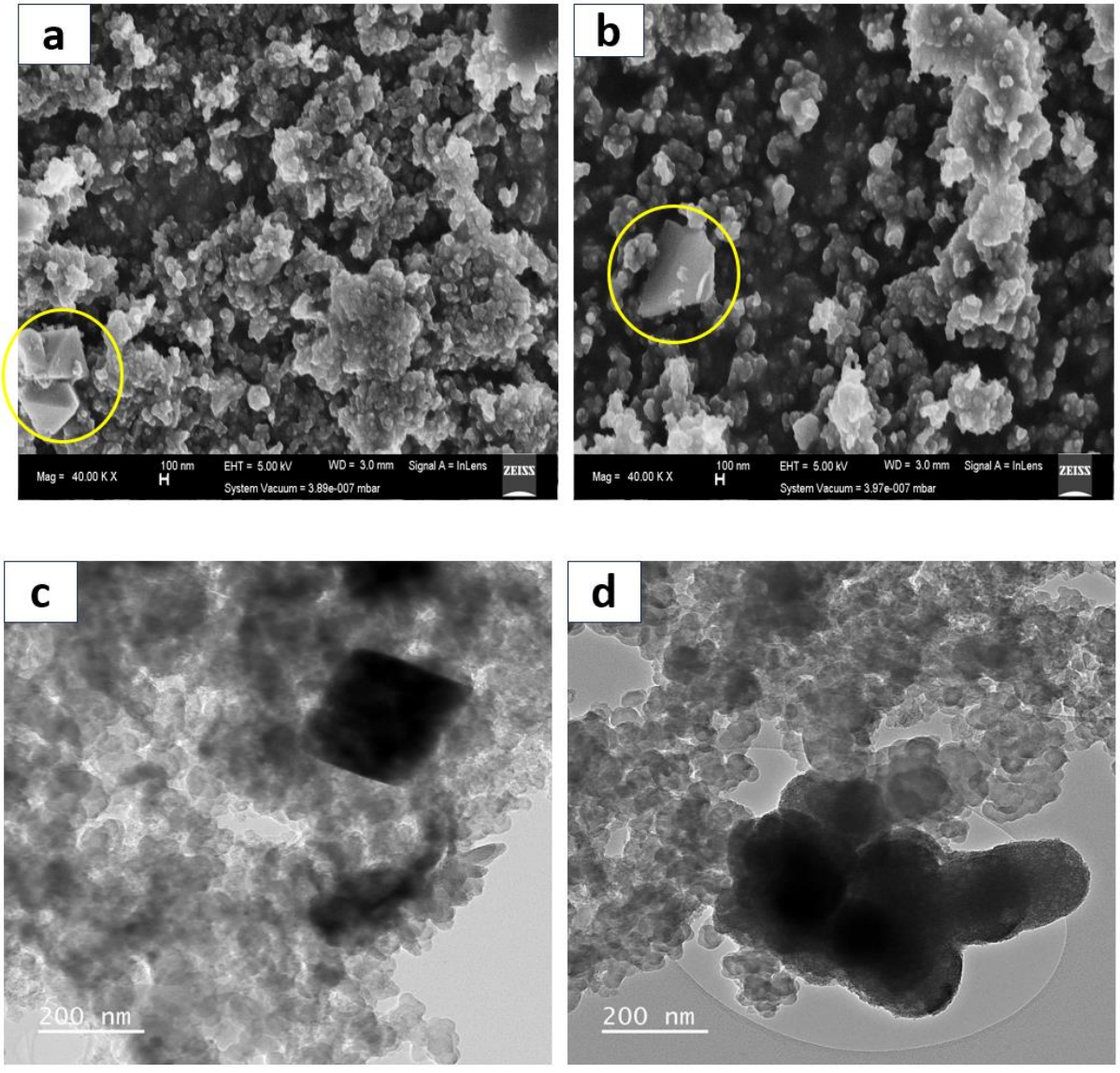

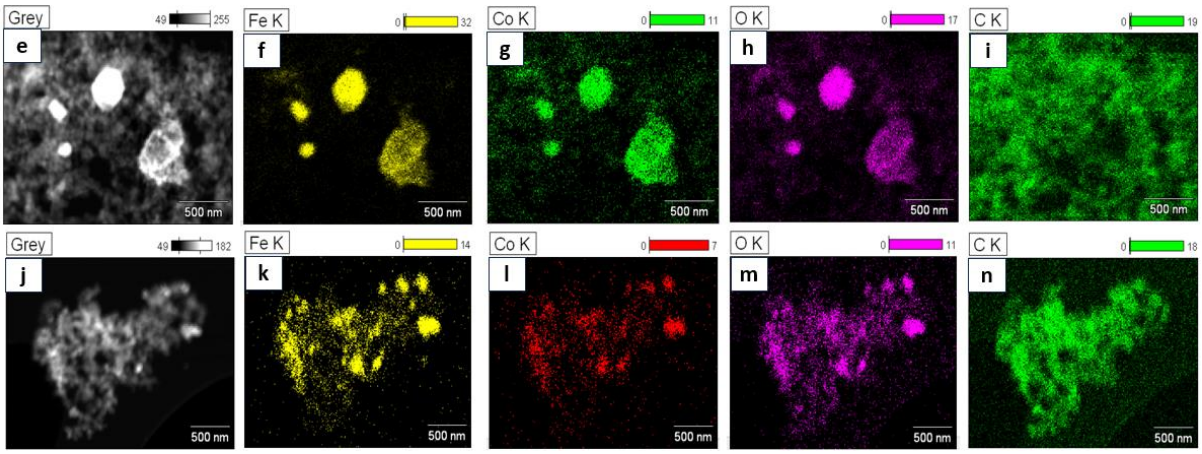

Figure 5. 2: SEM images for (a) FeCo-Fe_2CoO_4/C_{Ann} and (b) FeCo-Fe_2CoO_4/C_{MW}. TEM images for (c) FeCo-Fe_2CoO_4/C_{Ann} and (d) FeCo-Fe_2CoO_4/C_{MW}. EDS images for (e-i) FeCo-Fe_2CoO_4/C_{Ann} and (j-n) FeCo-Fe_2CoO_4/C_{MW}.

Figure 5.3. shows the survey scans (**Figure 5.3 (a)**) and high-resolution Fe 2P (**Figure 5.3 (b)**), Co 2P (**Figure 5.3 (c)**) and O 1s (**Figure 5.3 (d)**) XPS spectra for FeCo-Fe_2CoO_4/C_{Ann} and FeCo-Fe_2CoO_4/C_{MW}. The survey scans confirm the presence of Co, Fe, O, and C which agree with the EDS. However, FeCo-Fe_2CoO_4/C_{MW} has an additional element which is N. The surfactant PVP was identified as the source of N in FeCo-Fe_2CoO_4/C_{MW}. $2P_{3/2}$ and $2P_{1/2}$ doublets were observed for both Fe 2P and Co 2P which are due to spin-orbit coupling [23]. The Fe $2P_{3/2}$ verifies the presence of Fe^0, Fe^{2+} and Fe^{3+} with binding energies 707.8 V, 710.9 V and 713.4 V respectively for FeCo-Fe_2CoO_4/C_{Ann} [24]. The metallic Fe (zero-valent Fe) in the FeCo-Fe_2CoO_4/C_{Ann} is from the alloy component of the catalyst which is also observed in the XRD. The Co^0, Co^{2+} and Co^{3+} appear at 776.15 eV, 780.77 eV, and 783.69 eV respectively for the Co $2P_{3/2}$ in the FeCo-Fe_2CoO_4/C_{Ann} [25]. Both the Fe^0 and Co^0 peaks are not present in FeCo-Fe_2CoO_4/C_{MW} and this is due to the oxidation of FeCo to Fe_3O_4 and Co_3O_4 during microwaving in an open system. XPS analyses the surface composition of the samples therefore this implies that the metallic Fe and Co are not present on the FeCo-Fe_2CoO_4/C_{MW} surface however they are present in the bulk sample according to XRD (used for bulk sample analysis).

The O1s XPS shows three distinct peaks attributed to O_a, O_v and O_l (**Figure 5.3 (d)**). FeCo-Fe_2CoO_4/C_{MW} has a higher O_v percentage (62.2%) than FeCo-Fe_2CoO_4/C_{Ann} (49.5%). The O_v peak is associated with oxygen vacancies which are known to improve the conductivity, offer abundant reaction active sites and optimize the surface electrochemical structure [26]. The lower percentage of oxygen vacancies in FeCo-Fe_2CoO_4/C_{Ann} is attributed to the high alloy content in the sample which contains no oxygen therefore oxygen defects cannot be formed.

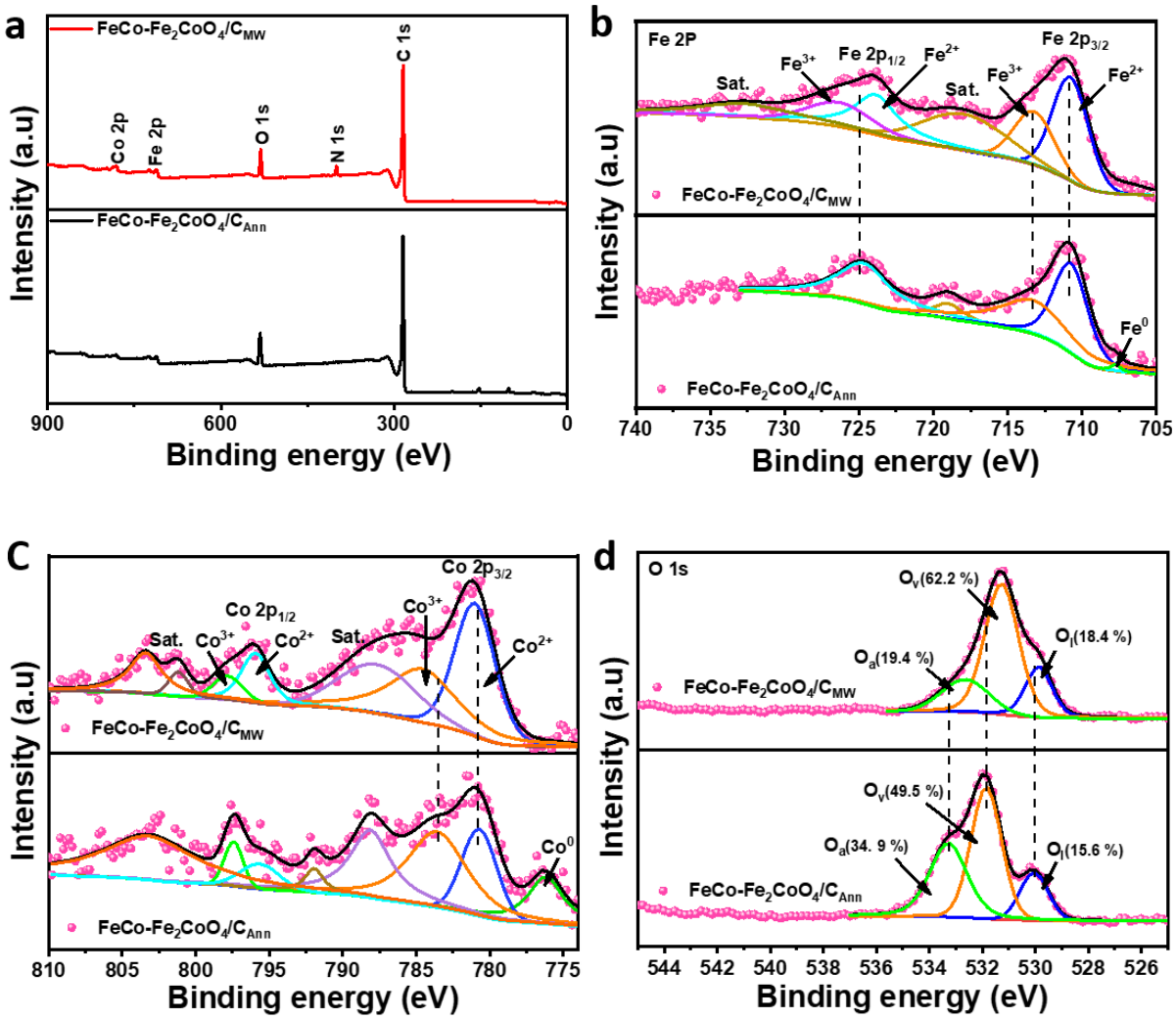

Figure 5. 3: XPS spectra of (a) survey scan (b) Fe 2P (c) Co 2P and (d) O1s for FeCo-Fe_2CoO_4/C_{Ann} and FeCo-Fe_2CoO_4/C_{MW}.

Figure 5.4. shows the TGA and derivative curves for the FeCo-Fe_2CoO_4/C samples heated in air. The initial weight loss between 100 ℃ and 150 ℃ observed in **Figure 5.4. (a)** for the FeCo-

Fe_2CoO_4/C_{Ann} sample is a common phenomenon in nanocarbon material, and it is attributed to the evaporation of the physically adsorbed water [27]. The water evaporation peak is observed at 130.0 ℃ in the DTG curve (**Figure 5.4 (b)**). With an assumption that all the carbon has been burned out, the amount of Fe_2CoO_4 remaining in the annealed sample is 33.1wt% which is higher than that in the microwave sample (24.4wt%). During heating, the FeCo component was concerted to Fe_3O_4 and Co_3O_4 [28]. Microwaving the sample greatly reduced the FeCo-Fe_2CoO_4 content thus decreasing the catalytic activity of FeCo-Fe_2CoO_4/C_{MW}.

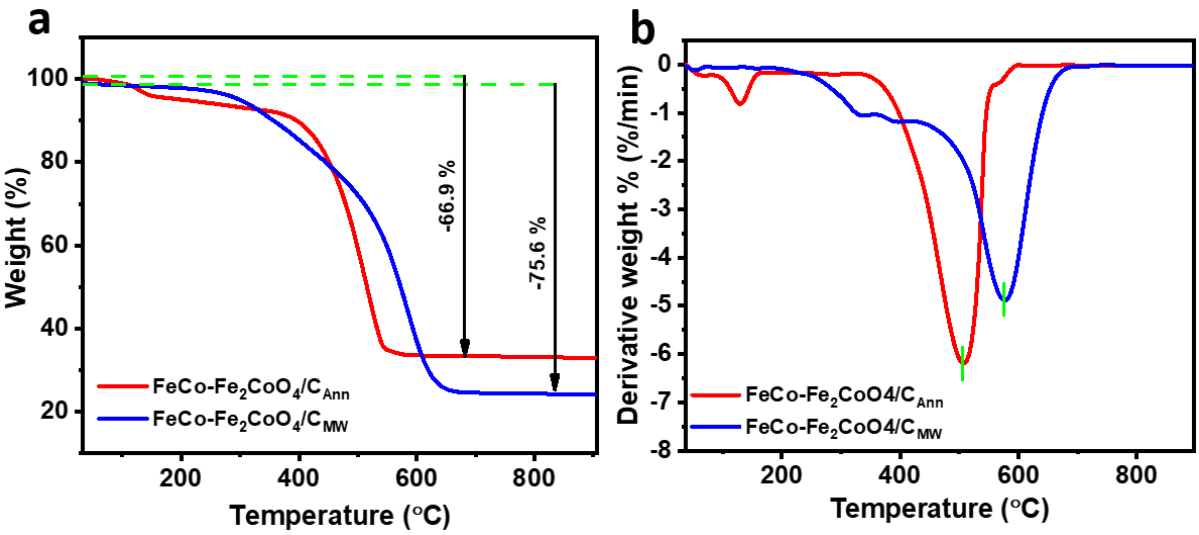

Figure 5. 4: (a) TGA and (b) DTG profiles for FeCo-Fe_2CoO_4/C electrocatalysts burnt in air.

Figure 5.5 shows the Raman spectra of the FeCo-Fe_2CoO_4/C catalysts and the deconvoluted Raman modes. Four Raman modes, that is $A_{1g} + E_g + 2F_{2g}$ were observed for FeCo-Fe_2CoO_4/C samples and are similar to that of ferrite in a spinel structure at ambient conditions. The modes below 600 cm^{-1} are linked to the motion of oxygen atoms in octahedral BO_6 and those above 600 cm^{-1} are linked to the motion of oxygen atoms in the tetrahedral AO_4 group. F_{2g} (1) is due to the translational movement of four oxygen atoms along with a metal ion at the tetrahedral site. The E_g mode is due to the symmetric bending of oxygen regarding the metal ion. F_{2g} (2) is due to the asymmetric stretching of Fe (Ni) and O while the A_{1g} is a result of the symmetric stretching of oxygen atoms on Fe–O (and Ni–O) bonds in the tetrahedral sites [29]. The peaks

appear at 1350.7 cm^{-1} and 1593. cm^{-1} result from the D and G bands respectively. The D band signifies the degree of disorder while the G band is the descriptor of the graphitisation degree. FeCo-Fe_2CoO_4/C_{MW} has a slightly higher D/G ratio of 1.13 which is better than that of FeCo-Fe_2CoO_4/C_{Ann} (1.04). The D band arises from the defects and disorders in the carbon [30] therefore microwave irradiation introduced defects in the FeCo-Fe_2CoO_4/C_{MW} sample.

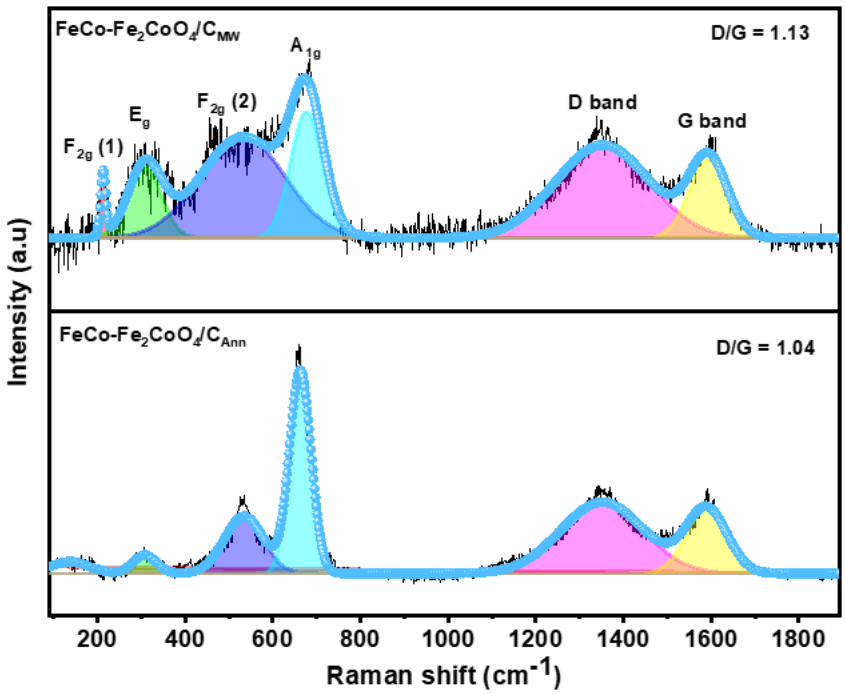

Figure 5. 5: The deconvoluted Raman modes for FeCo-Fe_2CoO_4/C_{Ann} and FeCo-Fe_2CoO_4/C_{MW}.

Catalysts often perform better when their specific surface areas are larger [31]. The FeCo-Fe_2CoO_4/C_{MW} has a surface area of 102.8 m^2/g and a pore volume of 0.4454 cm^3/g. These parameters are larger than those of FeCo-Fe_2CoO_4/C_{Ann} as listed in **Table 5.1**. Porous and high surface area structures are beneficial for electron transfer, mass exchange, and diffusion in electrocatalytic processes [32]. The increased BET surface can be attributed to the PVP added during microwaving. PVP is a large polymer therefore it has added to the surface area. The FWHM in the XRD was analysed for the (311) and (110) metal planes which implied a higher

surface area for FeCo-Fe_2CoO_4/C_{Ann} than for FeCo-Fe_2CoO_4/C_{MW}. This proves that the added BET surface area in FeCo-Fe_2CoO_4/C_{MW} is from the PVP.

Table 5. 1. BET textural properties analysis for the FeCo-Fe_2CoO_4/C electrocatalysts.

Catalyst	**BET parameters**		
	BET Surface Area (m^2/g)	Pore Volume (cm^3/g)	Pore diameter (nm)
FeCo-Fe_2CoO_4/C_{Ann}	90.49	0.4169	22.27
FeCo-Fe_2CoO_4/C_{MW}	102.8	0.4454	21.89

5.3.2. Electrochemical measurements

To test for the electrochemical performances of the FeCo-Fe_2CoO_4/C electrocatalysts, ORR was performed in 1 M KOH and Pt/C was included for comparison as shown in **Figure 5.6 (a)**. FeCo-Fe_2CoO_4/C_{Ann} has a larger half-wave potential ($E_{1/2}$) of 0.79 V compared to FeCo-Fe_2CoO_4/C_{MW} (0.74 V) suggesting better catalytic performance for FeCo-Fe_2CoO_4/C_{Ann} during ORR. Due to the noble nature of Pt, the $E_{1/2}$ for Pt/C is 0.93 V, and it surpasses that of the FeCo-Fe_2CoO_4/C electrocatalysts. The limiting current density for FeCo-Fe_2CoO_4/C_{MW} is 3.12 mA cm^{-2} which is higher than that of FeCo-Fe_2CoO_4/C_{Ann} (2.13 mA cm^{-2}). The improved limiting current in FeCo-Fe_2CoO_4/C_{MW} is attributed to the increased BET surface area and pore volume. The increased number of oxygen vacancies observed in the O1s XPS also led to the improved current response. **Figure 5.6 (b) & (d)** shows the ORR polarization curves for FeCo-Fe_2CoO_4/C_{Ann} and FeCo-Fe_2CoO_4/C_{MW} respectively at different rotation speeds. The current density increases with increasing rotation speed. **Figure 5.6 (c) & (e)** depict the Koutecky-Levich plots for FeCo-Fe_2CoO_4/C_{Ann} and FeCo-Fe_2CoO_4/C_{MW} respectively. The electron transfer numbers for both catalysts are less than 4 e^- suggesting a two-step pathway. This shows

that microwaving the sample did not change the reaction pathway (or electron transfer number) but only altered the limiting current, E_{onset} and $E_{1/2}$. The OER polarization curves are depicted in **Figure 5.6 (f)**. FeCo-Fe_2CoO_4/C_{Ann} has lower $E_{j=10}$ of 1.55 V compared to FeCo-Fe_2CoO_4/C_{MW} (1.58 V) and IrO_2 (1.68 V) suggesting better catalytic performance for OER. FeCo-Fe_2CoO_4/C_{MW} has a smaller tafel slope than FeCo-Fe_2CoO_4/C_{Ann} as illustrated in **Figure 5.6 (g)**.

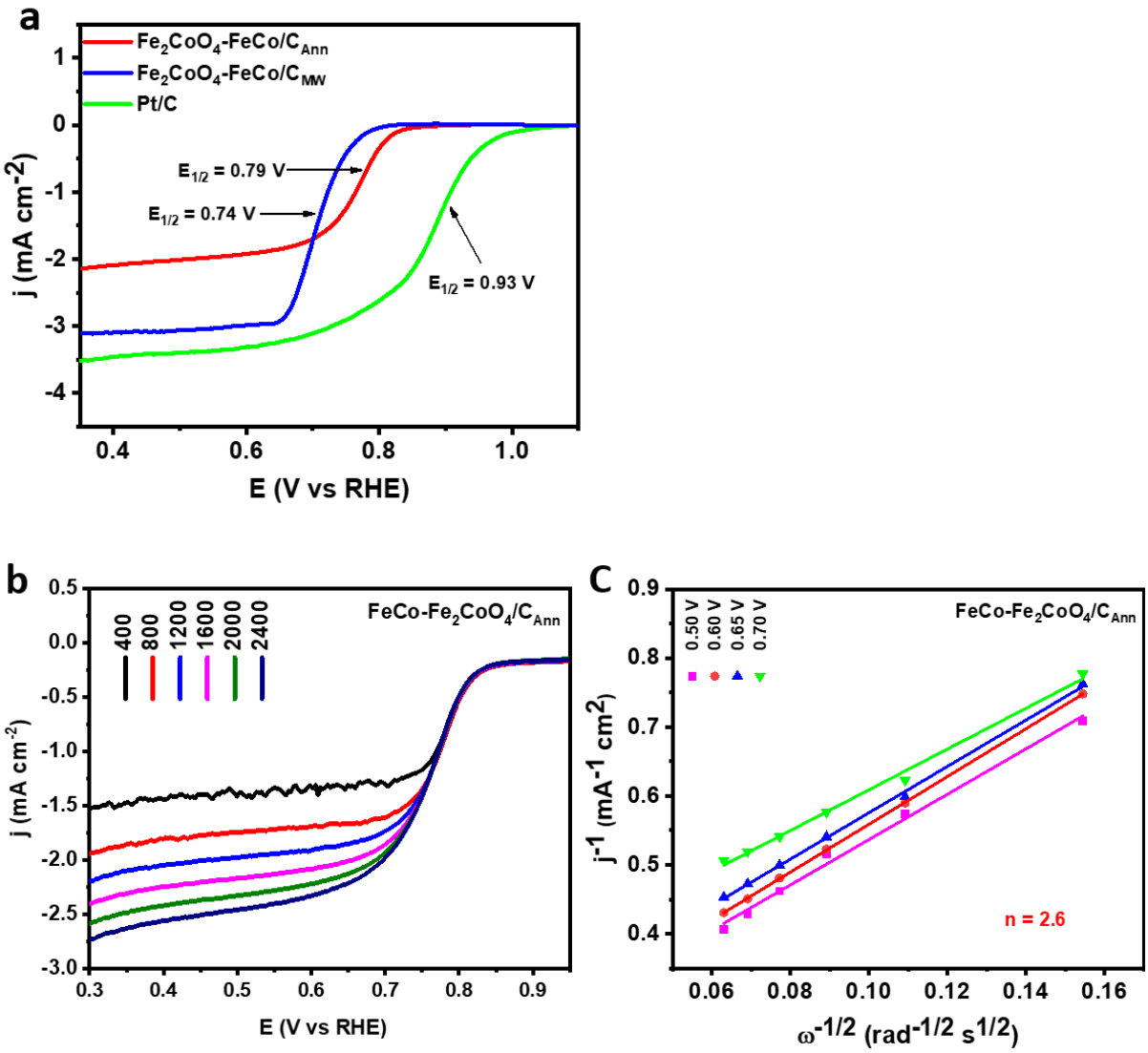

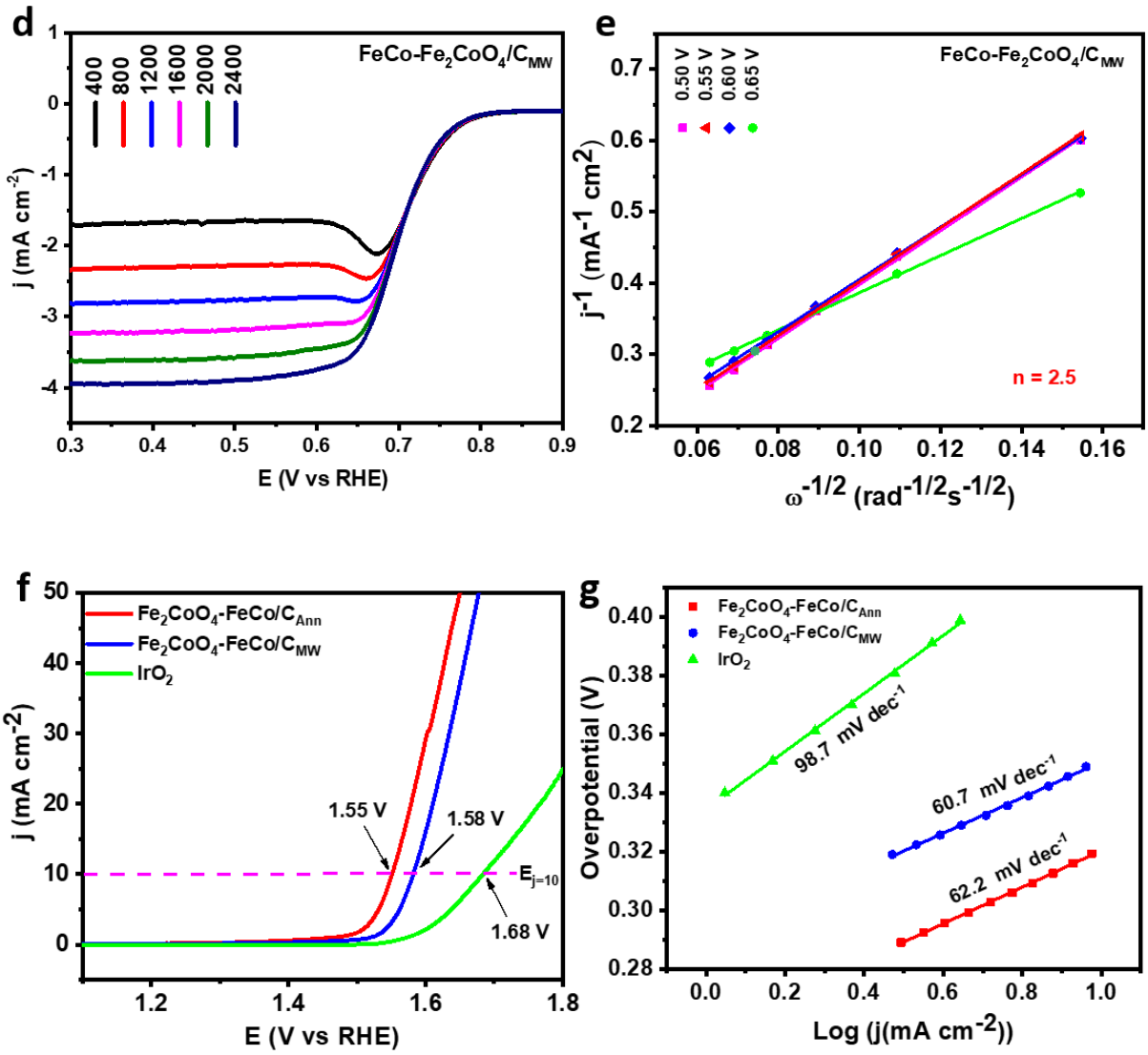

Figure 5. 6: (a) ORR polarization curves for the FeCo-Fe_2CoO_4/C samples and Pt/C at 1600 rpm. (b) LSV curves at different rotation rates for FeCo-Fe_2CoO_4/C_{Ann} (c) Koutecky-Levich plots for FeCo-Fe_2CoO_4/C_{Ann} (d) LSV curves at different rotation rates for FeCo-Fe_2CoO_4/C_{MW} (e) Koutecky-Levich plots for FeCo-Fe_2CoO_4/C_{MW} (f) OER polarization curves for the FeCo-Fe_2CoO_4/C samples and IrO_2 at 1600 rpm. (f) Tafel slopes for the FeCo-Fe_2CoO_4/C catalysts and IrO_2.

5.3.3. Rechargeable zinc-air battery

The lower the bifunctionality index (potential difference between ORR half-wave potential and OER potential @ 10 $mAcm^{-2}$), the better the performance in rechargeable zinc-air batteries. FeCo-Fe_2CoO_4/C_{Ann} has a small potential (ΔE = 0.76 V) difference compared to FeCo-Fe_2CoO_4/C_{MW} (ΔE = 0.84 V), however, slightly similar to that of Pt/C-IrO_2 (ΔE = 0.75 V) (**Figure 5.7 (a)**). This led to the continuation of FeCo-Fe_2CoO_4/C_{Ann} in rechargeable zinc-air battery measurements. To construct the zinc-air battery, FeCo-Fe_2CoO_4/C_{Ann} was loaded on carbon paper and used as the electrocatalyst at the air cathode. This was paired with the zinc plate which acted as the anode and 6 M KOH + 0.2 M Zinc acetate as the electrolyte as demonstrated in **Figure 5.7 (b)**. To ensure reversible Zn electrochemical reactions at the anode, zinc acetate is dissolved in KOH to form zincate, $Zn(OH)_4^{2-}$ [33,34]. For comparison, the Pt/C-IrO_2 cell was also assembled. The peak power density of FeCo-Fe_2CoO_4/C_{Ann} is 146.12 $mWcm^{-2}$ which is smaller than that of Pt/C-IrO_2, 208.52 $mWcm^{-2}$ (**Figure 5.7 (c)**). Platinum-based electrocatalysts are unanimously considered the most efficient catalysts for ORR hence the superior power density [35]. The specific capacity of the zinc-air battery was determined by fully discharging the battery at 10 $mAcm^{-2}$ and was normalised to the mass of zinc consumed. FeCo-Fe_2CoO_4/C_{Ann} demonstrated an excellent specific capacity of 690 mAh g^{-1} compared to Pt/C-IrO_2 (421 mAh g^{-1}) proving the superiority of the electrocatalyst (**Figure 5.7 (d)**). The zinc plate thins gradually as the discharge continues and the cell ceases functioning as all the zinc is consumed and more zinc salts agglomerate in the electrolyte (**Figure 5.7 (d)**). In addition, different current densities were evaluated for the discharge performance of FeCo-Fe_2CoO_4/C_{Ann} (**Figure 5.7 (e)**). Stable discharge voltages were observed at each current density (from 0.1 $mAcm^{-2}$ to 10 $mAcm^{-2}$) and this proves the excellence of the electrocatalyst for ORR (good rate capability). The discharge voltages were gradually decreased with increasing current densities. After cycling at higher current densities, the discharge voltages at 0.1 mA cm^{-2}

increased compared to the initial and this is attributed to the activation of the material during cycling. The battery was continually discharged and charged at 10 mA cm^{-2} for 8 h per cycle as shown in **Figure 5.7 (f)**. A stable discharge voltage of ~1.20 V was maintained for 50 h until a significant voltage drop was observed. The voltage gap (ΔE) for the FeCo-Fe_2CoO_4/C_{Ann} battery was 0.76 V during the second cycle while that of Pt/C-IrO_2 was 1.27 V as demonstrated in **Figure SB2** (supporting documents). The FeCo-Fe_2CoO_4/C_{Ann} maintained an excellent voltage gap for consecutive cycles and proved to be a promising bifunctional electrocatalyst in RZAB. The FeCo-Fe_2CoO_4/C_{Ann} battery was cycled at an areal energy density of 48.4 $mWhcm^{-2}$, higher than the recommended 35 $mWhcm^{-2}$ and better than most catalysts reported in the literature (**Table 2.1**) [36]. The highest areal energy density achieved for FeCo-Fe_2CoO_4/C_{Ann} was 60.5 $mWhcm^{-2}$ (**Figure SB3 in the supporting documents**). During cycling at 10 mA cm^{-2}, 8 h per cycle, the FeCo-Fe_2CoO_4/C_{MW} assembled battery shows deterioration in the discharge voltage after one cycle as shown in **Figure SB4**. This proves the instability of FeCo-Fe_2CoO_4/C_{MW} in RZAB. Although FeCo-Fe_2CoO_4/C_{MW} showed increased oxygen vacancies, BET surface area, BET pore volume, and increased defects, its suitability for RZAB application is insufficient. This implies the higher alloy content in FeCo-Fe_2CoO_4/C_{Ann} greatly improved the catalysts' stability in RZAB. Oxidising the alloy component by microwaving in the air greatly compromised the stability of the material.

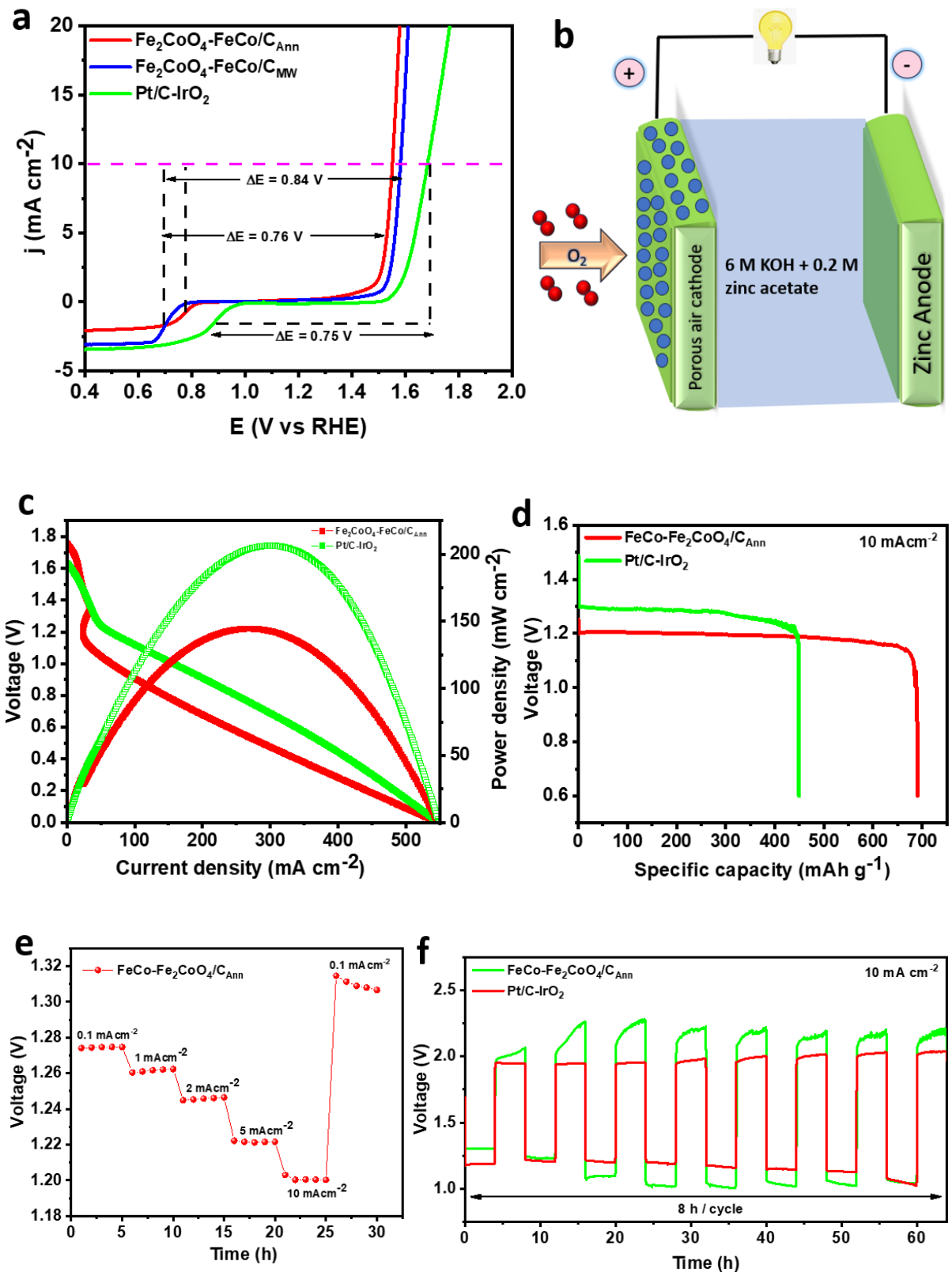

Figure 5. 7: (a) ORR/OER bifunctionality curves (b) A schematic diagram of a zinc-air battery. (c) Discharge polarization curves and the corresponding power density curves of the batteries

using FeCo-Fe_2CoO_4/C_{Ann} or Pt/C-IrO_2 as air electrode catalysts. (d) Galvanostatic discharge curves. (e) Long-term discharge-charge cycles (4 h charge and 4 h discharge).

5.4. Summary

In summary, FeCo-Fe_2CoO_4/C electrocatalysts were successfully synthesized using a simple reduction method. Microwave irradiation was employed to improve the catalytic activity of the FeCo-Fe_2CoO_4/C_{Ann} catalyst, however, this strategy proved to be unsuccessful despite improved physicochemical properties (surface area, pore volume, oxygen vacancies and carbon defects). FeCo-Fe_2CoO_4/C_{Ann} proved to be an excellent electrocatalyst for both ORR and OER with the $E_{1/2}$ = 0.74 V and $E_{j=10}$ = 1.55 V. The material also shows good stability in RZAB when cycled for 60 h at areal energy densities of 48.4 mWh cm^{-2} and 60.5 mWh cm^{-2}. The greater alloy component in FeCo-Fe_2CoO_4/C_{Ann} brings about good stability in RZAB. This work strategically brings the synergistic effects of alloys and oxides together for improved rechargeable zinc-air battery performance.

5.5. References

(1) Van Der Wiel, K.; Bloomfield, H. C.; Lee, R. W.; Stoop, L. P.; Blackport, R.; Screen, J. A.; Selten, F. M. The Influence of Weather Regimes on European Renewable Energy Production and Demand. *Environmental Research Letters* **2019**, *14* (9). https://doi.org/10.1088/1748-9326/ab38d3.

(2) Xu, Y.; Chen, B.; Nie, J.; Ma, G. Reactive Template-Induced Core-Shell FeCo@C Microspheres as Multifunctional Electrocatalysts for Rechargeable Zinc-Air Batteries. *Nanoscale* **2018**, *10* (36), 17021–17029. https://doi.org/10.1039/c8nr02492h.

(3) Qin, Y.; Ou, Z.; Xu, C.; Zhang, Z.; Yi, J.; Jiang, Y.; Wu, J.; Guo, C.; Si, Y.; Zhao, T. Progress of Carbon-Based Electrocatalysts for Flexible Zinc-Air Batteries in the Past 5 Years: Recent Strategies for Design, Synthesis and Performance Optimization. *Nanoscale Research Letters*. Springer 2021. https://doi.org/10.1186/s11671-021-03548-5.

(4) Fang, H.; Huang, T.; Sun, Y.; Kang, B.; Liang, D.; Yao, S.; Yu, J.; Dinesh, M. M.; Wu, S.; Lee, J. Y.; Mao, S. Metal-Organic Framework-Derived Core-Shell-Structured Nitrogen-Doped CoCx/FeCo@C Hybrid Supported by Reduced Graphene Oxide Sheets as High Performance Bifunctional Electrocatalysts for ORR and OER. *J Catal* **2019**, *371*, 185–195. https://doi.org/10.1016/j.jcat.2019.02.005.

(5) Winter, M.; Brodd, R. J. What Are Batteries, Fuel Cells, and Supercapacitors? *Chem Rev* **2004**, *104* (10), 4245–4269. https://doi.org/10.1021/cr020730k.

(6) Lin, L.; Lei, W.; Zhang, S.; Liu, Y.; Wallace, G. G.; Chen, J. Two-Dimensional Transition Metal Dichalcogenides in Supercapacitors and Secondary Batteries. *Energy*

Storage Materials. Elsevier B.V. May 1, 2019, pp 408–423. https://doi.org/10.1016/j.ensm.2019.02.023.

(7) Omabegho, T.; Sha, R.; Seeman, N. C. A Bipedal DNA Brownian Motor with Coordinated Legs. *Science (1979)* **2009**, *324* (5923), 67–71. https://doi.org/10.1126/science.1170336.

(8) Fu, X.; Liu, Y.; Cao, X.; Jin, J.; Liu, Q.; Zhang, J. FeCo-Nx Embedded Graphene as High Performance Catalysts for Oxygen Reduction Reaction. *Appl Catal B* **2013**, *130–131*, 143–151. https://doi.org/10.1016/j.apcatb.2012.10.028.

(9) Li, C.; Wu, M.; Liu, R. High-Performance Bifunctional Oxygen Electrocatalysts for Zinc-Air Batteries over Mesoporous Fe/Co-N-C Nanofibers with Embedding FeCo Alloy Nanoparticles. *Appl Catal B* **2019**, *244*, 150–158. https://doi.org/10.1016/j.apcatb.2018.11.039.

(10) Ipadeola, A. K.; Haruna, A. B.; Gaolatlhe, L.; Lebechi, A. K.; Meng, J.; Pang, Q.; Eid, K.; Abdullah, A. M.; Ozoemena, K. I. Efforts at Enhancing Bifunctional Electrocatalysis and Related Events for Rechargeable Zinc-Air Batteries. *ChemElectroChem* **2021**, 1–22. https://doi.org/10.1002/celc.202101284.

(11) Chen, K.; Kim, S.; Rajendiran, R.; Prabakar, K.; Li, G.; Shi, Z.; Jeong, C.; Kang, J.; Li, O. L. Enhancing ORR/OER Active Sites through Lattice Distortion of Fe-Enriched FeNi3 Intermetallic Nanoparticles Doped N-Doped Carbon for High-Performance Rechargeable Zn-Air Battery. *J Colloid Interface Sci* **2021**, *582*, 977–990. https://doi.org/10.1016/j.jcis.2020.08.101.

(12) Fashedemi, O. O.; Ozoemena, K. I. Enhanced Methanol Oxidation and Oxygen Reduction Reactions on Palladium-Decorated FeCo@Fe/C Core-Shell Nanocatalysts

in Alkaline Medium. *Physical Chemistry Chemical Physics* **2013**, *15* (48), 20982–20991. https://doi.org/10.1039/c3cp52601a.

(13) Pandia Rajathi, M.; Berchmans, S. Poly (3, 4-Ethylene Dioxythiophene) Supported Palladium Catalyst Prepared by Galvanic Replacement Reaction for Methanol Tolerant Oxygen Reduction. *Sci Rep* **2019**, *9* (1). https://doi.org/10.1038/s41598-019-55688-5.

(14) Liu, W.; Niu, X.; Feng, J.; Yin, R.; Ma, S.; Que, W.; Dai, J.; Tang, J.; Wu, F.; Shi, W.; Liu, X.; Cao, X. Tunable Heterogeneous FeCo Alloy-Mo0.82N Bifunctional Electrocatalysts for Temperature-Adapted Zn-Air Batteries. *ACS Appl Mater Interfaces* **2023**, *15* (12), 15344–15352. https://doi.org/10.1021/acsami.2c21616.

(15) Yan, J.; Huang, Y.; Liu, P.; Wei, C. Large-Scale Controlled Synthesis of Magnetic FeCo Alloy with Different Morphologies and Their High Performance of Electromagnetic Wave Absorption. *Journal of Materials Science: Materials in Electronics* **2017**, *28* (4), 3159–3167. https://doi.org/10.1007/s10854-016-5904-4.

(16) Zehani, K.; Bez, R.; Moscovici, J.; Mazaleyrat, F.; Mliki, N.; Bessais, L. High Magnetic Moment of FeCo Nanoparticles Produced in Polyol Medium. *IEEE Trans Magn* **2014**, *50* (4). https://doi.org/10.1109/TMAG.2013.2288411.

(17) Sundararajan, M.; Kennedy, L. J.; Aruldoss, U.; Pasha, S. K.; Vijaya, J. J.; Dunn, S. Microwave Combustion Synthesis of Zinc Substituted Nanocrystalline Spinel Cobalt Ferrite: Structural and Magnetic Studies. *Mater Sci Semicond Process* **2015**, *40*, 1–10. https://doi.org/10.1016/j.mssp.2015.06.002.

(18) Najm, A. S.; Naeem, H. S.; Alwarid, D. A. R. M.; Aljuhani, A.; Hasbullah, S. A.; Hasan, H. A.; Sopian, K.; Bais, B.; Al-Iessa, H. J.; Majdi, H. S.; Sultan, A. J.; Moria, H. Mechanism of Chemical Bath Deposition of CdS Thin Films: Influence of Sulphur

Precursor Concentration on Microstructural and Optoelectronic Characterizations. *Coatings* **2022**, *12* (10). https://doi.org/10.3390/coatings12101400.

(19) Park, J. W.; Shin, J.; Ju, Y. W. Influence of Calcination Temperature on Electrochemical Properties of Perovskite Oxide Nanofiber Catalysts. *Energies (Basel)* **2023**, *16* (13). https://doi.org/10.3390/en16134979.

(20) Potpattanapol, P.; Tang, I. M.; Somyanonthanakun, W.; Thongmee, S. Exchange Bias Effect in FeCo Nanoparticles. *J Supercond Nov Magn* **2018**, *31* (3), 791–796. https://doi.org/10.1007/s10948-017-4389-6.

(21) Laudon, Matthew.; Romanowicz, B. F.; Nano Science and Technology Institute. *Nanotech : Technical Proceedings of the 2014 NSTI Nanotechnology Conference and Expo : June 15-18, Washington, D.C., U.S.A.*

(22) Li, T.; Yao, Y.; Ko, B. H.; Huang, Z.; Dong, Q.; Gao, J.; Chen, W.; Li, J.; Li, S.; Wang, X.; Shahbazian-Yassar, R.; Jiao, F.; Hu, L. Carbon-Supported High-Entropy Oxide Nanoparticles as Stable Electrocatalysts for Oxygen Reduction Reactions. *Adv Funct Mater* **2021**, *31* (21). https://doi.org/10.1002/adfm.202010561.

(23) Liu, D.; Ai, H.; Li, J.; Fang, M.; Chen, M.; Liu, D.; Du, X.; Zhou, P.; Li, F.; Lo, K. H.; Tang, Y.; Chen, S.; Wang, L.; Xing, G.; Pan, H. Surface Reconstruction and Phase Transition on Vanadium–Cobalt–Iron Trimetal Nitrides to Form Active Oxyhydroxide for Enhanced Electrocatalytic Water Oxidation. *Adv Energy Mater* **2020**, *10* (45). https://doi.org/10.1002/aenm.202002464.

(24) Yuan, M.; Nan, C.; Yang, Y.; Sun, G.; Li, H.; Ma, S. Uniform FexNiy Nanospheres: Cost-Effective Electrocatalysts for Nonaqueous Rechargeable Li-O2 Batteries. *ACS Omega* **2017**, *2* (8), 4269–4277. https://doi.org/10.1021/acsomega.7b00497.

(25) Huang, J.; Li, X.; Jiang, S.; Liu, C.; Lu, M.; Yang, Y. Boosted Sodium Storage Performance by Iron Doping in Hybrid Spheres of Cobalt Selenide/Carbon Composite Anode. *J Electron Mater* **2022**, *51* (12), 6626–6636. https://doi.org/10.1007/s11664-022-09909-9.

(26) Liu, Z.; Wan, J.; Li, M.; Shi, Z.; Liu, J.; Tang, Y. Synthesis of Co/CeO2hetero-Particles with Abundant Oxygen-Vacancies Supported by Carbon Aerogels for ORR and OER. *Nanoscale* **2022**, *14* (5), 1997–2003. https://doi.org/10.1039/d1nr07595k.

(27) Guo, Y.; Sun, Q.; Song, K.; Ding, J.; Shi, C.; He, F. Rational Design of FeCo Imbedded 3D Porous Carbon Microspheres as Broadband and Lightweight Microwave Absorbers. *J Mater Sci* **2021**, *56* (3), 2212–2225. https://doi.org/10.1007/s10853-020-05424-6.

(28) Kuang, D.; Hou, L.; Wang, S.; Luo, H.; Deng, L.; Mead, J. L.; Huang, H.; Song, M. Large-Scale Synthesis and Outstanding Microwave Absorption Properties of Carbon Nanotubes Coated by Extremely Small FeCo-C Core-Shell Nanoparticles. *Carbon N Y* **2019**, *153*, 52–61. https://doi.org/10.1016/j.carbon.2019.06.105.

(29) De, M.; Rout, A.; Tewari, H. S. Synthesis and Structural Characterization of A-Site Doped NiFe2O4. In *AIP Conference Proceedings*; American Institute of Physics Inc., 2017; Vol. 1837. https://doi.org/10.1063/1.4982126.

(30) Lee, A. Y.; Yang, K.; Anh, N. D.; Park, C.; Lee, S. M.; Lee, T. G.; Jeong, M. S. Raman Study of D* Band in Graphene Oxide and Its Correlation with Reduction. *Appl Surf Sci* **2021**, *536*. https://doi.org/10.1016/j.apsusc.2020.147990.

(31) Fang, H.; Huang, T.; Sun, Y.; Kang, B.; Liang, D.; Yao, S.; Yu, J.; Dinesh, M. M.; Wu, S.; Lee, J. Y.; Mao, S. Metal-Organic Framework-Derived Core-Shell-Structured Nitrogen-Doped CoCx/FeCo@C Hybrid Supported by Reduced Graphene Oxide

Sheets as High Performance Bifunctional Electrocatalysts for ORR and OER. *J Catal* **2019**, *371*, 185–195. https://doi.org/10.1016/j.jcat.2019.02.005.

(32) Xu, Y.; Chen, B.; Nie, J.; Ma, G. Reactive Template-Induced Core-Shell FeCo@C Microspheres as Multifunctional Electrocatalysts for Rechargeable Zinc-Air Batteries. *Nanoscale* **2018**, *10* (36), 17021–17029. https://doi.org/10.1039/c8nr02492h.

(33) Li, Y.; Gong, M.; Liang, Y.; Feng, J.; Kim, J. E.; Wang, H.; Hong, G.; Zhang, B.; Dai, H. Advanced Zinc-Air Batteries Based on High-Performance Hybrid Electrocatalysts. *Nat Commun* **2013**, *4*. https://doi.org/10.1038/ncomms2812.

(34) Liu, X.; Yuan, Y.; Liu, J.; Liu, B.; Chen, X.; Ding, J.; Han, X.; Deng, Y.; Zhong, C.; Hu, W. Utilizing Solar Energy to Improve the Oxygen Evolution Reaction Kinetics in Zinc–Air Battery. *Nat Commun* **2019**, *10* (1). https://doi.org/10.1038/s41467-019-12627-2.

(35) Wang, X.; Li, Z.; Qu, Y.; Yuan, T.; Wang, W.; Wu, Y.; Li, Y. Review of Metal Catalysts for Oxygen Reduction Reaction: From Nanoscale Engineering to Atomic Design. *Chem*. Elsevier Inc June 13, 2019, pp 1486–1511. https://doi.org/10.1016/j.chempr.2019.03.002.

(36) Hopkins, B. J.; Chervin, C. N.; Parker, J. F.; Long, J. W.; Rolison, D. R. An Areal-Energy Standard to Validate Air-Breathing Electrodes for Rechargeable Zinc–Air Batteries. *Advanced Energy Materials*. Wiley-VCH Verlag August 1, 2020. https://doi.org/10.1002/aenm.202001287.

Chapter 6

Conclusions and recommendations

General conclusions

- Acid treating the OLC-supported $HESO_x$ was an effective method for introducing defects, increasing the surface area and functionalizing the catalyst. These parameters together improved the catalytic activity of $HESO_x$-550/OLC_{AT}.
- Despite what is reported regarding microwave irradiation, this procedure failed to improve the catalytic activity of the FeCo-Fe_2CoO_4/C_{MW} electrocatalysts. The only improvement observed was with the conductivity of the material however other parameters were impaired. Therefore FeCo-Fe_2CoO_4/C_{Ann} emerged as a better catalyst.
- Using carbon supports proved to be valuable in improving the conductivity of the catalysts.
- Non-noble metal-based electrocatalysts ($HESO_x$ and FeCo) in this project were significantly better than well-known noble metal-based (Pt/C and IrO_2) electrocatalysts in catalysing the cathodic reactions in rechargeable zinc-air batteries.

Recommendations

- The metal content in $HESO_x$-550/OLC and $HESO_x$-550/OLC_{AT} catalysts can be increased to reduce carbon corrosion during RZAB operation. Instead of 10% $HESO_x$ and 90% OLC, the ratios can be optimised to obtain the highest performance.
- Microwave irradiation was carried out in an open microwave system therefore a closed system can be used to eliminate side reactions.

- A pure zinc metal plate was used as the anode in RZABs, and it is prone to corrosion. The zinc anode should be re-designed to eliminate corrosion and dendrite formation thereby improving the stability and cycle life of the battery.

Appendix A

Supporting information for chapter 4.

Onion-like carbon supported high-entropy spinel oxides [$(CoCuFeMnNi)_3O_4$] for robust rechargeable zinc-air batteries.

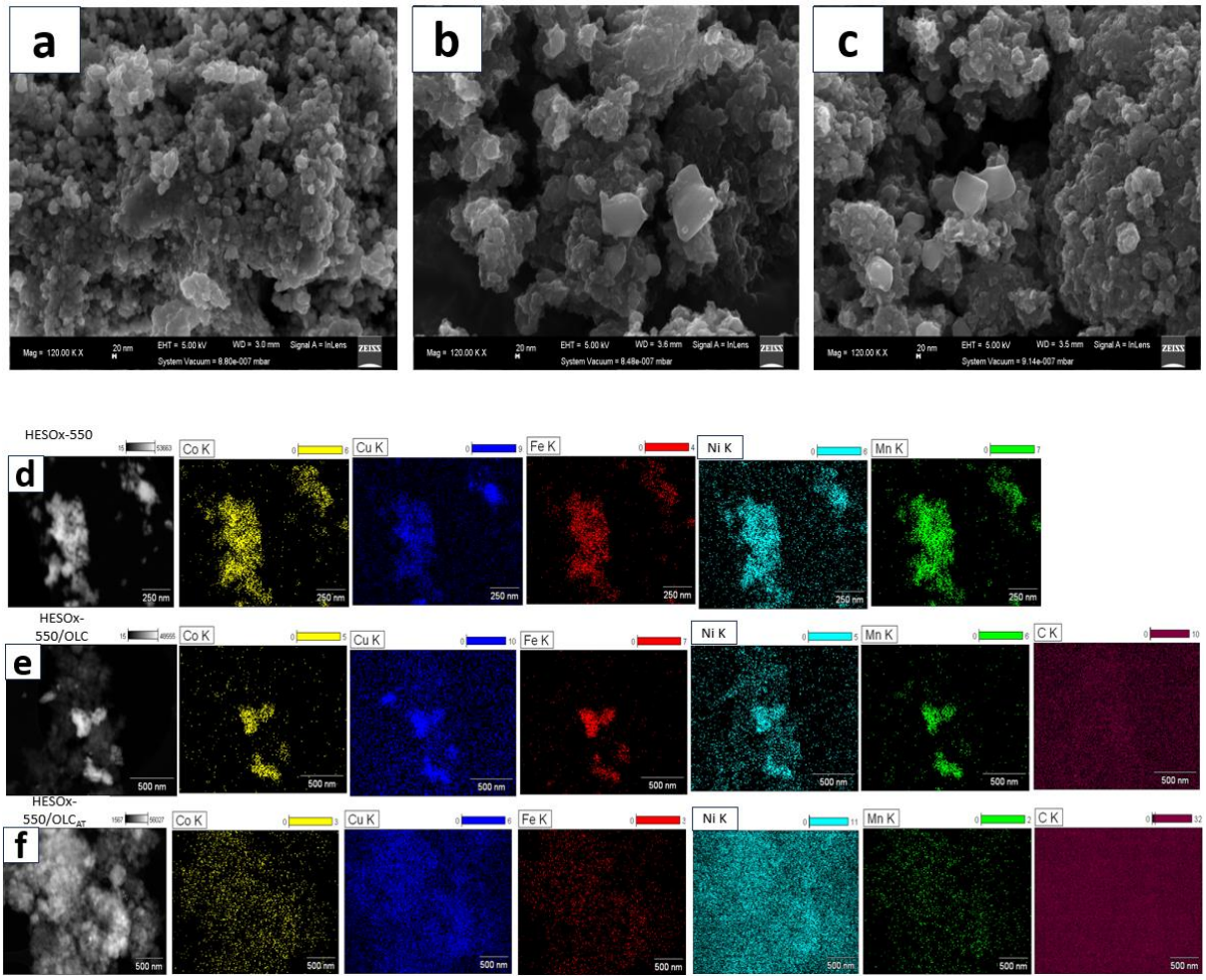

Figure S 1: SEM images (a-c) and EDS (d-f) for $HESO_x$-550, $HESO_x$-550/OLC and $HESO_x$-550/OLC_{AT} respectively.

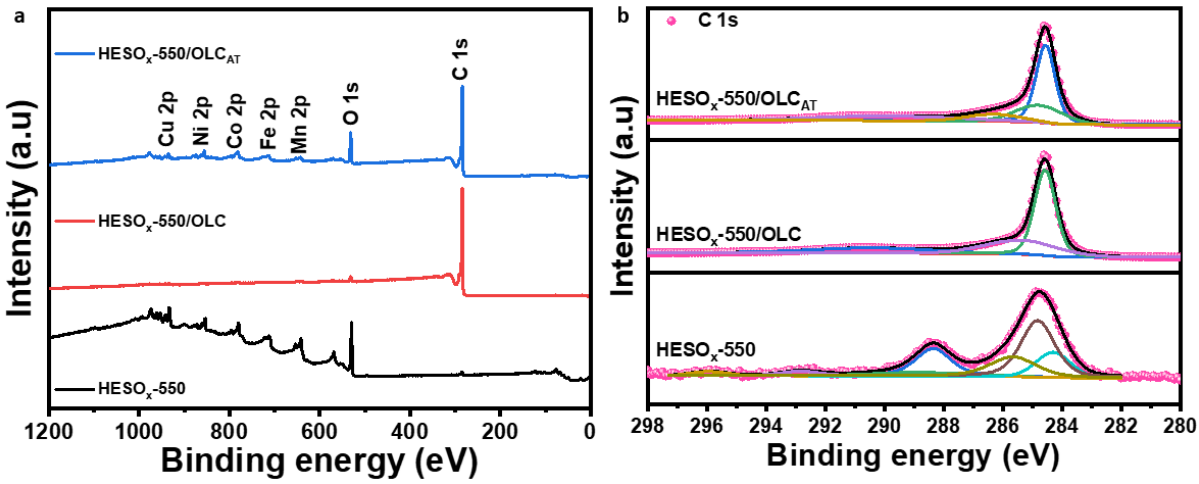

Figure S 2: The XPS survey scans (a) and C 1s spectra (b) for $HESO_x$-550, $HESO_x$-550/OLC and $HESO_x$-550/OLC_{AT}.

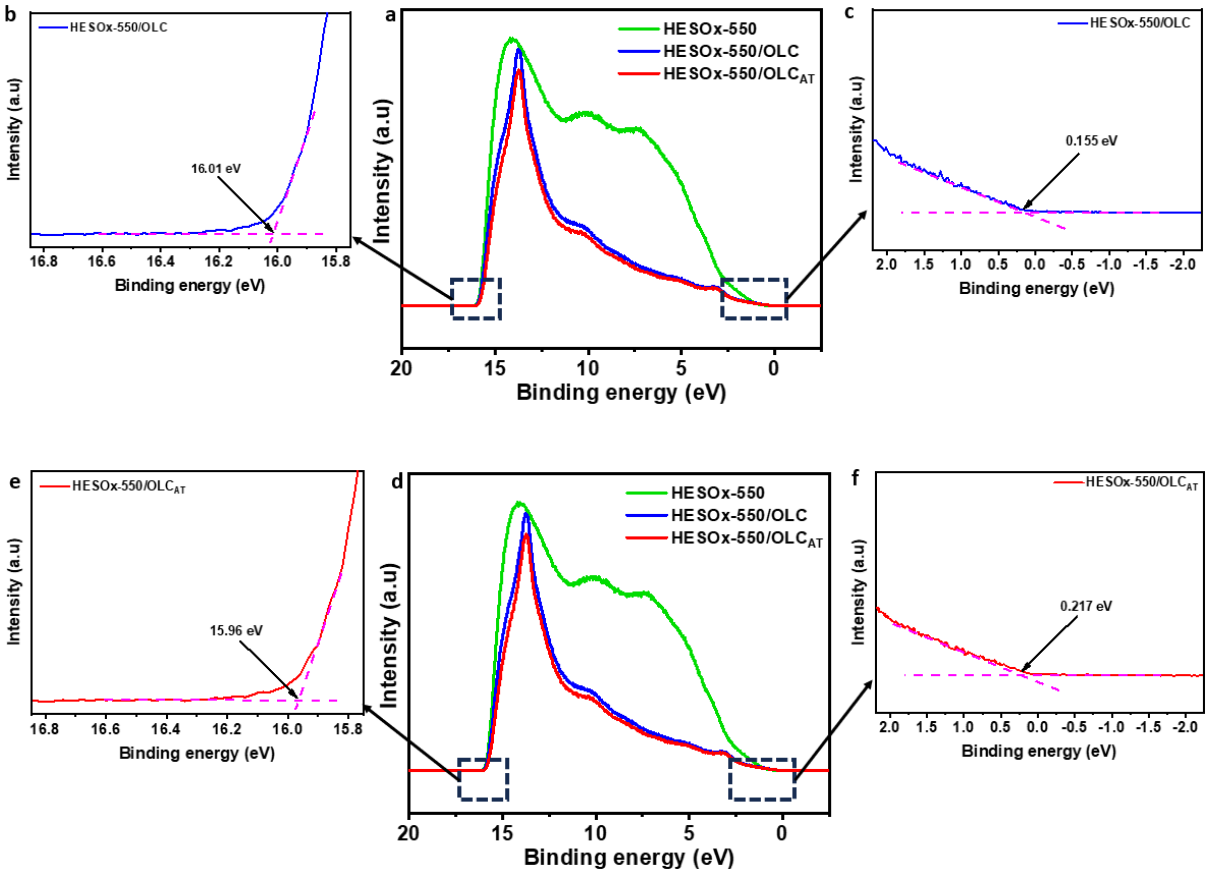

Figure S 3: (a) UPS spectrum for $HESO_x$ samples. (b,e) Left plot: Secondary electron emission for $HESO_x$-550/OLC and $HESO_x$-550/OLC_{AT} respectively. (c,f) Right plot: The

zoomed area near the valence band for $HESO_x$-550/OLC and $HESO_x$-550/OLC_{AT} respectively.

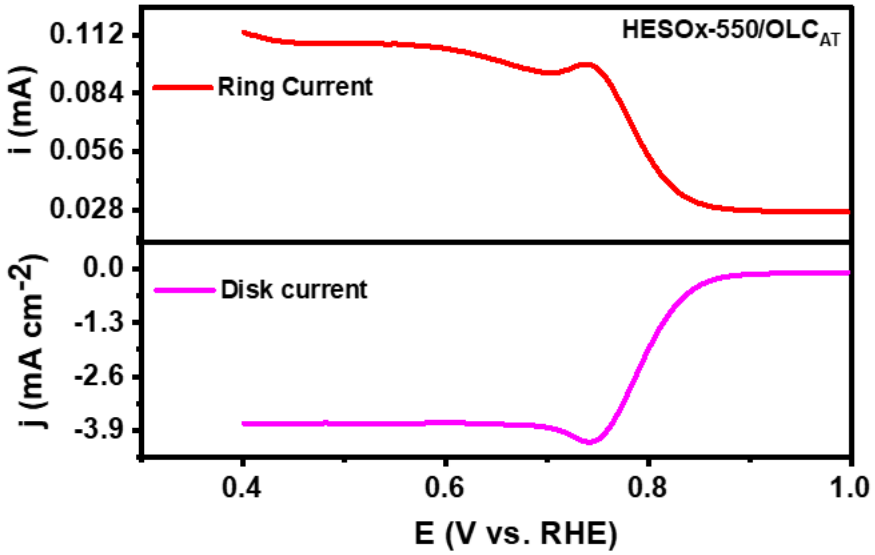

Figure S 4: ORR RRDE measurements at 5 mV/s, 1600 rpm at the disk with the collected ring current holding 1.2 V at the ring in O_2 saturated 1 M KOH for $HESO_x$-550/OLC_{AT}.

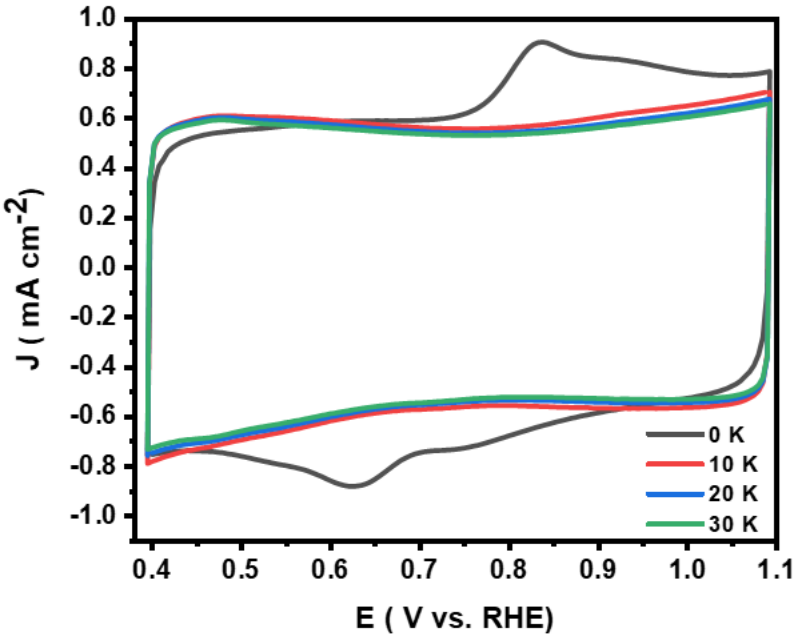

Figure S 5: Accelerated durability test CV in Ar at 50 mV/s for $HESO_x$-550/OLC_{AT}.

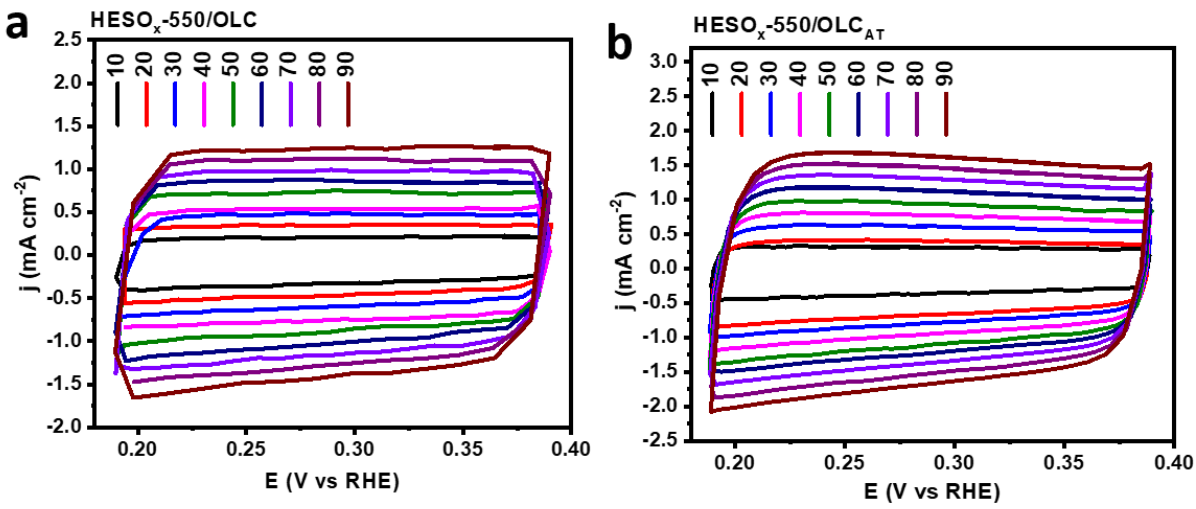

Figure S 6: CV curves obtained in the non-Faradaic regions for (a) $HESO_x$-550/OLC and (b) $HESO_x$-550/OLC_{AT}.

Table S 1: A table summarizing the ECSA of the $HESO_x$ composites.

Catalyst	**ECSA**
$HESO_x$-550/OLC	330.93
$HESO_x$-550/OLC_{AT}	404.93

The constructed HESOx-550/OLC_{AT} and standard zinc-air batteries were fully discharged to determine the specific capacity as illustrated in **Figure S7**. During the galvanostatic discharging at 10 $mAcm^{-2}$ for ~53 h, the voltage remained stable for ~35 h until a visible voltage drop was observed for $HESO_x$-550/OLC_{AT}. After ~32 h of discharging, a significant voltage drop was observed after ~2 h for the Pt/C-IrO_2. The excellent discharge stability was owed to the superiority of the $HESO_x$-550/OLC_{AT} catalyst. Gradually, the zinc foil thinned, and more zinc salts were agglomerated in the electrolyte as the discharge continued. At some point, all the Zn metal in the battery was consumed, and the battery eventually ceased to function. The specific capacity normalised to the mass of zinc consumed was 742 mAh g^{-1} and 421 mAh g^{-1} for $HESO_x$-550/OLC_{AT} and Pt/C-IrO_2 respectively.

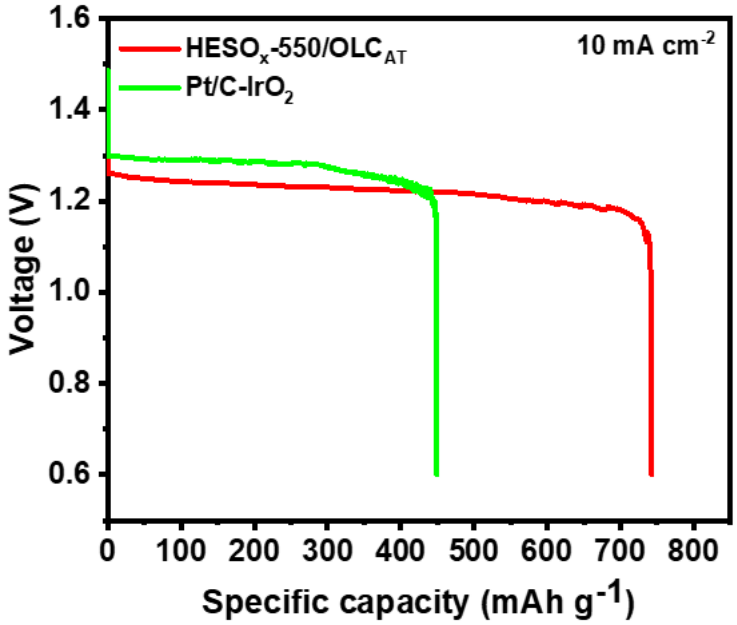

Figure S 7: Discharge curves for $HESO_x$-550/OLC_{AT} and Pt/C-IrO_2 at 10 mA cm^{-2}.

Figure S8 depicts the excellent stability of HESOx-550/OLC_{AT} by monitoring the ΔE after every 50th cycle. The ΔE remains stable for 200 h until a drastic change is observed. The increased charge voltage is attributed to impaired OER kinetics or HER promotion while the decreased discharge voltage is attributed to ohmic, and mass transport loss [1]. Another factor leading to voltage decay is the formation of the dendrites at the zinc anode [2].

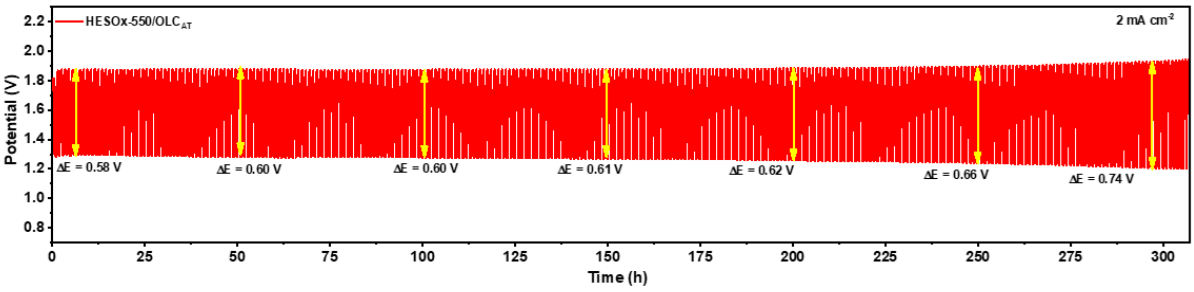

Figure S 8: Discharge-charge profiles of $HESO_x$-550/OLC_{AT} at 2 mA cm^{-2} with 30 min charge/discharge depicting how the ΔE changes after every 50 h.

Figure S9 depicts the discharge-charge curves for $HESO_x$-550/OLC under shallow cycling. The initial ΔE 0.65 V was observed which is higher than that of $HESO_x$-550/OLC_{AT} (0.58 V). This further corroborates the results obtained in the three-electrode working system ($HESO_x$-550/OLC_{AT} is better than $HESO_x$-550/OLC).

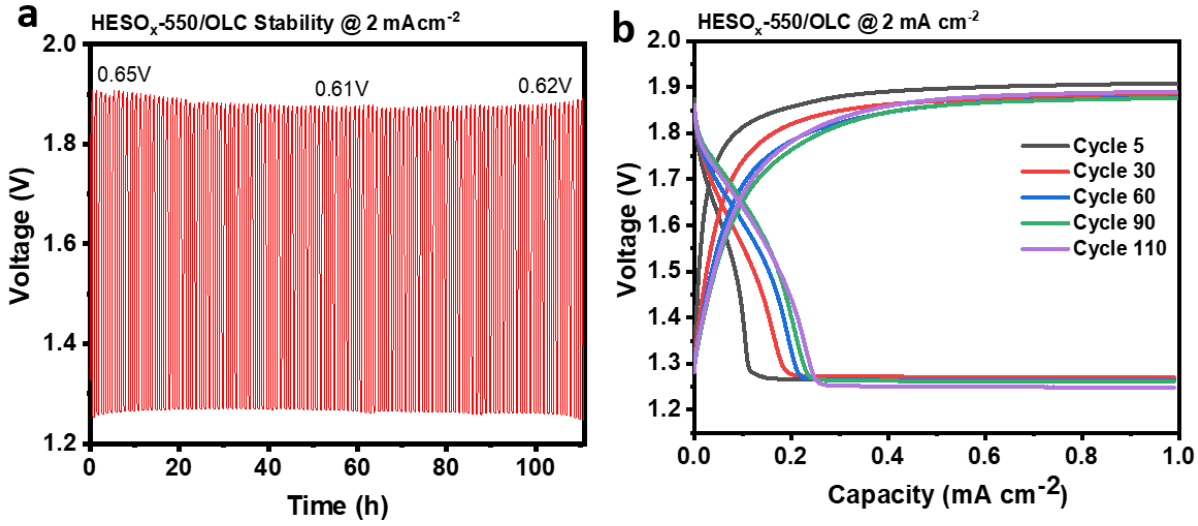

Figure S 9: (a) The long-term stability test for $HESO_x$-550/OLC at 2 mA cm^{-2}, 30 min discharge and 30 min charge (b) The discharge-charge charge curves for $HESO_x$-550/OLC at different cycle numbers.

Figure S10 depicts the $HESO_x$-550/OLC_{AT} stability at different DODs and current densities for the same cell. The discharge voltage remains stable at 23.9% DOD however the DOD change to 41% leads to decreased discharge voltage. Changing the current density to 10 mA cm^{-2} further degrades the cell proving the instability of the zinc anode under harsh DOD conditions and high current densities.

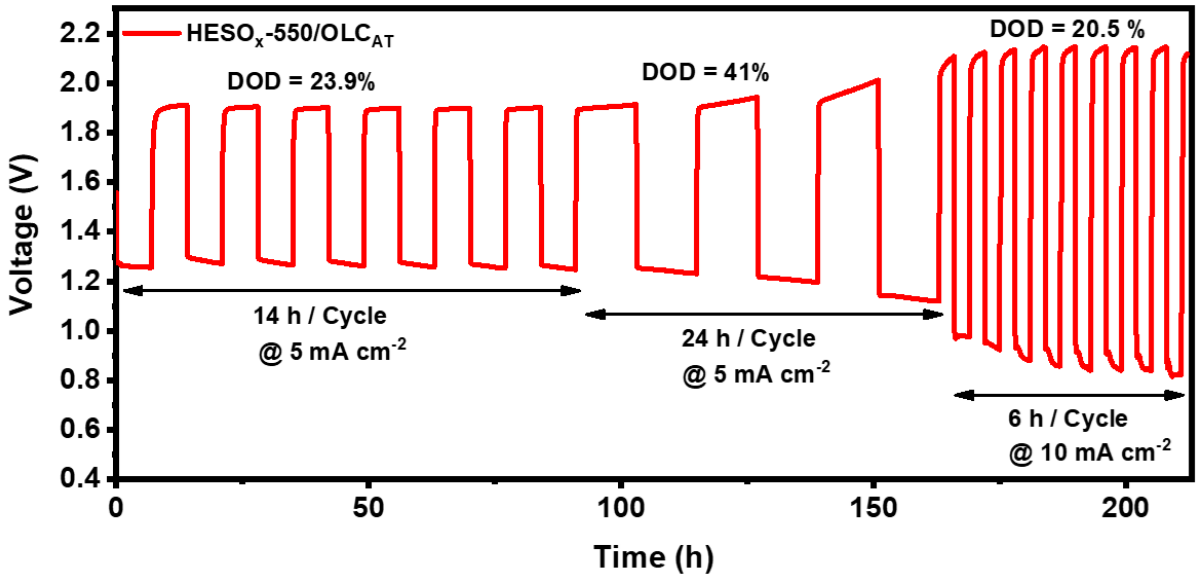

Figure S 10: Discharge-charge profiles of $HESO_x$-550/OLC_{AT} at 5 mA cm^{-2} and 10 $mAcm^{-2}$.

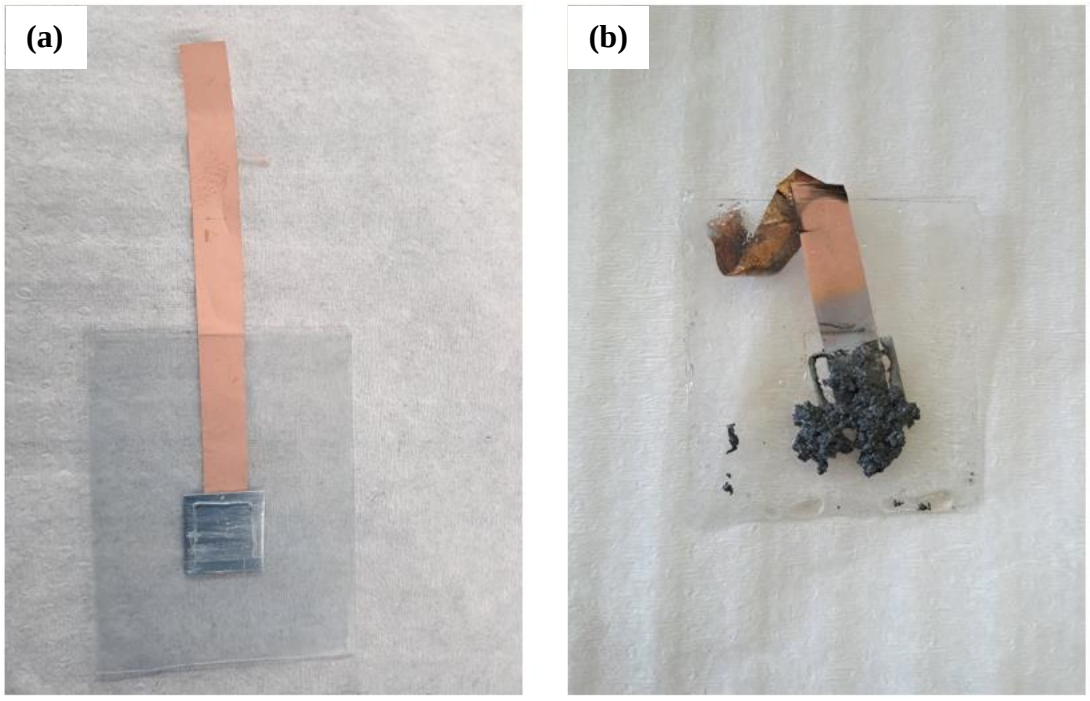

Figure S 11: Pictures depicting the zinc plate (a) before cycling and (b) after cycling under harsh DOD conditions (8 h per cycle and 10 mA cm^{-2}).

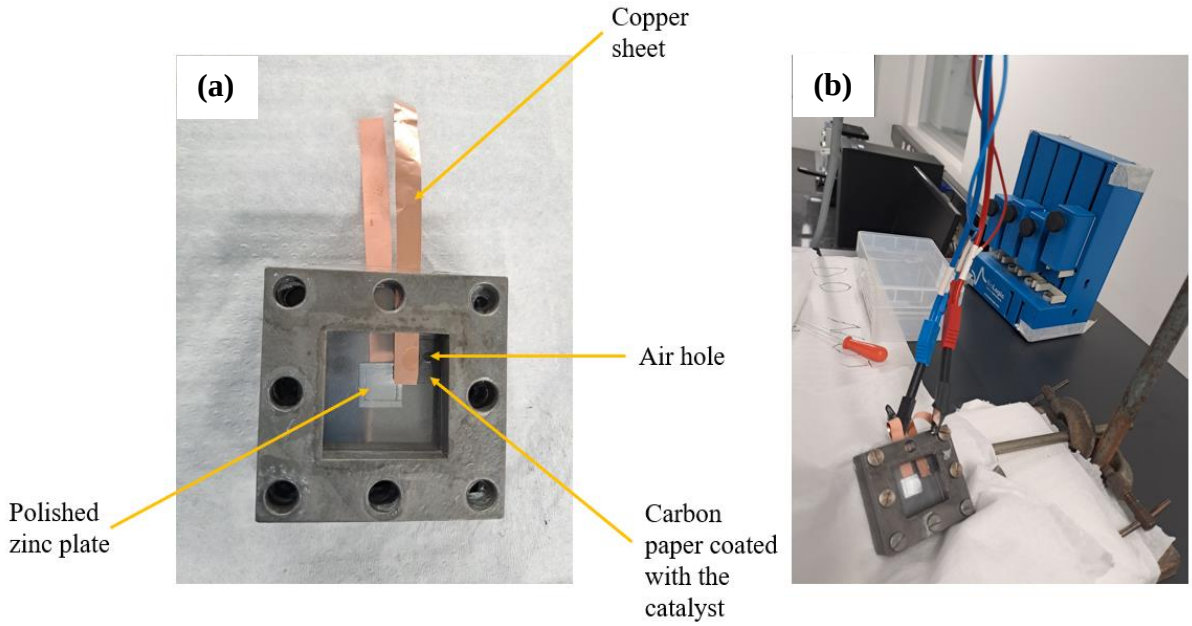

Figure S 12: (a) The assembled zinc-air batter (b) The assembled zinc-air battery connected to the battery tester.

Table S 2: ORR and OER comparison table for the catalysts reported in the literature.

Year	Catalyst	OER $E_{j=10}$ [V]	ORR $E_{1/2}$ [V]	ΔE [V]	Tafel [mV dec-1]	Electrolyte	References
2024	$(CoCuFeNiMn)_3O_4$/OLC	1.53	0.83	0.70	48.4: OER	ORR: 1 M KOH OER: 1 M KOH	This work
2020	AlNiCoRuMo	1.50	0.875	0.61	54.5	1.0 M KOH	[3]
2022	AlNiCoRuMoCrFeTi	1.48	0.87	0.61	51.3	ORR: 0.1 M KOH OER: 1 M KOH	[4]
2021	np−AlCoFeMoCr/Pt	1.49		0.62	52.4		[5]
2022	AlNiCoFeCrMoV-based HEO/CoNC	1.487	0.85	0.64	54.6	ORR: 0.1 M KOH OER: 1 M KOH	[6]
2023	CrMnFeCoNi	1.50	0.78	0.734	37.9	ORR:0.1 M KOH	[7]

2023	$Fe_{12}Ni_{23}Cr_{10}Co_{30}Mn_{25}$/CNT	1.51	0.81	0.70	ORR: 69.2 OER:77.4	ORR: 0.1 M KOH OER: 0.1 M KOH	[8]
2022	$Mn_{70}Ni_{7.5}Cu_{7.5}Co_{4.2}V_{4.2}Fe_2Mo_2Pd_{0.5}Pt_{0.5}Au_{0.5}Ru_{0.5}Ir_{0.5}$ Alloy (np-12)	1.435	0.90	0.535	74.2: OER	ORR: 0.1 M KOH OER: 1 M KOH	[9]
2023	FeCoNiMnCu-1000(1 : 1)	-	0.78	-	73: ORR	ORR: 0.1 M	[10]
2023	FeNiCoMnRu@CNT	1.549	-	-	56: OER	OER: seawater + 1 M KOH	[11]
2022	(PtPdAuAgCuIrRu) clusters@ $(AlNiCoFeCrMoTi)_3O_4$	1.47	0.89	0.58	49.3: OER	ORR: 0.1 M KOH OER: 1 M KOH	[12]
2022	MnNiCuCoVFeMoPdPtAu RuIr/NG	1.493	0.836	0.63	86.7	0.1 M KOH ORR & 1 M KOH OER	[13]

2020	AlFeCoNiCr	1.47	0.71	0.76	52: OER	ORR: 0.1 M KOH OER: 1 M KOH	[14]
2023	$Fe_6Ni_{20}Co_2Mn_2Cu_{1.5}$@rGO	1.52	-	-	48.9: OER	OER: 1 M KOH	[15]
2023	Co-N-C@ CoNiFe-LDH	1.54	0.79	0.75	64: OER	ORR: 0.1 M KOH OER: 0.1 M KOH	[16]
2021	CC3	1.62	0.83	0.79	101: OER	ORR: 0.1 M KOH OER: 0.1 M KOH	[17]
2016	NCNF-1000	1.84	0.82	1.02	274: OER	ORR: 0.1 M KOH OER: 0.1 M KOH	[18]
2015	NCNT/CoO-NiO-NiCo	1.50	0.83	0.67	63: ORR 40: OER	ORR: 0.1 M KOH OER: 1 M KOH	[19]
2022	MoNiFe	1.525	0.896	0.63	46.8: ORR 62.2: OER	ORR: 1 M KOH OER: 1 M KOH	[20]

2015	Directly grown MnO_x	-	-	-	-	-	[21]
2017	$Fe_{0.5}Co_{0.5}O_x$/NrGO						[22]
2014	dp-$MnCo_2O_4$/CNT	-	-	-	106	ORR: 0.1 M KOH OER: 0.1 M KOH	[23]
2015	Co_3O_4 Nps	-	-0.188 (Ag/AgCl)	-	23: OER	0.1 M KOH	[24]
2018	Co–N_x/C NRA	1.53	0.877	0.653	66: ORR 62.3: OER	0.1 M KOH	[25]
2013	CoO/N-CNT and NiFe LDH	-	-	-	-	-	[26]
2020	FeCo/ Co_2P@NPCF	1.56	0.79	0.77	62: ORR 61: OER	ORR: 0.1 M KOH OER: 0.1 M KOH	[27]

2019	FeCo/FeCoNi@NCNTs-HF	1.608	0.850	0.758	71: ORR 66: OER	ORR: 0.1 M KOH OER: 0.1 M KOH	[28]
2021	FeCo-1/NSC	1.555 -	0.82	0.83	69.75: ORR 99.15: OER	ORR: 0.1 M KOH OER: 1 M KOH	[29]
2023	FeCo/Co−N−C	1.61	0.86	0.75	56: ORR 79: OER	ORR: 0.1 M KOH OER: 0.1 M KOH	[30]
2017	N-GCNT/FeCo-3	1.73	0.92	0.81	66.8: ORR 99.5: OER	ORR: 0.1 M KOH OER: 0.1 M KOH	[31]
2021	NPC/FeCo@NCNT	1.57	0.829	0.741	46: ORR 50.6: OER	ORR: 0.1 M KOH OER: 0.1 M KOH	[32]
2020	FeCo/FeN_2/ NHOPC	1.57	0.86	0.71	59: ORR 91: OER	ORR: 1 M KOH OER: 1 M KOH	[33]

2023	Co/FeCo@Fe(Co)$_3$O$_4$	1.65	0.79	0.86	-	0.1 M KOH	[34]
2022	FeCo/LNCNT	1.48	0.86	0.62	-	0.1 M KOH	[35]
2023	FeCo@MNC	1.60	0.90	0.70	51.9: ORR	ORR: 0.1 M KOH OER: 1 M KOH	[36]
2023	FeOOH-CNT-FeCo/NC	1.65	0.79	0.86	44: ORR 127: OER	ORR: 0.1 M KOH OER: 0.1 M KOH	[37]
2019	FeCo@MNC	1.47	0.85	0.62	66: ORR 60: OER	ORR: 0.1 M KOH OER: 1 M KOH	[38]
2022	FeCo@Co/N-C-8	1.542	0.87	0.672	91: ORR 87: OER	ORR: 0.1 M KOH OER: 1 M KOH	[39]
2023	NF/CCO/FCH	1.49	0.83	0.66	94.3: OER	ORR: 1 M KOH OER: 1 M KOH	[40]
2021	CoNC@LDH	1.47	0.84	0.63	55: ORR	0.1 M KOH	[41]

					48: OER		
2018	Ternary $Ni_{46}Co_{40}Fe_{14}$ (C@ NCF-900)	1.66	0.93	0.73	124: ORR 66: OER	ORR: 0.1 M KOH OER: 1 M KOH	[42]
2015	NPMC-1000	-	0.85	-	89: ORR 193: OER	0.1 M KOH	[43]
2017	Ni_3FeN	1.585	0.78	0.81	70: OER	ORR: 0.1 M KOH OER: 0.1 M KOH	[44]
2020	FeCoMoS@NG	1.58	0.83	0.75	65: ORR 51: OER	ORR: 0.1 M KOH OER: 1 M KOH	[45]
2019	Co-Mn-Ni ternary spinel oxides (CMN-231)	1.631	0.749	0.88	75.9: ORR 120: OER	ORR: 0.1 M KOH OER: 0.1 M KOH	[46]
2019	FeCoNi-CNF	1.45	-	-	57: OER	OER: 1 M KOH	[47]

2022	$Fe_4Co_1Ni_2$@hNCTs	1.58	0.83	0.75	90: ORR 120: OER	ORR: 0.1 M KOH OER: 0.1 M KOH	[48]
2017	Ternary spinel oxides, $M_{0.1}Ni_{0.9}Co_2O_4$ (M: Mn, Fe, Cu, Zn) (FNCO-01)	-	-	-	-	ORR: 0.1 M KOH OER: 0.1 M KOH	[49]
2022	Ternary $Pd_{45}Pt_{44}Ni_{11}$ SpNSs/C	1.686	-	-	88: OER	ORR: 0.1 M KOH OER: 0.1 M KOH	[50]
2021	MnCoNi-C-D	1.61	0.82	0.79	68.5: ORR 77.3: OER	ORR: 0.1 M KOH OER: 0.1 M KOH	[51]
2022	Ox-MnCoNi-C (4h)	1.59	0.8	0.79	86: ORR 86: OER	ORR: 0.1 M KOH OER: 0.1 M KOH	[52]
2021	FeCoNi@HNC	1.621	0.805	0.82	51.5: ORR 47: OER	ORR: 0.1 M KOH OER: 0.1 M KOH	[53]

2024	Fe-NP/MNCF	-	0.89	-	46: ORR	ORR: 0.1 M	[54]
2024	Co-NCS-5||Co2P-NCS-60	1.522	0.886	0.636	52: ORR 99: OER	ORR: 0.1 M KOH OER: 1 M KOH	[55]
2024	Fe–N4SP/NPS-HC	-	0.912	-	39.18: ORR	ORR: 0.1 M KOH	[56]
2024	$Fe_{3\%}Co_{3\%}Ni_{9\%}$-NC1000	1.56	0.927	0.633	84.6: ORR	ORR: 0.1 M KOH	[57]
2024	Fe-FeN-C	1.682	0.921	0.761	60.1: ORR	ORR: 0.1 M KOH OER: 0.1 M KOH	[58]
2024	$CoMoO_4$-RuO_2	1.407	0.858	0.549	62.4: OER	ORR: 0.1 M KOH	[59]
2024	CoN/MnO@NC	1.525	0.83	0.69	62: ORR 69: OER	ORR: 0.1 M KOH OER: 1 M KOH	[60]
2024	CoN_3NLF	1.531	0.863	0.668	77.9: ORR 69.8: OER	ORR: 0.1 M KOH OER: 0.1 M KOH	[61]

2024	$MnO\text{-}CeO_2$@Cs + RuO_2	-	0.80	-	37.4: ORR	ORR: 0.1 M KOH	[62]
2023	Co/ Co_7Fe_3@PNCC	1.525	0.899	0.63	65.5: ORR 72.8: OER	ORR: 0.1 M KOH OER: 1 M KOH	[63]
2024	FeCo-MI@TAP-900	1.615	0.86	0.755	115: ORR 83: OER	ORR: 0.1 M KOH OER: 0.1 M KOH	[64]
2024	FeCo/Co_2P/Fe_2P@NPC	1.511	0.79	0.73	117: ORR 85: OER	ORR: 0.1 M KOH OER: 0.1 M KOH	[65]
2024	LSCNiO	1.66	0.6	1.06	91.5: ORR 61.8: OER	ORR: 0.1 M KOH OER: 0.1 M KOH	[66]
2024	N, B, and F-doped PCNF	1.51	0.90	0.61	58: ORR 87: OER	ORR: 0.1 M KOH OER: 1 M KOH	[67]
2024	Co–N–C 800	-	0.85	-	50: ORR	ORR: 0.1 M KOH	[68]

2024	Ni-CAT/NiFe-LDH/CNFs	1.60	0.74	0.86	79: OER	ORR: 0.1 M KOH OER: 1 M KOH	[69]
2023	$Fe_{0.2}Co_{0.8}$/N-C	1.51	0.84	0.67	6.18: ORR 39.1: OER	ORR: 0.1 M KOH OER: 1 M KOH	[70]
2024	S-VN/Co/NS-MC	-	0.86	-	54.64: ORR	ORR: 0.1 M KOH	[71]
2024	$NiMoO_4 \cdot xH_2O$	1.415	0.618	0.79	148.5: ORR 70.7: OER	ORR: 0.1 M KOH OER: 1 M KOH	[72]

References

(1) Mainar, A. R.; Colmenares, L. C.; Grande, H. J.; Blázquez, J. A. Enhancing the Cycle Life of a Zinc–Air Battery by Means of Electrolyte Additives and Zinc Surface Protection. *Batteries*. MDPI September 1, 2018. https://doi.org/10.3390/batteries4030046.

(2) Iqbal, A.; El-Kadri, O. M.; Hamdan, N. M. Insights into Rechargeable Zn-Air Batteries for Future Advancements in Energy Storing Technology. *Journal of Energy Storage*. Elsevier Ltd June 1, 2023. https://doi.org/10.1016/j.est.2023.106926.

(3) Jin, Z.; Lyu, J.; Zhao, Y. L.; Li, H.; Lin, X.; Xie, G.; Liu, X.; Kai, J. J.; Qiu, H. J. Rugged High-Entropy Alloy Nanowires with in Situ Formed Surface Spinel Oxide As Highly Stable Electrocatalyst in Zn-Air Batteries. *ACS Mater Lett* **2020**, *2* (12), 1698–1706. https://doi.org/10.1021/acsmaterialslett.0c00434.

(4) Jin, Z.; Lyu, J.; Hu, K.; Chen, Z.; Xie, G.; Liu, X.; Lin, X.; Qiu, H. J. Eight-Component Nanoporous High-Entropy Oxides with Low Ru Contents as High-Performance Bifunctional Catalysts in Zn-Air Batteries. *Small* **2022**, *18* (12). https://doi.org/10.1002/smll.202107207.

(5) Jin, Z.; Lyu, J.; Zhao, Y. L.; Li, H.; Chen, Z.; Lin, X.; Xie, G.; Liu, X.; Kai, J. J.; Qiu, H. J. Top-Down Synthesis of Noble Metal Particles on High-Entropy Oxide Supports for Electrocatalysis. *Chemistry of Materials* **2021**, *33* (5), 1771–1780. https://doi.org/10.1021/acs.chemmater.0c04695.

(6) Yu, T.; Xu, H.; Jin, Z.; Zhang, Y.; Qiu, H. J. Noble Metal-Free High-Entropy Oxide/Co-N-C Bifunctional Electrocatalyst Enables Highly Reversible and Durable Zn-Air Batteries. *Appl Surf Sci* **2023**, *610*. https://doi.org/10.1016/j.apsusc.2022.155624.

(7) He, R.; Yang, L.; Zhang, Y.; Wang, X.; Lee, S.; Zhang, T.; Li, L.; Liang, Z.; Chen, J.; Li, J.; Ostovari Moghaddam, A.; Llorca, J.; Ibáñez, M.; Arbiol, J.; Xu, Y.; Cabot, A. A CrMnFeCoNi High Entropy Alloy Boosting Oxygen Evolution/Reduction Reactions and Zinc-Air Battery

Performance. *Energy Storage Mater* **2023**, *58*, 287–298. https://doi.org/10.1016/j.ensm.2023.03.022.

(8) Cao, X.; Gao, Y.; Wang, Z.; Zeng, H.; Song, Y.; Tang, S.; Luo, L.; Gong, S. FeNiCrCoMn High-Entropy Alloy Nanoparticles Loaded on Carbon Nanotubes as Bifunctional Oxygen Catalysts for Rechargeable Zinc-Air Batteries. *ACS Appl Mater Interfaces* **2023**. https://doi.org/10.1021/acsami.3c04120.

(9) Yu, T.; Zhang, Y.; Hu, Y.; Hu, K.; Lin, X.; Xie, G.; Liu, X.; Reddy, K. M.; Ito, Y.; Qiu, H. J. Twelve-Component Free-Standing Nanoporous High-Entropy Alloys for Multifunctional Electrocatalysis. *ACS Mater Lett* **2022**, *4* (1), 181–189. https://doi.org/10.1021/acsmaterialslett.1c00762.

(10) Yao, Y.; Li, Z.; Dou, Y.; Jiang, T.; Zou, J.; Lim, S. Y.; Norby, P.; Stamate, E.; Jensen, J. O.; Zhang, W. High Entropy Alloy Nanoparticles Encapsulated in Graphitised Hollow Carbon Tubes for Oxygen Reduction Electrocatalysis. *Dalton Transactions* **2023**, *52* (13), 4142–4151. https://doi.org/10.1039/d2dt03637a.

(11) Zhang, Q.; Lian, K.; Liu, Q.; Qi, G.; Zhang, S.; Luo, J.; Liu, X. High Entropy Alloy Nanoparticles as Efficient Catalysts for Alkaline Overall Seawater Splitting and Zn-Air Batteries. *J Colloid Interface Sci* **2023**, *646*, 844–854. https://doi.org/10.1016/j.jcis.2023.05.074.

(12) Jin, Z.; Zhou, X.; Hu, Y.; Tang, X.; Hu, K.; Reddy, K. M.; Lin, X.; Qiu, H. J. A Fourteen-Component High-Entropy Alloy@oxide Bifunctional Electrocatalyst with a Record-Low ΔE of 0.61 V for Highly Reversible Zn-Air Batteries. *Chem Sci* **2022**, *13* (41), 12056–12064. https://doi.org/10.1039/d2sc04461g.

(13) Lin, X.; Hu, Y.; Hu, K.; Lin, X.; Xie, G.; Liu, X.; Reddy, K. M.; Qiu, H. J. Inhibited Surface Diffusion of High-Entropy Nano-Alloys for the Preparation of 3D Nanoporous Graphene with

High Amounts of Single Atom Dopants. *ACS Mater Lett* **2022**, *4* (5), 978–986. https://doi.org/10.1021/acsmaterialslett.2c00245.

(14) Fang, G.; Gao, J.; Lv, J.; Jia, H.; Li, H.; Liu, W.; Xie, G.; Chen, Z.; Huang, Y.; Yuan, Q.; Liu, X.; Lin, X.; Sun, S.; Qiu, H. J. Multi-Component Nanoporous Alloy/(Oxy)Hydroxide for Bifunctional Oxygen Electrocatalysis and Rechargeable Zn-Air Batteries. *Appl Catal B* **2020**, *268*. https://doi.org/10.1016/j.apcatb.2019.118431.

(15) Gao, L.; Zhong, X.; Li, Z.; Hu, J.; Cui, S.; Wang, X.; Xu, B. Multi-Layer Reduced Graphene Oxide Encapsulates High-Entropy Alloy for Rechargeable Zinc-Air Batteries. *Chemical Communications* **2024**. https://doi.org/10.1039/d3cc05069f.

(16) Arafat, Y.; Zhong, Y.; Azhar, M. R.; Asif, M.; Tadé, M. O.; Shao, Z. CoNiFe-Layered Double Hydroxide Decorated Co-N-C Network as a Robust Bi-Functional Oxygen Electrocatalyst for Zinc-Air Batteries. *EcoMat* **2023**. https://doi.org/10.1002/eom2.12394.

(17) Henkelman, G.; Wei, L.; Chen, Y.; Liu, C.; Liu, F.; Li, H.; Chen, J.; Fei, J.; Yu, Z.; Yuan, Z.; Wang, C.; Zheng, H.; Liu, Z.; Xu, M. One-Dimensional van Der Waals Heterostructures as Efficient Metal-Free Oxygen Electrocatalysts. *ACS Nano* **2021**, *15* (2), 3309–3319. https://doi.org/10.1021/acsnano.0c10242.

(18) Liu, Q.; Wang, Y.; Dai, L.; Yao, J. Scalable Fabrication of Nanoporous Carbon Fiber Films as Bifunctional Catalytic Electrodes for Flexible Zn-Air Batteries. *Advanced Materials* **2016**, *28* (15), 3000–3006. https://doi.org/10.1002/adma.201506112.

(19) Liu, X.; Park, M.; Kim, M. G.; Gupta, S.; Wu, G.; Cho, J. Integrating NiCo Alloys with Their Oxides as Efficient Bifunctional Cathode Catalysts for Rechargeable Zinc–Air Batteries. *Angewandte Chemie* **2015**, *127* (33), 9790–9794. https://doi.org/10.1002/ange.201503612.

(20) Dang, L.; Zhang, K.; Wang, Q.; Xu, C.; Wang, S. Fe-Alloyed MoNi Nanohybrids as Oxygen Evolution Reaction/Oxygen Reduction Reaction Bifunctional Electrocatalyst for Rechargeable

Zinc–Air Batteries. *Physica Status Solidi (A) Applications and Materials Science* **2023**, *220* (2). https://doi.org/10.1002/pssa.202200581.

(21) Sumboja, A.; Ge, X.; Goh, F. W. T.; Li, B.; Geng, D.; Hor, T. S. A.; Zong, Y.; Liu, Z. Manganese Oxide Catalyst Grown on Carbon Paper as an Air Cathode for High-Performance Rechargeable Zinc-Air Batteries. *Chempluschem* **2015**, *80* (8), 1341–1346. https://doi.org/10.1002/cplu.201500183.

(22) Wei, L.; Karahan, H. E.; Zhai, S.; Liu, H.; Chen, X.; Zhou, Z.; Lei, Y.; Liu, Z.; Chen, Y. Amorphous Bimetallic Oxide–Graphene Hybrids as Bifunctional Oxygen Electrocatalysts for Rechargeable Zn–Air Batteries. *Advanced Materials* **2017**, *29* (38). https://doi.org/10.1002/adma.201701410.

(23) Ge, X.; Liu, Y.; Goh, F. W. T.; Hor, T. S. A.; Zong, Y.; Xiao, P.; Zhang, Z.; Lim, S. H.; Li, B.; Wang, X.; Liu, Z. Dual-Phase Spinel MnCo2O4 and Spinel MnCo 2O4/Nanocarbon Hybrids for Electrocatalytic Oxygen Reduction and Evolution. *ACS Appl Mater Interfaces* **2014**, *6* (15), 12684–12691. https://doi.org/10.1021/am502675c.

(24) Li, B.; Ge, X.; Goh, F. W. T.; Hor, T. S. A.; Geng, D.; Du, G.; Liu, Z.; Zhang, J.; Liu, X.; Zong, Y. Co3O4 Nanoparticles Decorated Carbon Nanofiber Mat as Binder-Free Air-Cathode for High Performance Rechargeable Zinc-Air Batteries. *Nanoscale* **2015**, *7* (5), 1830–1838. https://doi.org/10.1039/c4nr05988c.

(25) Amiinu, I. S.; Liu, X.; Pu, Z.; Li, W.; Li, Q.; Zhang, J.; Tang, H.; Zhang, H.; Mu, S. From 3D ZIF Nanocrystals to Co–Nx/C Nanorod Array Electrocatalysts for ORR, OER, and Zn–Air Batteries. *Adv Funct Mater* **2018**, *28* (5). https://doi.org/10.1002/adfm.201704638.

(26) Li, Y.; Gong, M.; Liang, Y.; Feng, J.; Kim, J. E.; Wang, H.; Hong, G.; Zhang, B.; Dai, H. Advanced Zinc-Air Batteries Based on High-Performance Hybrid Electrocatalysts. *Nat Commun* **2013**, *4*. https://doi.org/10.1038/ncomms2812.

(27) Shi, Q.; Liu, Q.; Ma, Y.; Fang, Z.; Liang, Z.; Shao, G.; Tang, B.; Yang, W.; Qin, L.; Fang, X. High-Performance Trifunctional Electrocatalysts Based on FeCo/Co2P Hybrid Nanoparticles for Zinc–Air Battery and Self-Powered Overall Water Splitting. *Adv Energy Mater* **2020**, *10* (10). https://doi.org/10.1002/aenm.201903854.

(28) Wang, Z.; Ang, J.; Zhang, B.; Zhang, Y.; Ma, X. Y. D.; Yan, T.; Liu, J.; Che, B.; Huang, Y.; Lu, X. FeCo/FeCoNi/N-Doped Carbon Nanotubes Grafted Polyhedron-Derived Hybrid Fibers as Bifunctional Oxygen Electrocatalysts for Durable Rechargeable Zinc–Air Battery. *Appl Catal B* **2019**, *254*, 26–36. https://doi.org/10.1016/j.apcatb.2019.04.027.

(29) Chang, S.; Zhang, H.; Zhang, Z. FeCo Alloy/N, S Dual-Doped Carbon Composite as a High-Performance Bifunctional Catalyst in an Advanced Rechargeable Zinc-Air Battery. *Journal of Energy Chemistry* **2021**, *56*, 64–71. https://doi.org/10.1016/j.jechem.2020.07.047.

(30) Zhong, J.; Zhu, Z.; Xu, Q.; Peng, L.; Luo, K.; Yuan, D. FeCo Alloy Nanoparticles Supported on Co-N-C Cubes Derived from Imidazolate Frameworks as a Bifunctional Electrocatalyst for Rechargeable Zinc-Air Batteries. *Energy and Fuels* **2023**. https://doi.org/10.1021/acs.energyfuels.3c02221.

(31) Su, C. Y.; Cheng, H.; Li, W.; Liu, Z. Q.; Li, N.; Hou, Z.; Bai, F. Q.; Zhang, H. X.; Ma, T. Y. Atomic Modulation of FeCo–Nitrogen–Carbon Bifunctional Oxygen Electrodes for Rechargeable and Flexible All-Solid-State Zinc–Air Battery. *Adv Energy Mater* **2017**, *7* (13). https://doi.org/10.1002/aenm.201602420.

(32) Hao, X.; Jiang, Z.; Zhang, B.; Tian, X.; Song, C.; Wang, L.; Maiyalagan, T.; Hao, X.; Jiang, Z. J. N-Doped Carbon Nanotubes Derived from Graphene Oxide with Embedment of FeCo Nanoparticles as Bifunctional Air Electrode for Rechargeable Liquid and Flexible All-Solid-State Zinc–Air Batteries. *Advanced Science* **2021**, *8* (10). https://doi.org/10.1002/advs.202004572.

(33) Wang, Y.; Qiao, M.; Mamat, X. An Advantage Combined Strategy for Preparing Bi-Functional Electrocatalyst in Rechargeable Zinc-Air Batteries. *Chemical Engineering Journal* **2020**, *402*. https://doi.org/10.1016/j.cej.2020.126214.

(34) Xiong, Y.; Jiang, Z.; Gong, L.; Tian, X.; Song, C.; Maiyalagan, T.; Jiang, Z. J. Construction of Co/FeCo@Fe(Co)3O4 Heterojunction Rich in Oxygen Vacancies Derived from Metal–Organic Frameworks Using O2 Plasma as a High-Performance Bifunctional Catalyst for Rechargeable Zinc-Air Batteries. *J Colloid Interface Sci* **2023**, *649*, 36–48. https://doi.org/10.1016/j.jcis.2023.06.040.

(35) Wen, J.; Li, X.; Liu, Y.; Yang, M.; Liu, B.; Chen, H.; Li, H. Facile Crafting of Ultralong N-Doped Carbon Nanotube Encapsulated with FeCo Nanoparticles as Bifunctional Electrocatalyst for Rechargeable Zinc-Air Batteries. *Microporous and Mesoporous Materials* **2022**, *336*. https://doi.org/10.1016/j.micromeso.2022.111850.

(36) Fan, M.; Liu, P.; Cheng, Y.; Tang, H.; Jin, B.; Zhang, H. Fe-N4/Co-N4 Active Sites Engineered Porous Carbon with Encapsulated FeCo Alloy as an Efficient Bifunctional Catalyst for Rechargeable Zinc-Air Battery. *J Alloys Compd* **2023**, *935*. https://doi.org/10.1016/j.jallcom.2022.168107.

(37) Yang, P. Q.; Ko, T. E.; Tseng, C. M.; Wang, W. H.; Huang, C. C.; Tsai, J. E.; Fu, Y. C.; Li, Y. Y. FeOOH-Carbon Nanotube-FeCo/Nitrogen-Doped Porous Carbon as an Excellent Bifunctional Catalyst for Achieving High Power Performance in Rechargeable Zinc-Air Batteries. *Journal of Industrial and Engineering Chemistry* **2023**, *121*, 338–347. https://doi.org/10.1016/j.jiec.2023.01.037.

(38) Li, C.; Wu, M.; Liu, R. High-Performance Bifunctional Oxygen Electrocatalysts for Zinc-Air Batteries over Mesoporous Fe/Co-N-C Nanofibers with Embedding FeCo Alloy Nanoparticles. *Appl Catal B* **2019**, *244*, 150–158. https://doi.org/10.1016/j.apcatb.2018.11.039.

(39) Song, L.; Zhang, J.; Sarkar, S.; Zhao, C.; Wang, Z.; Huang, C.; Yan, L.; Zhao, Y. Interface Engineering of FeCo-Co Structure as Bifunctional Oxygen Electrocatalyst for Rechargeable Zinc-Air Batteries via Alloying Degree Control Strategy. *Chemical Engineering Journal* **2022**, *433*. https://doi.org/10.1016/j.cej.2021.133686.

(40) Yang, X.; Zhou, Z.; Zou, Y.; Kuang, J.; Ye, D.; Zhang, S.; Gao, Q.; Yang, S.; Cai, X.; Fang, Y. Interface Reinforced 2D/2D Heterostructure of Cu-Co Oxides/FeCo Hydroxides as Monolithic Multifunctional Catalysts for Rechargeable/Flexible Zinc-Air Batteries and Self-Powered Water Splitting. *Appl Catal B* **2023**, *325*. https://doi.org/10.1016/j.apcatb.2022.122332.

(41) Zhao, C. X.; Liu, J. N.; Wang, J.; Ren, D.; Yu, J.; Chen, X.; Li, B. Q.; Zhang, Q. A ΔE = 0.63 V Bifunctional Oxygen Electrocatalyst Enables High-Rate and Long-Cycling Zinc–Air Batteries. *Advanced Materials* **2021**, *33* (15). https://doi.org/10.1002/adma.202008606.

(42) Nam, G.; Son, Y.; Park, S. O.; Jeon, W. C.; Jang, H.; Park, J.; Chae, S.; Yoo, Y.; Ryu, J.; Kim, M. G.; Kwak, S. K.; Cho, J. A Ternary Ni46Co40Fe14 Nanoalloy-Based Oxygen Electrocatalyst for Highly Efficient Rechargeable Zinc–Air Batteries. *Advanced Materials* **2018**, *30* (46). https://doi.org/10.1002/adma.201803372.

(43) Zhang, J.; Zhao, Z.; Xia, Z.; Dai, L. A Metal-Free Bifunctional Electrocatalyst for Oxygen Reduction and Oxygen Evolution Reactions. *Nat Nanotechnol* **2015**, *10* (5), 444–452. https://doi.org/10.1038/nnano.2015.48.

(44) Fu, G.; Cui, Z.; Chen, Y.; Xu, L.; Tang, Y.; Goodenough, J. B. Hierarchically Mesoporous Nickel-Iron Nitride as a Cost-Efficient and Highly Durable Electrocatalyst for Zn-Air Battery. *Nano Energy* **2017**, *39*, 77–85. https://doi.org/10.1016/j.nanoen.2017.06.029.

(45) Ramakrishnan, S.; Balamurugan, J.; Vinothkannan, M.; Kim, A. R.; Sengodan, S.; Yoo, D. J. Nitrogen-Doped Graphene Encapsulated FeCoMoS Nanoparticles as Advanced Trifunctional

Catalyst for Water Splitting Devices and Zinc–Air Batteries. *Appl Catal B* **2020**, *279*. https://doi.org/10.1016/j.apcatb.2020.119381.

(46) Wang, Q.; Xue, Y.; Sun, S.; Yan, S.; Miao, H.; Liu, Z. Facile Synthesis of Ternary Spinel Co–Mn–Ni Nanorods as Efficient Bi-Functional Oxygen Catalysts for Rechargeable Zinc-Air Batteries. *J Power Sources* **2019**, *435*. https://doi.org/10.1016/j.jpowsour.2019.226761.

(47) Li, C.; Zhang, Z.; Wu, M.; Liu, R. FeCoNi Ternary Alloy Embedded Mesoporous Carbon Nanofiber: An Efficient Oxygen Evolution Catalyst for Rechargeable Zinc-Air Battery. *Mater Lett* **2019**, *238*, 138–142. https://doi.org/10.1016/j.matlet.2018.11.160.

(48) Tang, W.; He, J.; Teng, K.; Gao, L.; Qi, R.; Deng, Y.; Liu, R.; Li, A.; Fu, H.; Wang, C. A. Toward Highly Efficient Bifunctional Electrocatalysts for Zinc-Air Batteries: From Theoretical Prediction to a Ternary FeCoNi Design. *Nanoscale* **2022**, *14* (46), 17447–17459. https://doi.org/10.1039/d2nr04741a.

(49) Lu, Y. T.; Chien, Y. J.; Liu, C. F.; You, T. H.; Hu, C. C. Active Site-Engineered Bifunctional Electrocatalysts of Ternary Spinel Oxides, M0.1Ni0.9Co2O4 (M: Mn, Fe, Cu, Zn) for the Air Electrode of Rechargeable Zinc-Air Batteries. *J Mater Chem A Mater* **2017**, *5* (39), 21016–21026. https://doi.org/10.1039/c7ta06302d.

(50) Liu, K.; Huang, H.; Zhu, Y.; Wang, S.; Lyu, Z.; Han, X.; Kuang, Q.; Xie, S. Edge-Segregated Ternary Pd-Pt-Ni Spiral Nanosheets as High-Performance Bifunctional Oxygen Redox Electrocatalysts for Rechargeable Zinc-Air Batteries. *J Mater Chem A Mater* **2022**, *10* (7), 3808–3817. https://doi.org/10.1039/d1ta10585j.

(51) Wang, X.; Zhang, J.; Ma, D.; Feng, X.; Wang, L.; Wang, B. Metal-Organic Framework-Derived Trimetallic Nanocomposites as Efficient Bifunctional Oxygen Catalysts for Zinc-Air Batteries. *ACS Appl Mater Interfaces* **2021**, *13* (28), 33209–33217. https://doi.org/10.1021/acsami.1c02570.

(52) Rui, C.; Zhang, T.; Jiang, Y.; Xie, D.; Li, M.; Lu, Q.; Bu, Y. Highly Efficient and Stable Bifunctional Electrocatalyst with Alloy/Oxide Heterostructures for a Rechargeable Zinc-Air Battery. *Energy and Fuels* **2022**, *36* (20), 12816–12825. https://doi.org/10.1021/acs.energyfuels.2c02744.

(53) Liu, J.; Luo, Z.; Zhang, X.; Zheng, H.; Peng, L.; Qian, D.; Jia, C.; Sun-Waterhouse, D.; Waterhouse, G. I. N. FeCoNi Nanoalloys Embedded in Hierarchical N-Rich Carbon Matrix with Enhanced Oxygen Electrocatalysis for Rechargeable Zn-Air Batteries. *J Mater Chem A Mater* **2021**, *9* (48), 27701–27708. https://doi.org/10.1039/d1ta09964g.

(54) Wang, T.; Zhang, Q.; Lian, K.; Qi, G.; Liu, Q.; Feng, L.; Hu, G.; Luo, J.; Liu, X. Fe Nanoparticles Confined by Multiple-Heteroatom-Doped Carbon Frameworks for Aqueous Zn-Air Battery Driving CO2 Electrolysis. *J Colloid Interface Sci* **2024**, *655*, 176–186. https://doi.org/10.1016/j.jcis.2023.10.157.

(55) Wei, J.; Lou, J.; Hu, W.; Song, X.; Wang, H.; Yang, Y.; Zhang, Y.; Jiang, Z.; Mei, B.; Wang, L.; Yang, T.; Wang, Q.; Li, X. Superstructured Carbon with Enhanced Kinetics for Zinc-Air Battery and Self-Powered Overall Water Splitting. *Small* **2024**. https://doi.org/10.1002/smll.202308956.

(56) Liu, J.; Chen, W.; Yuan, S.; Liu, T.; Wang, Q. High-Coordination Fe-N4SP Single-Atom Catalysts via the Multi-Shell Synergistic Effect for the Enhanced Oxygen Reduction Reaction of Rechargeable Zn-Air Battery Cathodes. *Energy Environ Sci* **2023**. https://doi.org/10.1039/d3ee03183g.

(57) Zhai, W.; He, Y.; Duan, Y. e.; Guo, S.; Chen, Y.; Dai, Z.; Liu, L.; Tan, Q. Densely Populated Trimetallic Single-Atoms for Durable Low-Temperature Flexible Zinc-Air Batteries. *Appl Catal B* **2024**, *342*. https://doi.org/10.1016/j.apcatb.2023.123438.

(58) Lu, X.; Li, Y.; Dong, D.; Wan, Y.; Li, R.; Xiao, L.; Wang, D.; Liu, L.; Wang, G.; Zhang, J.; An, M.; Yang, P. Coexisting Fe Single Atoms and Nanoparticles on Hierarchically Porous Carbon for High-Efficiency Oxygen Reduction Reaction and Zn-Air Batteries. *J Colloid Interface Sci* **2024**, *653*, 654–663. https://doi.org/10.1016/j.jcis.2023.09.047.

(59) Chen, S.; Xu, J.; Chen, J.; Yao, Y.; Wang, Z.; Li, P.; Li, Y.; Wang, F. Ru Doping Induced Interface Engineering in Flower-Liked CoMoO4-RuO2 Boosts Oxygen Electrocatalysis for Rechargeable Zn-Air Battery. *J Colloid Interface Sci* **2024**, *658*, 230–237. https://doi.org/10.1016/j.jcis.2023.12.066.

(60) Niu, Y.; Jiang, G.; Gong, S.; Liu, X.; Shangguan, E.; Li, L.; Chen, Z. Engineering of Heterointerface of Ultrathin Carbon Nanosheet-Supported CoN/MnO Enhances Oxygen Electrocatalysis for Rechargeable Zn–Air Batteries. *J Colloid Interface Sci* **2024**, *656*, 346–357. https://doi.org/10.1016/j.jcis.2023.11.112.

(61) Liu, X.; Wang, Z.; Wang, J.; Tang, T.; Li, C.; Yu, J.; Zhang, S.; Deng, C. Unsaturated Cobalt-Nitrogen Atomic Sites in Necklace-like Hairy Fibers towards Highly Efficient Oxygen Electrocatalysis for Flexible Zn-Air Battery. *Energy Storage Mater* **2024**, 103184. https://doi.org/10.1016/j.ensm.2024.103184.

(62) Wang, L.; Hu, X.; Li, H.; Huang, Z.; Huang, J.; Isimjan, T. T.; Yang, X. Engineering Built-in Electric Fields in Oxygen-Deficient MnO-CeO $_2$ @Cs Catalysts: Enhanced Performance and Kinetics for the Oxygen Reduction Reaction in Aqueous/Flexible Zinc–Air Batteries. *Green Chemistry* **2024**. https://doi.org/10.1039/D3GC04537D.

(63) Lian, Y.; Yu, T.; Qu, Y.; Yuan, C.; Lu, Z.-H.; Guo, M. Interface Electronic Modulation of Monodispersed Co Metal-Co $_7$ Fe $_3$ Alloy Heterostructures for Rechargeable Zn–Air Battery. *Ind Eng Chem Res* **2024**. https://doi.org/10.1021/acs.iecr.3c03149.

(64) Zheng, J.; Hu, G.; Liu, B.; Liu, Y.; Li, H.; Zhao, H.; Yang, M. In-Situ Spatial-Embedding Construction of FeCo Nucleus-Bound Carbon Skeletons for Durable Rechargeable Liquid and Flexible Zn-Air Batteries. *Energy Storage Mater* **2024**, *65*. https://doi.org/10.1016/j.ensm.2023.103106.

(65) Wang, B.; Liu, Q.; Yuan, A.; Shi, Q.; Jiang, L.; Yang, W.; Yang, T.; Hou, X. A Facile and Green Strategy for Mass Production of Dispersive FeCo-Rich Phosphides@N,P-Doped Carbon Electrocatalysts toward Efficient and Stable Rechargeable Zn-Air Battery and Water Splitting. *J Mater Sci Technol* **2024**, *182*, 1–11. https://doi.org/10.1016/j.jmst.2023.08.073.

(66) Anand, P.; Wong, M. S.; Fu, Y. P. Lanthanum Strontium Cobaltite-Based Perovskite as an Electrocatalyst for Zinc-Air Battery Application. *J Energy Storage* **2024**, *77*. https://doi.org/10.1016/j.est.2023.109917.

(67) Muthurasu, A.; Pathak, I.; Acharya, D.; Rosyara, Y. R.; Kim, H. Y. Cutting-Edge Nitrogen, Boron, and Fluorine Triply Doped Chain-like Porous Carbon Nanofibers: A Versatile Solution for High-Performance Zinc-Air Batteries and Self-Powered Water Splitting. *J Mater Chem A Mater* **2023**. https://doi.org/10.1039/d3ta06387a.

(68) Zhang, W.; Pu, W.; Zhang, X.; Xiao, Y.; Liu, Y. Preparation of Co N Co-Doped Carbon Nanosheets Electrocatalyst for Efficient Oxygen Reduction Reaction in Zinc-Air Battery. *Diam Relat Mater* **2024**, *142*, 110810. https://doi.org/10.1016/j.diamond.2024.110810.

(69) Li, J.; Qin, Y.; Bai, Z.; Li, S.; Li, L.; Ouyang, B.; Kan, E.; Zhang, W. Investigating the Role of 3D Hierarchical Ni-CAT/NiFe-LDH/CNFs in Enhancing the Oxygen Evolution Reaction and Zn-Air Battery Performance. *Appl Surf Sci* **2024**, *648*. https://doi.org/10.1016/j.apsusc.2023.159080.

(70) Huang, H.; Liang, Q.; Guo, H.; Wang, Z.; Yan, G.; Wu, F.; Wang, J. Spray Pyrolysis Regulated FeCo Alloy Anchoring on Nitrogen–Doped Carbon Hollow Spheres Boost the Performance of Zinc–Air Batteries. *Small* **2024**. https://doi.org/10.1002/smll.202310318.

(71) Deng, D.; Zhang, H.; Wu, J.; Tang, X.; Ling, M.; Dong, S.; Xu, L.; Li, H.; Li, H. Electronic Structure and Spin State Regulation of Vanadium Nitride via a Sulfur Doping Strategy toward Flexible Zinc-Air Batteries. *Journal of Energy Chemistry* **2024**, *89*, 239–249. https://doi.org/10.1016/j.jechem.2023.10.024.

(72) Ayyaluri, R. R.; Krishna, B. N. V.; Ankinapalli, O. R.; Yu, J. S. Facile Hydrothermal Synthesis of NiMoO4·xH2O Nanorods-like Structures as Bifunctional Oxygen Electrocatalysts for Rechargeable Zinc-Air Batteries. *J Energy Storage* **2024**, *78*, 110171. https://doi.org/10.1016/j.est.2023.110171.

Appendix B

Supporting information for Chapter 5.

Hybrid FeCo-Fe_2CoO_4/C bifunctional electrocatalysts for high-performance rechargeable zinc-air batteries.

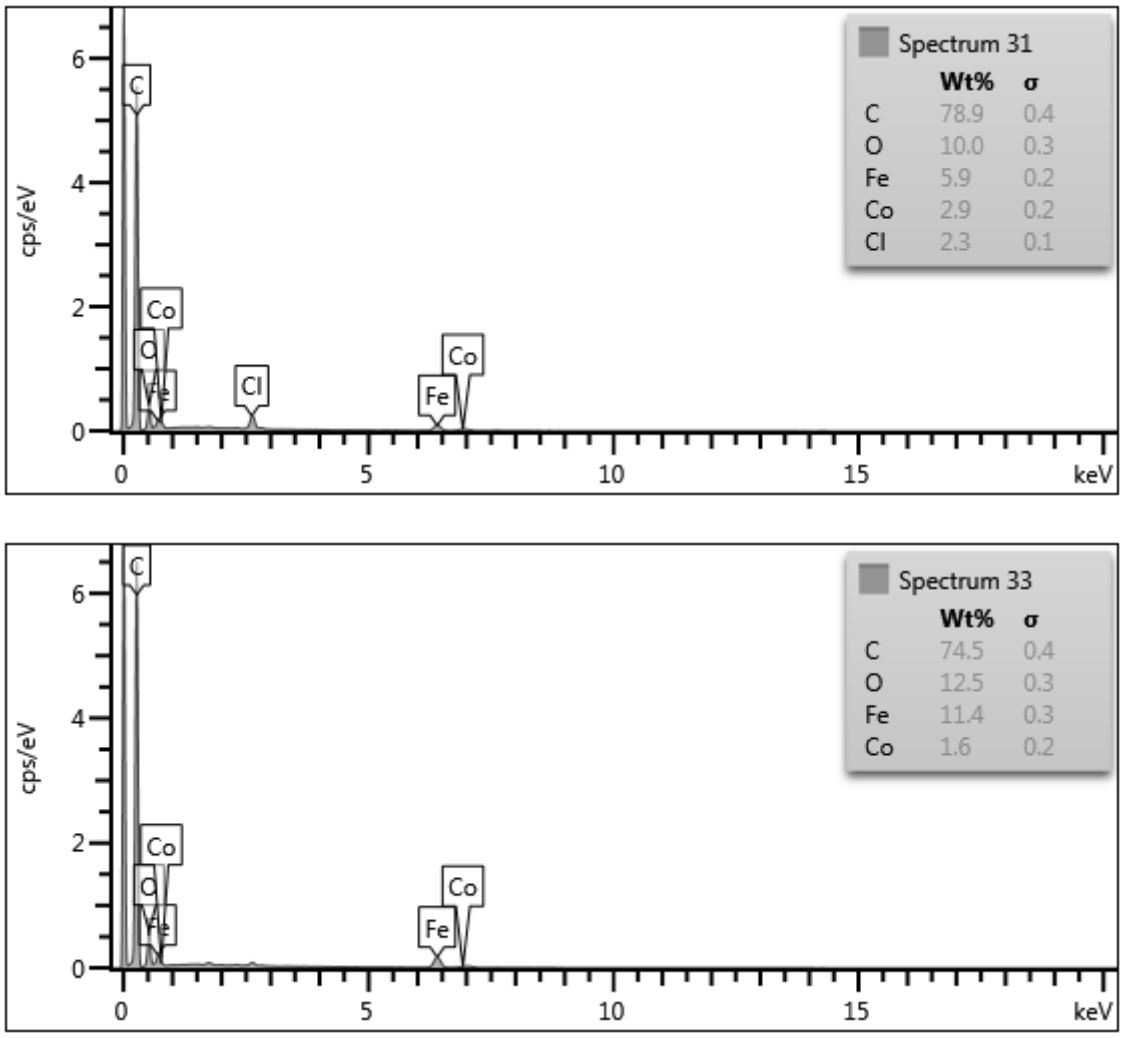

Figure SB 1: The EDS spectra for (a) FeCo-Fe_2CoO_4/C_{Ann} and (b) FeCo-Fe_2CoO_4/C_{MW}.

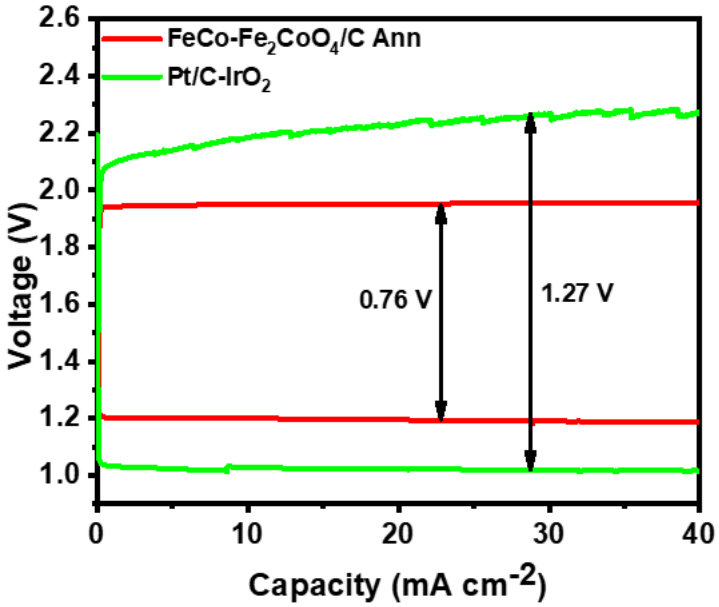

Figure SB 2: Areal capacity curves for FeCo-Fe_2CoO_4/C_{Ann} and Pt/C-IrO_2.

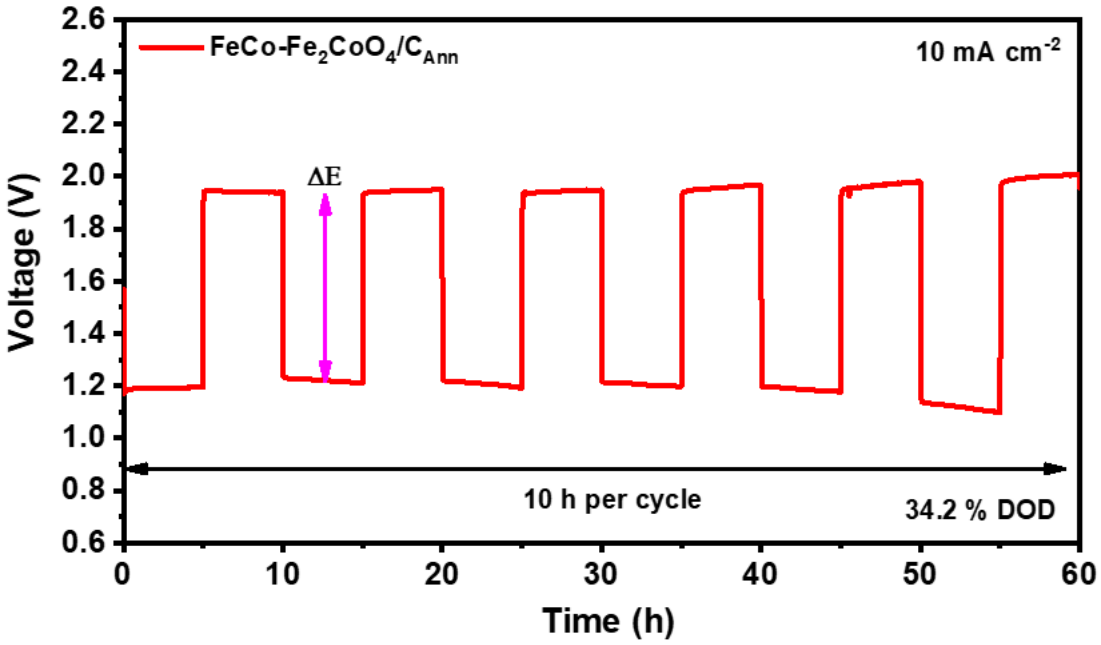

Figure SB 3: Discharge-charge curves for FeCo-Fe_2CoO_4/C_{Ann} at 10 mA cm^{-2} with 5 h discharge and 5 h charge (Areal energy = 60.5 mWh cm^{-2}).

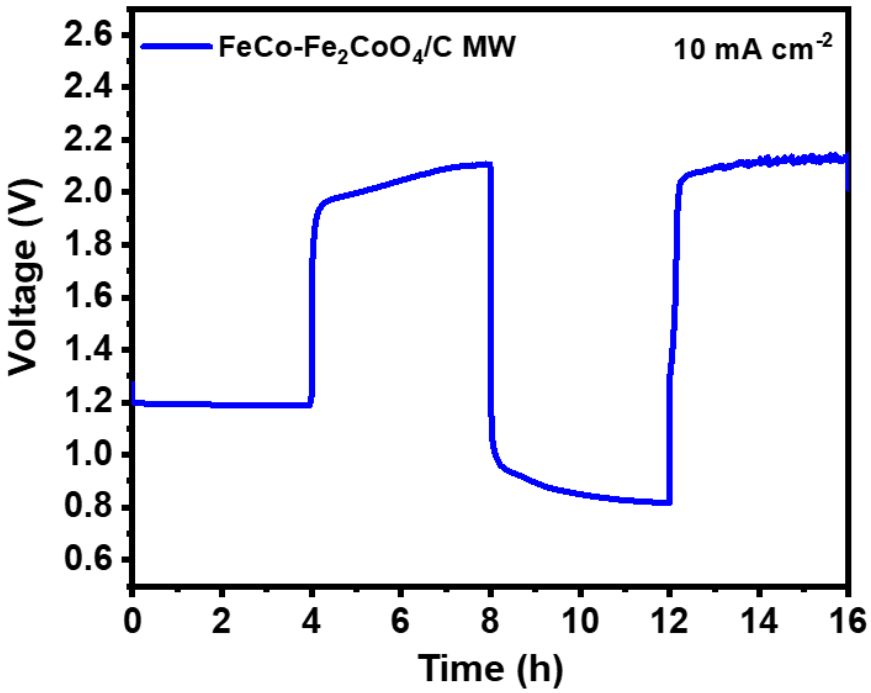

Figure SB 4: Discharge-charge curves for FeCo-Fe_2CoO_4/C MW at 10 $mAcm^{-2}$ with 4 h charge and 4 h discharge.